

450
404
Contract No. N62289-76-C-0086

12
2
**"MULTI JET INDUCED FORCES AND MOMENTS
ON VTOL AIRCRAFT HOVERING IN AND OUT
OF GROUND EFFECT"**

McDonnell Aircraft Company
McDonnell Douglas Corporation
St. Louis, Missouri

June 1977

Final Report for Period 19 April 1976 - 19 April 1977

Distribution: Unlimited

DISTRIBUTION STATEMENT A

Approved for public release;
Distribution Unlimited

Prepared for
NAVAL AIR DEVELOPMENT CENTER
WARMINSTER, PENNSYLVANIA 18974

UNU
ILL
UNI

DDC
JUL 28 1977
D

REPORT DOCUMENTATION PAGE		READ INSTRUCTIONS BEFORE COMPLETING FORM
1. REPORT NUMBER (10) NADCI-77-3229-38	2. GOVT ACCESSION NO.	3. RECIPIENT'S CATALOG NUMBER (9)
4. TITLE (and Subtitle) Multi Jet Induced Forces and Moments on VTOL Aircraft Hovering In and Out of Ground Effect		5. TYPE OF REPORT & PERIOD COVERED Final Technical Report, for period 4/19/76-4/19/77
7. AUTHOR(s) (10) Donald R./Kotansky Norbert A./Durando Dean R./Bristow		6. PERFORMING ORG. REPORT NUMBER N/A 8. CONTRACT OR GRANT NUMBER(s) (15) N62269-76-C-C086
9. PERFORMING ORGANIZATION NAME AND ADDRESS McDonnell Aircraft Company P.O. Box 516 St. Louis, Missouri 63166		10. PROGRAM ELEMENT, PROJECT, TASK AREA & WORK UNIT NUMBERS
11. CONTROLLING OFFICE NAME AND ADDRESS Naval Air Development Center Warminster, Pennsylvania 18974		12. REPORT DATE (11) 19 June 1977
14. MONITORING AGENCY NAME & ADDRESS (if different from Controlling Office) (12) 1078		13. NUMBER OF PAGES
		18. SECURITY CLASS. (of this report) Unclassified
		19a. DECLASSIFICATION DOWNGRADING SCHEDULE
16. DISTRIBUTION STATEMENT (of this Report) Unlimited <div style="border: 1px solid black; padding: 5px; display: inline-block;"> DISTRIBUTION STATEMENT A Approved for public release; Distribution Unlimited </div>		
17. DISTRIBUTION STATEMENT (of the abstract entered in Block 20, if different from Report) Unlimited		
18. SUPPLEMENTARY NOTES		
19. KEY WORDS (Continue on reverse side if necessary and identify by block number) V/STOL Ground Effects Suckdown Fountain Forces		
20. ABSTRACT (Continue on reverse side if necessary and identify by block number) An engineering methodology has been developed for the prediction of propulsive lift system induced aerodynamic effects for multi-lift-jet VTOL aircraft operating in the hover mode in and out of ground effect. The developed methodology takes into account the effects of aircraft geometry, aircraft orientation (pitch, roll) and height above the ground plane, cross-flow, lift-jet vector directions with respect to the airframe, lift-jet exit flow conditions and non-circular nozzle exit geometry for low aspect ratio nozzles.		

In ground effect, the prediction methodology proceeds logically from the defined aircraft lift-jet exits through the free-jets, jet impingement points, wall-jets, fountain bases (stagnation lines), and fountain impact on the airframe undersurface. The induced suckdown flows are computed from the potential flowfield induced by the turbulent entrainment of both the free-jets and the wall-jets in ground effect and from the free-jets alone out of ground effect. The jet and ground flowfield methodology defines necessary fluid flow properties in the free-jets and wall-jets, the jet impingement regions and fountain base regions, and the fountain upwash for certain classes of multi-jet fountains. The entire methodology is dependent on aircraft and flowfield geometry, and an effort has been made to clarify and simplify geometric requirements.

The methodology emphasizes accurate analytical and empirical modeling of free and wall-jet flows (especially turbulent entrainment); ground wall-jet interactions including the computation of multi-jet stagnation lines and fountain base flow direction; and fountain development and impingement on the airframe under-surface. An analogy between certain classes of multi-jet fountains and self-impinging pairs of circular jets has been used to describe fountain geometry, and to define experimental test configurations which were employed to empirically investigate fountain development and impingement on the airframe under-surface. Techniques for predicting fountain induced forces on the airframe have been developed. An investigation of the effects of protuberances was included in the experimental effort, and techniques for predicting the incremental forces due to the interaction of fountain flows with protuberances were developed.

The induced potential flow field due to turbulent jet entrainment is computed through use of the Douglas Neumann potential flow program. The program has been modified for direct application to the VTOL flowfield computation problem. A User Manual for the modified Douglas Neumann program has been prepared.

The developed methodology represents a state-of-the-art approach for the engineering prediction of ground flowfields, induced suckdown, and fountain formation and development for multi-jet VTOL aircraft.

PREFACE

An analytical program has been conducted for the Naval Air Development Center (NADC) by the McDonnell Aircraft Company (MCAIR) to develop a methodology for the prediction of propulsion induced aerodynamic effects for multi-lift-jet VTOL aircraft operating in the hover mode in and out of ground effect. The methodology emphasizes accurate analytical and empirical modeling of free and wall-jet entrainment, ground wall-jet interaction and subsequent formation of fountains, and fountain impingement on the undersurface of the fuselage/wing. Induced flows about the wing/body are computed through the use of the Douglas Neumann potential flow computer program which has been modified for application to the VTOL problem.

These analytical techniques and empirical correlations have been incorporated into the resulting methodology for force and moment prediction.

The basic analytical work described in this report was funded under contract #N62269-76-C-0086 to MCAIR. Most of the experimental data presented in this report concerning the formation and development of fountains, and the data pertinent to the description of the interaction of the fountain with the fuselage/wing and the effect of protuberances were obtained as part of a MCAIR Independent Research and Development Program during the calendar year 1976.

The program manager of this study was Dr. Donald R. Kotansky and the Principal Investigator was Norbert A. Durando, both of the MCAIR Aerodynamics Department. The technical effort associated with the Douglas Neumann potential flow computations was performed by Dean R. Bristow and Philip W. Saunders of MCAIR Aerodynamics. The Naval Air Development Center Project Engineer was John D. Cyrus.

The authors wish to express their appreciation for the guidance and technical support provided by Chester W. Miller, Chief Technology Engineer - Aerodynamics and Robert B. Jenny, Branch Chief Technology - Aerodynamics, MCAIR.

ACCESSION for	
NTIS	Write Section <input checked="" type="checkbox"/>
DOC	Diff Section <input type="checkbox"/>
UNANNOUNCED	<input type="checkbox"/>
JUSTIFICATION	
BY	
DISTRIBUTION/AVAILABILITY CODES	
100 100 100 100 100 100 100 100	
A I I I I I I I I I	

TABLE OF CONTENTS

<u>Section</u>	<u>Page</u>
PREFACE	iii
LIST OF ILLUSTRATIONS	ix
LIST OF NOMENCLATURE	xiii
1. INTRODUCTION	1
2. FREE-JET AND WALL-JET FLOWFIELDS AND JET ENTRAINMENT CHARACTERISTICS	5
2.1 Free-Jet Flows	5
2.1.1 Reynolds Number Effects	6
2.1.2 Nozzle Pressure Ratio	6
2.1.3 Nozzle Temperature Ratio	11
2.1.4 Nozzle Shape	11
2.1.5 Exit Velocity Profile	15
2.1.6 Exit Turbulence Intensity	17
2.2 The Jet Impingement Region	17
2.2.1 Jet Impingement Angle	18
2.2.2 Ground Plane Momentum Distribution	19
2.2.3 Stagnation Point Displacement	21
2.3 Wall-Jet Flows	21
2.3.1 Wall-Jet Velocity and Thickness Distributions	22
2.3.2 Wall-Jet Entrainment	27
2.3.3 Radial Wall-Jet Momentum	29
3. VISCOUS FLOWFIELD WITHIN THE INNER REGION	31
3.1 Airframe, Jet, and Ground Plane Geometry	31
3.2 Stagnation Line Computation for a Pair of Wall-Jets	32
3.2.1 Development of the Stagnation Line Slope Equations	33
3.2.2 Wall-Jet Pair Stagnation Line Solutions	36
3.2.3 Local Direction of Fountain Flow Above Stagnation Line	39
3.2.4 Stagnation Line Slope Equation for Single Wall-Jet and Uniform Cross-Flow Interaction	41
3.3 Computation of Stagnation Lines for Three or Four Jet Flowfields	43
3.3.1 Geometry for Three or Four Jet Stagnation Line Computation	43
3.3.2 Rotation of Basic Momentum Distribution, $f(\theta)$	44

TABLE OF CONTENTS (Continued)

<u>Section</u>	<u>Page</u>
3.3.3 Determination of Wall-Jet Momentum Flux Entering the Base of a Fountain	45
4. CALCULATION OF THE INDUCED FLOW FIELD	49
4.1 The Douglas Neumann Method	49
4.2 Modifications to Douglas Neumann Program	53
4.2.1 Option to Allow Arbitrary Neumann Boundary Conditions . .	53
4.2.2 Option to Allow Wake-Free Configurations	53
4.2.3 Simplified Geometry Modification Option	53
4.2.4 Coordinate Transformation Option	54
4.2.5 Modified Method of Images Option	55
4.3 Numerical Experiments with Douglas Neumann Program	57
5. FOUNTAIN UPWASH FLOW CHARACTERISTICS	63
5.1 Equivalence Between Symmetric Two-Jet Fountains and Radial Jets	63
5.2 Extension of Two-Jet Fountain Results to Three and Four Jet Configurations	71
5.3 Normal Momentum Flux in Fountains	77
5.3.1 Ideal Normal Momentum Flux in a Fountain Segment	79
5.3.2 Ideal Momentum Fluxes for Two, Three, and Four-Jet Fountains and Optimum Arrangements of Three and Four-Jet Fountains	82
5.4 Asymmetric Two-Jet Fountains	84
6. FOUNTAIN IMPINGEMENT ON A FUSELAGE-WING	93
6.1 Two-Jet Fountain Impingement and Suckdown	93
6.1.1 Fountain Impingement Force	93
6.1.1.1 Pressures Generated by Axisymmetric Wall-Jets Impinging on Each Other	94
6.1.1.2 Pressures Generated by Fountain Impingement on an Airframe Undersurface	97
6.1.2 Calculation of Fountain Suckdown Force	101
6.1.2.1 Fountain Suckdown Force for a Rectangular Plate	103
6.1.2.2 Fountain Suckdown Force for a Trapezoidal Wing	109
6.2 Multiple-Jet Fountain Impingement and Suckdown	112

TABLE OF CONTENTS (Continued)

<u>Section</u>	<u>Page</u>
6.2.1 Calculation of Four-Jet Fountain Impingement Force . . .	114
6.2.2 Calculation of Four-Jet Fountain Suckdown Force . . .	116
6.3 Comparison of Predicted and Experimental Fountain Forces . . .	120
6.3.1 Fountain Impingement Test Apparatus	120
6.3.2 Comparison of Two-Jet Fountain Results	120
6.3.3 Comparison of Four-Jet Fountain Results	126
7. EFFECTS OF PROTUBERANCES ON INDUCED FORCES	129
7.1 Fountain Force Increment Due to Store	129
7.2 Fountain Force Impingement Due to Trailing Edge Flap Deflection	132
8. SUMMARY OF RESULTS AND RECOMMENDATIONS FOR FURTHER STUDY	137
8.1 Free Jet Development	138
8.2 Jet Impingement and Wall-Jets	138
8.3 Fountain Development	138
9. REFERENCES	139
APPENDIX I	143
APPENDIX II	149

RECEIVED 1960-11-10 FILM LIST OF ILLUSTRATIONS

<u>Figure #</u>	<u>Title</u>	<u>Page</u>
1	VTOL Flow Field Interactions In Ground Effect	2
2	Separation of Forces Acting on VTOL Aircraft	
	Hovering In Ground Effect	3
3	Structure of the Axisymmetric Jet	7
4	Non-Dimensional Free-Jet Velocity Profiles.	8
5	Axial Velocity Decay and Spreading Characteristics	
	for Free-Jet.	9
6	Entrained Mass Flow Distribution for Circular Jets.	10
7	Structure of a Rectangular Jet.	12
8	End of Inviscid Core Region for Rectangular Jets.	12
9	End of Inviscid Core and Start of Axisymmetric Decay	
	Region.	13
10	Mass Flow Distribution for Circular and Rectangular Jets.	14
11	Definition of Equivalent Uniform Jet.	15
12	Definition of Nomenclature for Free-Jet and Jet	
	Impingement Region.	18
13	Radial Momentum	20
14	Momentum Flux Distribution for Rectangular Nozzle Jet ($AR > 2$)	
	Core Flow Impingement on Ground Plane	21
15	Stagnation Point Displacement	22
16	Non-Dimensional Wall-Jet Velocity Profile	23
17	Geometry of Two-Dimensional Jet Impingement Computation for	
	Turbulent Flowfield	24
18	Non-Dimensional Wall Jet Velocity Profile at Edge of	
	Impingement Region ($X = W$).	24
19	Variation of Maximum Radial Velocity with Radial Distance-	
	Vertical Jet Impingement.	27
20	Radial Momentum R Dependence	29
21	Control Volume and Geometry for Stagnation Line Momentum	
	Balance	33
22	Wall-Jet Interaction Geometry	34
23	Computed Jet Pair Stagnation Lines in Upper Right Quadrant.	37
24	Computed Stagnation Lines for 4-Jet Arrangement	37

LIST OF ILLUSTRATIONS
(Continued)

<u>Figure #</u>	<u>Title</u>	<u>Page</u>
25	Stagnation Lines for 3-Jet Arrangement.	38
26	Comparison of Measured and Predicted Wall-Jet Stagnation Lines.	38
27	Radial Wall-Jet and Fountain Momentum Relationship.	39
28	Interaction Geometry-Radial Wall-Jet and Uniform Cross Flow.	41
29	Computation of Stagnation Lines	44
30	Rotation of Momentum Distribution $f(\phi)$	45
31	Geometry for Determination of Momentum Flux into Foundation Base (Stagnation Line) Segment A-B	46
32	Douglas Neumann Panel Modeling	50
33	Supercritical Airfoil Pressure Distribution	52
34	Coordinate Transformation Option: Rotation	54
35	Sample Panelled Geometry for the Modified Method of Images Option (Airplane-Free Jet-Wall Jet)	56
36	Panel Model for an Axisymmetric Jet Exhausting from a Flat Jet	58
37	Three Panel Models of an Axisymmetric Jet Exhausting From A Flat Wall	59
38	Pressure Distribution Due to an Axisymmetric Jet.	60
39	Pressure Distribution Due to an Axisymmetric Jet Calculated by the Douglas Neumann Program	60
40	Source Distribution Due to an Axisymmetric Jet Calculated by the Douglas Neumann Program.	61
41	Pressure Distribution Due to an Axisymmetric Jet Calculated by the Douglas Neuman Program	61
42	Idealized Wall Jets and Fountain Turning.	64
43	Equivalence Between Two-Jet Fountain and Radial Jet	65
44	Wall Jet and Fountain Flow Visualization.	67
45	Wall Jet and Fountain Flow Visualization at Different Values of Jet Spacing	68
46	Velocity Profiles in Two-Jet Fountain $S/D_{je} = 8$	69
47	Radial Jet and Fountain Velocity Profiles	71
48	Radial Jet and Fountain Spreading Rates	72
49	Spreading Rate for Fountain, MCAIR Radial Jet Data and Radial Jets Tested by Witze	72
50	Peak Velocity In a Fountain and a Single Radial Jet	73

LIST OF ILLUSTRATIONS
(Continued)

<u>Figure #</u>	<u>Title</u>	<u>Page</u>
51	Idealized Wall Jets - Four Symmetric Jets	75
52	Equivalence Between Four-Jet Fountain and Sectors of Four Radial Jets.	75
53	Rectangular Arrangement of Four Equal, Perpendicular Jets.	76
54	Isosceles Triangular Arrangement of Three Equal, Perpendicular Jets.	77
55	Isosceles Triangular Arrangement of Three Equal Jets with Fountain Segments Intersecting Outside the Inner Region.	80
56	Wall Jets and Equivalent Radial Jet for a Fountain Segment. . .	81
57	Normalized Ideal Fountain Vertical Momentum Flux for Two, Three, and Four-Jet Fountains	85
58	Two-Jet Fountain Configuration.	85
59	Fountain Geometry for Perpendicular Jets of Unequal Thrust.	87
60a	Conical Fountain Semiapex Angles as a Function of Jet Momentum Ratio.	88
60b	Conical Fountain Apex Location As a Function of a Jet Momentum Ratio.	89
61	Approximation to Calculated Stagnation Lines by Hyperbolas. . .	91
62	Idealized Radial Jet Splitting and Turning Upon Impingement on a Rectangular Plate	94
63	Peak Pressure Distributions Beneath Fountain.	96
64	Calculation of Fountain Impingement Force	98
65	Fountain Impingement on a Rectangular Plate (Origin of Suckdown Force)	102
66	Fountain Mass Flow Diagram for Impingement at Midehord of a Rectangular Plate	104
67	Calculated Fountain Impingement and Suckdown Forces on a Rectangular Plate	109
68	Fountain Mass Flow Diagrams for Impingement at Station X_G - Trapezoidal Wing	110

LIST OF ILLUSTRATIONS (Continued)

<u>Figure #</u>	<u>Title</u>	<u>Page</u>
69	Idealized Streamline Pattern for a Square, Four-Jet Fountain Impinging on the Bottom of a Flat Plate	113
70	Four-Jet Fountain Impingement Footprint	115
71	Idealized Flow Directions on Trapezoidal Wing Undersurface After Four-Jet Fountain Impingement	117
72	Mass Flow Diagram In X-Z Plane.	118
73	Mass Flow Diagrams in (Y-Z) Plane	119
74	Fountain Generator Schematic.	121
75	Fountain Impingement Test Apparatus	122
76	Calculated Jet Impingement Force Compared to MCAIR IRAD Test Data Single Annular Jet, Low Wing.	123
77	Variation of Normal Force with Height Above Jet Origin.	125
78	Variation in Theoretical and Experimental Normal Force Coefficient with Height Above Nozzle Centerline	127
79	Comparison Between Theory and Experiment-Four Radial Jets	128
80	Calculation of Normal Force Increment Due to Underwing Stores.	130
81	Theoretical and Experimental Normal Force Coefficient With Simulated Stores	132
82	Calculation of Normal Force Increment Due to Flap	133
83	Momentum Flux Diagram for Computing Fountain Force Increment Due to Trailing Edge Flap Deflection.	134
84	Theoretical and Experimental Normal Force Coefficients with Full-Span Flaps	135
I-1	Euler Angles.	144
I-2	Nozzle Thrust Deflection Angle and Splay Angle.	146
II-1	Jet Path Plane Definition	150

LIST OF NOMENCLATURE

AR_{je}	Nozzle exit area aspect ratio
b	Rectangular nozzle exit dimension, plate dimension
C	Coefficient
C_p	Pressure coefficient
c	Rectangular nozzle exit dimension, plate dimension
D_{je}	Nozzle exit diameter
d	Pipe diameter used for fountain simulation
E	Jet entrainment rate
F	Force, normal force
$f(\phi)$	Momentum distribution about jet impingement region
$F'(\phi) = \gamma_A f(\phi)$	Corrected momentum distribution about jet impingement region
H	Nozzle exit height above ground
L	Nozzle centerline spacing
ℓ_1, ℓ_2, ℓ_3	Direction cosines
M	Integer index for angular measurement
\dot{M}	Momentum
\dot{M}_j	Jet momentum
\dot{M}_{je}	Jet momentum at nozzle exit
\dot{m}	Mass flow
\dot{m}_{jT}	Total jet mass flow
\dot{m}_{je}	Jet mass flow at nozzle exit
\dot{m}_{add}	Entrained jet mass flow = $\dot{m}_{jT} - \dot{m}_{je}$
m_1, m_2, m_3	Direction cosines
N	Normal distance above ground plane, number of panels in Douglas Neumann potential flow program
N_ℓ	Normal distance to stagnation line in ground plane
N_5	Normal distance to $U_{max}/2$
NPR	Nozzle pressure ratio

LIST OF NOMENCLATURE (Continued)

n_1, n_2, n_3	Direction cosines
p	Pressure
R	Radius measured from real or apparent jet impingement stagnation point, radius from fountain virtual origin
R_I	Ground radius at edge of impingement region
ΔR_I	Radial correction to apparent jet impingement stagnation point
R_{ej}	Jet exit Reynolds number
r	Radius measured along upper surface or wall
r_j	Jet radius
$r_j \sqrt{2}$	Radius of free jet from jet centerline to location of 1/2 jet centerline velocity
$r_j \sqrt{2}I$	Radius to 1/2 jet centerline velocity at impingement point
S	Distance between impinged jets, nozzle centerline spacing
$T_{o_{je}}/T_\infty$	Nozzle temperature ratio
U	Wall-jet velocity
V_∞	Freestream velocity
V	Jet exit velocity, jet velocity, fountain velocity
x, y, z	Cartesian coordinates
x_1, y_1, z_1	Input data coordinates for Douglas Neumann program
$\Delta x, \Delta y, \Delta z$	Coordinate translations, displacements
Z	Jet centerline coordinate
α_o	Conical fountain semi-apex angle
α_{jI}	Jet impingement angle measured with respect to ground surface
γ	Wing leading edge sweep angle, direction in ground plane of projection of negative of jet main velocity vector at impingement point
γ_A	Momentum correction
δ_F	Flap deflection angle

LIST OF NOMENCLATURE (Continued)

ζ	Normalized coordinate in jet deflection plane (Fig. II-1)
Θ	Euler angle
θ	Stagnation line slope, fountain or jet azimuthal angle measured from vertical about virtual origin
κ	Fountain velocity or momentum directional angle
ξ	Normalized coordinate in jet deflection plane (Fig. II-1)
ρ	Density
σ_{je}	Jet deflection angel at nozzle exit measured with respect to freestream direction
σ	Source strength density
ϕ	Euler angle
ϕ	Azimuthal angle measured around periphery of jet impingement region. For $\alpha_{ij} \neq 90^\circ$, $\phi = 0$ in direction of horizontal component of jet mean flow
ϕ'	Computational polar angle for stagnation line computation between a pair of wall-jets
ψ	Euler angle, radial momentum parameter used in Reference 2

Subscripts

1, 2, 3, 4	Associated with lift-jet 1, 2, 3 or 4
A	Aft, Area
c	Centerline, cross-flow
e	Jet exit station, equivalent
F	Forward, fountain
I	Impingement region
J	Jet
max., m	Maximum value, mean value
N, n	Normal to surface, normal
o	Total (fluid properties), conical geometry
R	Reference, rectangular, radial
s	Suckdown
st	Stores

LIST OF NOMENCLATURE (Concluded)

T, t, TOT	Total, tangential
$v/2$, $1/2$, 5	Half-velocity point
x, y, z	Cartesian coordinate direction
∞	Infinity, ambient

1. INTRODUCTION

The design of VTOL aircraft equipped with powered lift-jet systems requires a knowledge of the complicated flowfield produced by such devices over a wide range of aircraft operating conditions. Of particular importance are the flowfield interactions resulting from the operation of these types of aircraft in the hover mode out of ground effect and in proximity to the ground where strong interactions frequently occur between the lift-jet streams, the airframe surfaces, and the ground. These interactions usually result in the introduction of forces on the airframe which can be positive (providing additional lift) or negative. Thus, a propulsion system designed without taking into account the induced forces may not provide sufficient thrust for an adequately controlled takeoff without a reduction in desired payload. In addition to these induced net loads, situations are encountered where unfavorable moments are produced on the airframe resulting in significant stability and control problems.

The induced forces (and moments) in and out of ground effect usually result from one of two reasonably well defined viscous flow phenomena: jet entrainment and the formation of jet flow fountains. Jet entrainment causes otherwise static air to be set into motion, resulting in locally reduced static pressures on nearby airframe under-surfaces thus introducing negative aerodynamic loads. The jet entrainment effect occurs both in and out of regions influenced by the presence of the ground but is frequently accentuated as the distance between the jet source (nozzle exit) and the ground is reduced, largely because of the proximity of the additional entrainment resulting from the ground wall-jets.

Although the jet entrainment effect occurs both in and out of ground effect, the formation of jet-flow fountains requires an impingement surface and, therefore, is peculiar to operation close to the ground. The formation of fountains is also configuration-dependent in that multiple jets are required and the jet impingement points, relative strengths of the jets, and jet impingement angles are strongly influential factors. The upward convection of jet flow in the fountains usually results in a positive aerodynamic lift, caused by the positive pressurization of airframe under-surfaces containing and deflecting the fountain flow. Because of the upward convection of the lift-jet flow in the fountains, a degradation of propulsion system performance frequently results through exhaust-gas ingestion. In this respect, fountains can be detrimental to VTOL aircraft performance in ground proximity.

Generally, the aerodynamics of VTOL aircraft are influenced by a number of geometric parameters and by the viscous (turbulent) nature of the local flow-field. Significant VTOL hover flowfield interactions and their resulting effects on aerodynamic performance in ground effect are summarized in Figure 1. The comprehensive theoretical prediction of these flowfields and resulting aerodynamic forces for arbitrary aircraft configurations is undoubtedly many years off, and it may never be economically feasible to rely solely on theoretical predictions. However, it is possible with present knowledge to synthesize useful solutions with empirical information for well-defined flowfields about airframe components of significant current interest. It is to this objective that the work described herein was directed: the prediction of lift jet (primary) and induced flowfields, including induced forces and moments about arbitrary aerodynamic shapes in and out of ground proximity for a well defined set of flow conditions. This study was accomplished through the synthesis of new and existing analytical techniques and empirical correlations in use at the McDonnell Aircraft Company (MCAIR) and the McDonnell Douglas Research Laboratories (MDRL).

Problems	Causes
✓ • Lift Loss (Suck-Down)	→ Turbulent Jet Entrainment
✓ • Lift and Moment Sensitivity to Pitch and Roll	→ Deflection of Jets and Fountains by Impingement
✓ • Lift and Moment Sensitivity to Cross-Winds	→ Deflection of Jets and Fountains by Cross-Winds and Cross-Wind Induced Aerodynamic Loads
• Engine Thrust Loss From Exhaust Gas Ingestion	→ Fountain, Cross-Wind and Buoyant Convection of Hot Exhaust Gas

✓ Problems addressed in this study.

QP77 0374 27

FIGURE 1
VTOL FLOW FIELD INTERACTIONS IN GROUND EFFECT

The combined methodology was developed by proceeding logically from the lift-jet exits through the viscous flowfield including the free-jets, wall-jets, wall-jet stagnation lines, fountain formation, and fountain impingement on the airframe in ground effect. In and out of ground effect, jet entrainment induced flowfields are obtained from computations of induced potential flows about the airframe as established by empirical free and wall-jet entrainment characteristics where appropriate. Although the viscous flows do influence

the induced potential flow through specification of jet surface entrainment velocities, the induced potential flow effect on the complete flowfield is not iterated or altered to compute additional interactive flowfield effects. The basic separation of suckdown and fountain forces shown in Figure 2 is inherent in the formulation of the resulting methodology.

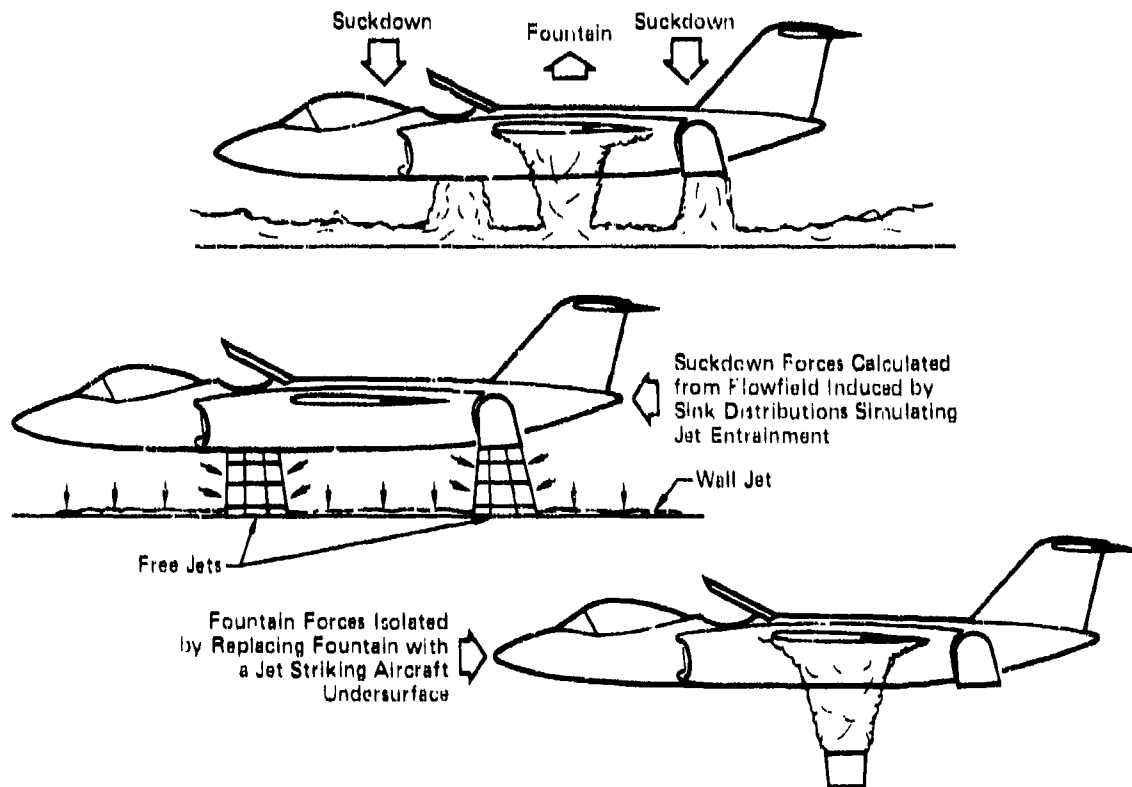


FIGURE 2
SEPARATION OF FORCES ACTING ON VTOL AIRCRAFT HOVERING
IN GROUND EFFECT

GP77-0374-1

2. FREE-JET AND WALL-JET FLOWFIELDS AND JET ENTRAINMENT CHARACTERISTICS

The analytical and empirical modeling of the viscous (turbulent) flows including the free-jets, jet impingement regions and wall-jets is described in the following subsections. This description of the fluid mechanics of these flow phenomena provides a means for the prediction of the properties of these flows including flow geometry, velocity distribution, momentum flux distribution and mass averaged temperature. Total pressures, if required, are obtained from knowledge of the velocity distributions in the constant pressure (ambient) free-jet and wall-jet regions. The resulting prediction methodology incorporates a number of theoretical, empirical and semi-empirical descriptions of the individual flow regions involved. The emphasis technically, however, is on the use of high quality empirical data which have been incorporated into the prediction methodology wherever possible in preference to purely theoretical predictions.

2.1 Free-Jet Flows

It is expected that for VTOL aircraft in hover, the lift-jets will retain free-jet characteristics, i.e., they will be to first order unaffected by pressure gradients, for some fraction of the distance between the nozzle exit and the ground plane. Experience based on wind tunnel tests and practical considerations have indicated that the distances between nozzle exit and ground plane (H/D_{je}) to be considered, lie in the range

$$0.5 \leq H/D_{je} \leq 15$$

Consequently, interest in the properties of free turbulent jets is focused on the same range of nozzle diameters downstream of the exit.

The velocity discontinuity at the exit of a jet nozzle is smoothed out by viscous effects within a thin shear layer. The shear layer is highly unstable and develops from the nozzle lip as a free turbulent flow. For some distance downstream of the nozzle exit plane, the jet retains a potential core flow surrounded by a sheath of highly turbulent fluid, where mixing between the jet and surrounding fluid takes place. This core flow region is eventually "consumed" by the spreading turbulent mixing, and the jet eventually becomes fully turbulent. The mass flow in the turbulent region increases along the jet, and flow continuity requires that this excess mass flux be supplied from the surrounding medium. The rate at which the jet entrains external air is found to be different in the core flow (or potential core) region from

that in the fully turbulent region. In the former, entrainment is due to a shear layer which separates two regions of approximately constant velocity. In the latter, as the turbulent region spreads, the jet centerline velocity decays. The distance from the nozzle at which the flow becomes fully turbulent is therefore an important parameter in the calculation of airframe suckdown forces due to free-jet entrainment.

The axial development of free turbulent jets, and consequently their entrainment distribution, generally depends on the following parameters:

- o Jet exit Reynolds number - Re_j
- o Nozzle pressure ratio - $NPR = P_{o,jc}/P_\infty$
- o Nozzle temperature ratio - $T_{o,j}/T_\infty$
- o Nozzle shape
- o Exit velocity profile
- o Exit turbulence intensity

2.1.1 Reynolds Number Effects - For the relevant Reynolds number range, turbulent transport dominates the flow. The shear layer and jet develop as free turbulent flows unconstrained by rigid boundaries, and consequently Reynolds number effects are negligible (Reference 1).

2.1.2 Nozzle Pressure Ratio - The nozzle pressure ratios considered range from subsonic ($NPR = 1.05$) to mildly underexpanded ($NPR = 2.2$). These are representative of current lift-fan or lift-jet propulsion systems. At the critical pressure ratio 1.89, the nozzle chokes, and since only convergent nozzles are considered, larger values of NPR will produce underexpanded jets. For subsonic jets, the effects of NPR (and temperature ratio) will be reflected in a jet density which is different from ambient. The effect of jet to ambient density ratio upon entrainment characteristics is taken into account by currently available entrainment data. For underexpanded jets, the exit pressure is relieved by a supersonic expansion. Overexpansion results, and the flow is recompressed by a series of shock waves. Reference (2) identifies the following flow patterns and associated pressure ratios:

- a. $1.05 \leq NPR \leq 1.89$ - no shocks, exit pressure approximately equal to ambient
- b. $1.89 \leq NPR \leq 2.08$ - weak expansion waves and normal shocks generated in jet
- c. $2.08 \leq NPR \leq 3.79$ - "diamond" shock pattern
- d. $3.79 \leq NPR$ - strong shocks develop at center line.

The nozzle pressure ratios considered in this study include the first three possibilities. Cases (b) and (c) are complicated by the fact that the

core flow jet boundary is distorted by the expansion and recompression process. The turbulent shear layer thus develops along a distorted boundary, with a non-uniform velocity in the core flow region. In addition, shock waves penetrate the shear layer and may be expected to affect its development. Thus, although turbulent dissipation will dominate and the jet will eventually be equivalent to a subsonic jet, the flow in the neighborhood of the nozzle is extremely complicated. Typical normalized jet velocity profiles and axial decay and spreading characteristics are given for jets within NPR ranges (a), (c) and (d) above in Reference (2). Characteristics of jets in the NPR range (b) are taken to be represented adequately by those of NPR range (a).

Axisymmetric subsonic jets with uniform exit velocity profile have been studied extensively. Three main flow regions have been identified and are indicated in Figure 3. For some distance downstream of the nozzle, the jet retains a region of core flow. After the jet becomes fully turbulent, the maximum velocity along the jet axis begins to decay. For values of Z/D_{je} in excess of 12, the maximum velocity in the jet decays inversely with axial distance, and the turbulent region grows linearly. The core flow region of the jet persists to values of Z/D_{je} of approximately 7 at which point the axial velocity profiles become self similar.

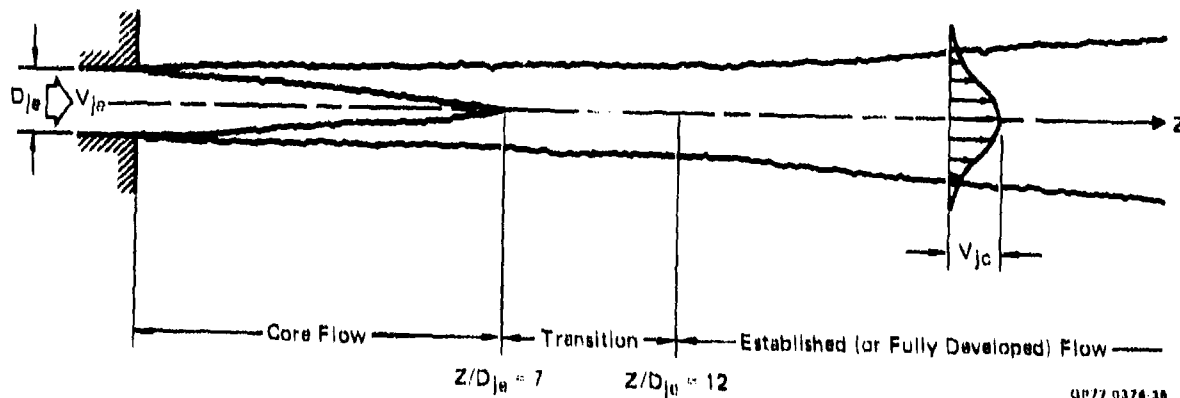


FIGURE 3
STRUCTURE OF THE AXISYMMETRIC JET

Free-jet development can be adequately described by the behavior of characteristic jet velocities and lengths and the self-similar properties of

fully developed jets of NPR range (a) of Reference 2. Figure 4 presents non-dimensional velocity profiles for axisymmetric free-jets as a function of Z/D_{je} . For $Z/D_{je} \geq 7$, the velocity profiles are self-similar, and the shape no longer varies with Z . Figure 5 presents the behavior of the jet characteristic lengths and velocities with axial distance Z/D_{je} . The velocity profiles and physical geometry of the free-jet can be obtained from these two figures up to the beginning of the jet impingement region in the flowfield between the airframe under-surface and the ground plane.

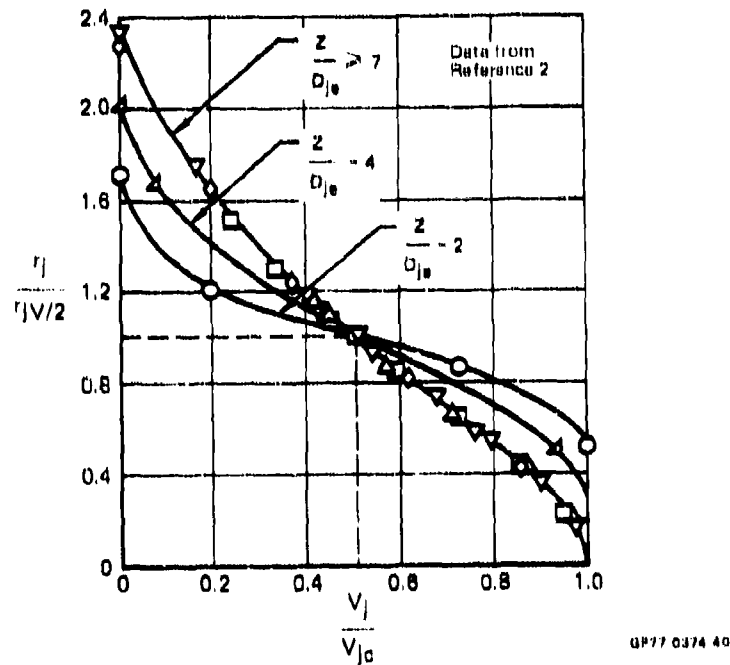
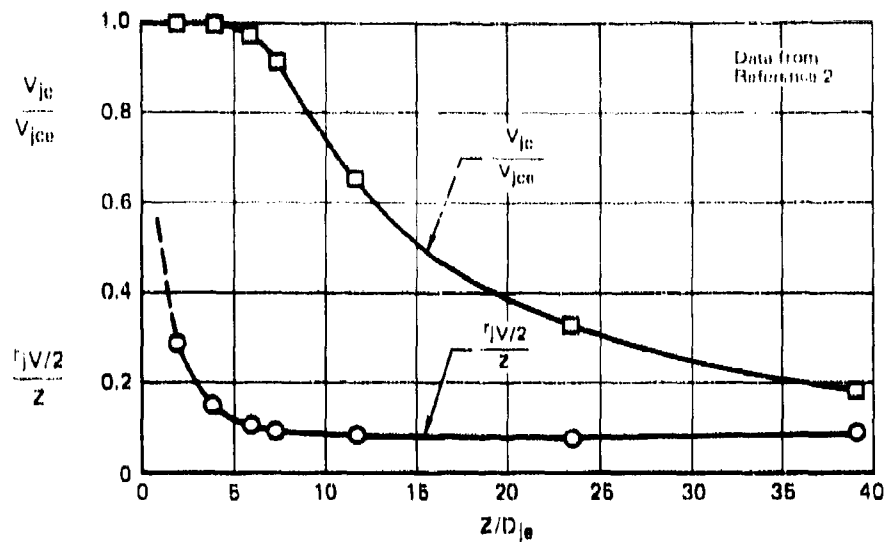


FIGURE 4
NON-DIMENSIONAL FREE-JET VELOCITY PROFILES



OP77 0374 41

FIGURE 5
AXIAL VELOCITY DECAY AND SPREADING CHARACTERISTICS FOR FREE-JET

The entrainment rate

$$E = d(\dot{m}_{JT}/\dot{m}_{j0})/d(Z/D_{j0}) \quad (1)$$

describes the amount of additional ambient fluid that is pulled into the jet by turbulent mixing as the jet develops along its axis. Figure 6 is a summary of several measured and estimated turbulent jet mass flow distributions, where

$$\dot{m}_{add} = \dot{m}_{JT} - \dot{m}_{j0}$$

and \dot{m}_{add} denotes the entrained mass flow.

Most authors consider the data of Ricou and Spalding (Curve C) to represent the most accurate measurement of mass entrainment in the fully developed region. Hill's data (Curve A) agrees well with Curve C in the region of fully developed flow, and also includes measurements in the core flow region. The change in entrainment rate between the core flow and the fully developed flow region is evident in the data. Curve A shows that the initial entrainment rate is not constant. On the other hand, Kleis and Foss' data (Curve B) show a constant initial entrainment rate, with a break in slope at $(Z/D_{j0}) = 5.3$. Curve B is in good agreement with the Ricou and Spalding data in the fully developed flow region. Curve E shows a smaller slope change between the core and the fully developed

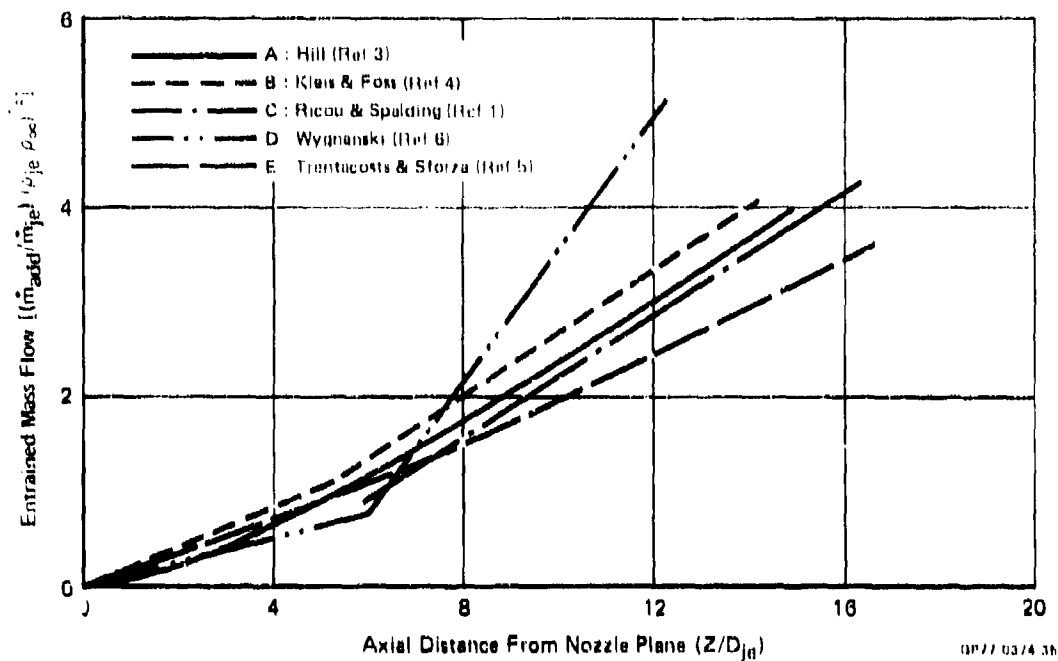


FIGURE 6
ENTRAINED MASS FLOW DISTRIBUTION FOR CIRCULAR JETS

flow regions. In the fully developed flow region, the slope for Curve E is substantially lower than that measured by other investigators. Most of the curves in Figure 6 change slope in the range

$$5 < (Z/D_{je}) < 6.$$

In the analysis by Wygnanski (Reference 6), $(Z/D_{je}) = 6$ is taken to be the beginning of the fully developed flow region. The transition zone is neglected, and a core flow entrainment rate is used up to $(Z/D_{je}) = 6$, with a fully developed entrainment rate for $(Z/D_{je}) > 6$. Wygnanski's entrained mass distribution is indicated by Curve D in Figure 6. His initial entrainment rate is reasonably accurate; the termination of the initial region at $Z/D_{je} = 6$ is in good agreement with Curve B. However, the entrainment rate in the fully developed region is excessive.

In the present study, the data of Kleis and Foss (curve B) have been selected to establish the entrainment rate for subsonic circular jets, with the following results:

$$\frac{d \left[\left(\dot{m}_{jT} / \dot{m}_{je} \right) (\rho_{je} / \rho_w)^{1/2} \right]}{d(Z/D_{je})} = 0.21 \quad \text{for } 0 \leq Z/D_{je} \leq 6 \quad (2)$$

and

$$\frac{d \left[\left(\dot{m}_{jT} / \dot{m}_{je} \right) (\rho_{je} / \rho_w)^{1/2} \right]}{d(Z/D_{je})} = 0.32 \quad \text{for } 6 \leq Z/D_{je} \quad (3)$$

2.1.3 Nozzle Temperature Ratio - The effects of nozzle temperature ratio are taken into account in determining jet exit velocity, V_{je} , and jet exit density, ρ_{je} , which in turn affects the free-jet entrainment rate as shown in Figure 6. Buoyancy effects in the free-jets and wall-jets are not considered in the resulting methodology.

2.1.4 Nozzle Shape - Reference 5 contains data on the characteristics of subsonic jets exhausting from rectangular nozzles. Figure 7 defines the nozzle geometry and general structure of the flow. Three different regions are identified according to the rate of decay of the maximum jet velocity. (See insert in Figure 7). In the core flow region, the maximum velocity is equal to the jet exit velocity. In the characteristic decay region, the flow is fully turbulent, but the decay rate of the maximum velocity with axial distance depends on the nozzle aspect ratio AR_{je} . In the axisymmetric decay region, the maximum velocity decays as $\sim (1/Z)$, as in an axisymmetric jet. The velocity profile, however, is not axisymmetric. Finally, the profile does become axisymmetric in what has been labeled the fully axisymmetric flow region. All memory of the nozzle shape has then been lost, and the jet structure is analogous to that of a fully developed axisymmetric jet.

In lift jet VTOL aircraft, approximately rectangular jets are generated primarily by groups of lift-jet engines geometrically clustered together. Thus, a maximum of $AR_j = 4$ is considered. For convenience in relating aircraft and jet geometries, the nozzle aspect ratio is defined to be greater than one when the long nozzle dimension is perpendicular to the aircraft plane of symmetry, and less than one when it is parallel to the plane of symmetry. Thus, the minimum aspect ratio to be considered is approximately $AR_j = 0.25$.

Reference 5 defines the end of the core flow region and the beginning of the axisymmetric decay region as a function of nozzle aspect ratio. Data for the end of the core flow region have been replotted from Reference 5 in Figure 8, in a slightly different form. Figure 8 also includes data from Reference 7, which were presented in Reference 5. For a square nozzle

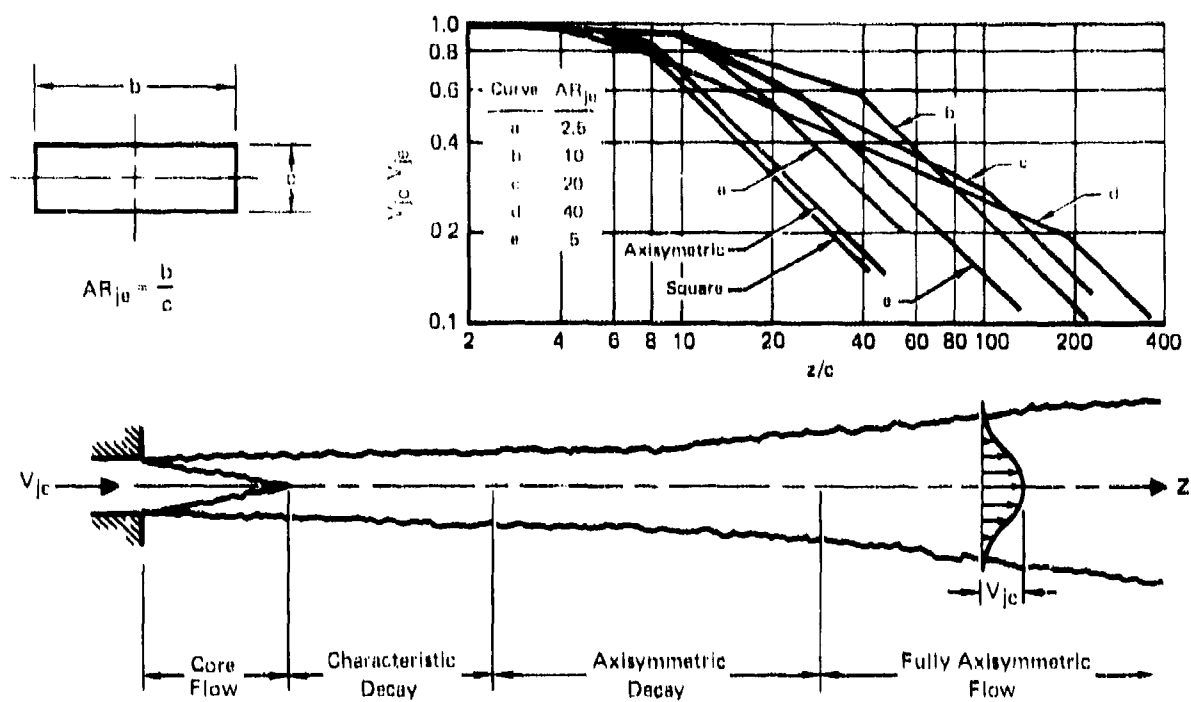
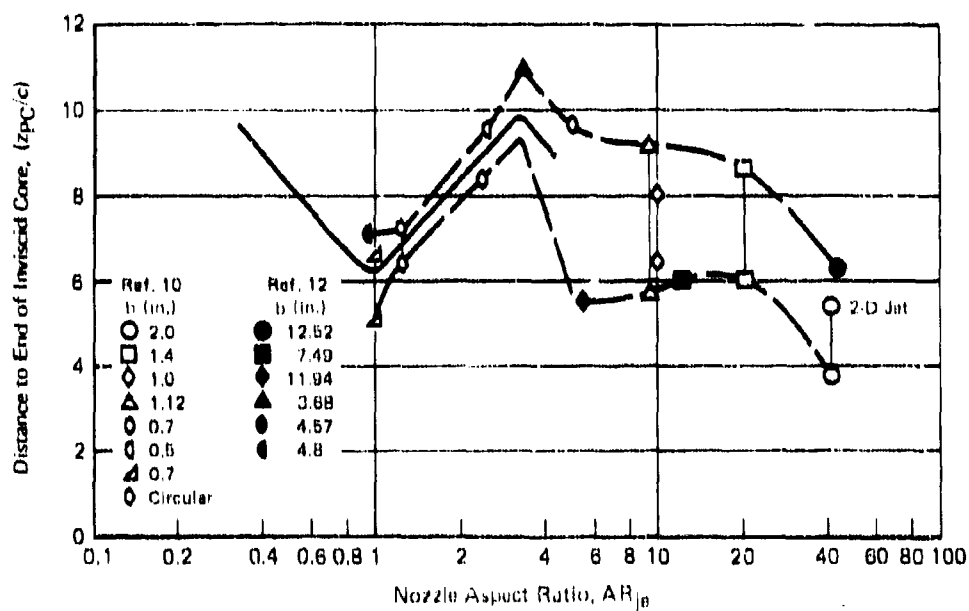


FIGURE 7
STRUCTURE OF A RECTANGULAR JET

QP77 0374 32



QP77 0374 33

FIGURE 8
END OF INVISCID CORE REGION FOR RECTANGULAR JETS

($AR_{je} = 1$), the core flow region has been shown to terminate at $z_{pc}/c = 6.2$. For a circular jet, the indicated value of 6.8 is somewhat higher than the value of 6 reported by other authors. Although there is considerable data scatter, an increase in core flow length with nozzle aspect ratio is indicated, peaking at $AR_{je} = 3.4$ and subsequently decreasing towards 6, the value used in Reference 6 for two-dimensional jets. Figure 9 repeats the average empirical curve for (z_{pc}/c) shown in Figure 8, and indicates the dependence of the onset of axisymmetric decay on nozzle aspect ratio.

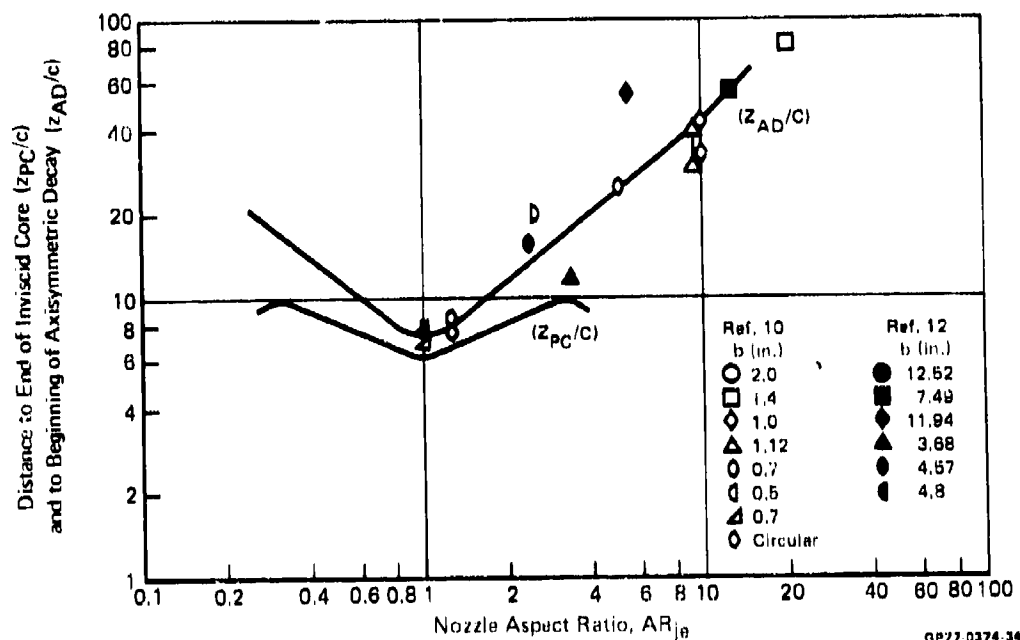


FIGURE 9
END OF INVISCID CORE AND START OF AXISYMMETRIC DECAY REGION

The boundaries of the various jet regions depicted above are used to establish regions for the free-jet entrainment rates. Reference 5 indicates that the entrainment rate for an $AR_{je} = 10$ jet initially is higher than that for a circular jet, but at the onset of axisymmetric decay, the entrainment rates are the same.

For rectangular exit area jets, two entrainment rates are used. One is valid in the core flow region, and one is valid in the fully developed turbulent region. In the core flow region, it is assumed that

$$E_R = \frac{E}{2\pi} \frac{P_R}{r_{je}} \quad (4)$$

where E_R - entrainment rate for rectangular nozzle

P_R - perimeter of rectangular nozzle

E - entrainment rate for circular jet

For the fully developed turbulent zone, the results of Reference 5 will be used. Reference 5 shows the mass flow distribution for a circular jet, and for an aspect ratio 10 rectangular jet. These data are plotted in Reference 5 in inches downstream of the nozzle exit. Figure 10 shows the same data plotted in terms of axial distance normalized by a diameter

$$d_f = 2 \sqrt{\frac{bc}{\pi}} \quad (5)$$

Satisfactory correlation is obtained, indicating that for the fully developed turbulent region, an entrainment equal to that for a circular jet whose diameter is given by Equation (5) can be used.

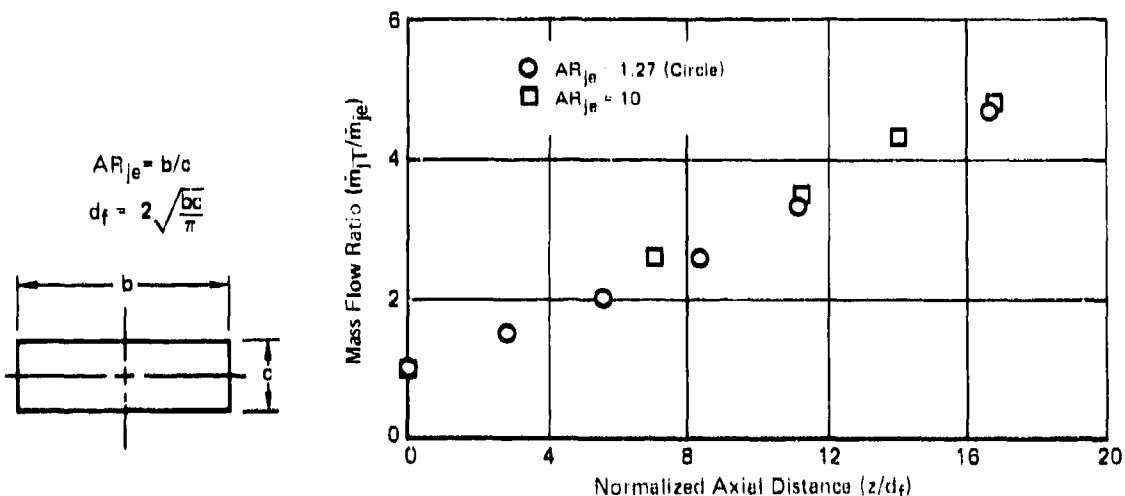


FIGURE 10
MASS FLOW DISTRIBUTION FOR CIRCULAR AND RECTANGULAR JETS

In order to fully specify the entrainment distribution for a rectangular jet, the length of the core flow region must be defined. This can be accomplished by the average curve in Figure 8 which is based on the data of Reference 5. This curve shows the length of the core flow region (normalized by the nozzle chord c) as a function of nozzle aspect ratio, for the range of interest

$$1 \leq AR_{je} \leq 3.$$

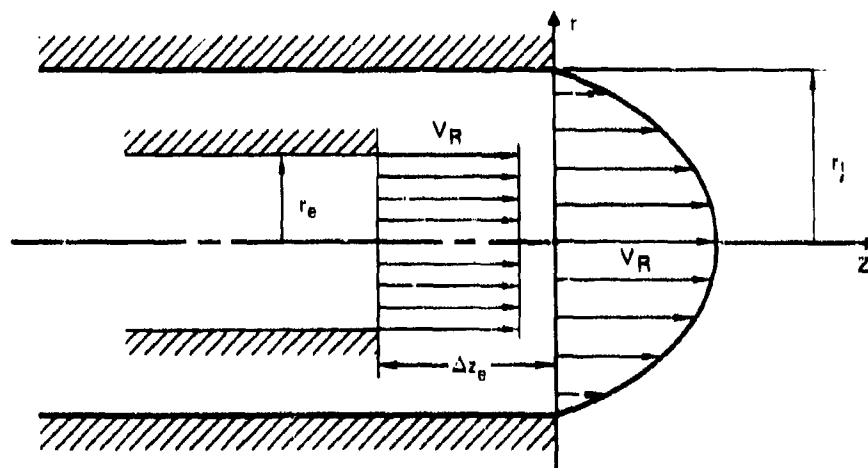
2.1.5 Exit Velocity Profile - Circular jets with non-uniform exit conditions are analyzed by defining equivalent uniform jets. The analogy has been described in References 8 and 9. Let

$$\dot{m}_{jT} = 2\pi \int_0^{r_j} \rho_j V_j r dr \quad (6)$$

and

$$\dot{M}_j = 2\pi \int_0^{r_j} \rho_j V_j^2 r dr \quad (7)$$

where \dot{m}_{jT} and \dot{M}_j denote the actual jet mass and momentum fluxes, respectively. For the non-uniform jet a reference velocity is chosen, denoted by V_R and shown in Figure 11. This should be the maximum in the profile, which in most cases will also be the centerline velocity. An equivalent jet of radius r_e , located at a distance Δz_e from the origin on Figure 11, is defined. The equivalent radius and location are chosen such that, for a uniform velocity distribution V_R , the equivalent and actual jets will have the same mass and momentum fluxes.



QR77 037A 37

FIGURE 11
DEFINITION OF EQUIVALENT UNIFORM JET

Thus :

$$\dot{m}_{jT} = 2\pi \int_0^{\infty} (\rho V)_{\Delta z_e} r dr \quad (8)$$

and

$$\dot{M}_j = 2\pi \int_0^{\infty} (\rho V^2)_{\Delta z_e} r dr. \quad (9)$$

Since momentum is conserved in a jet, Equation (9) may be written as

$$2\pi \int_0^{r_j} \rho_j V_j^2 r dr = \pi r_e^2 \rho_j V_R^2.$$

A momentum distortion coefficient is defined

$$n_2 = \frac{\dot{M}_j}{\pi \rho_j V_R^2 r_j^2} \quad (10)$$

which, when substituted in the above equation, yields

$$r_e = r_j \sqrt{n_2}. \quad (11)$$

A mass distortion coefficient is defined as:

$$n_1 = \frac{\dot{m}_{jT}}{\pi \rho_j V_R r_j^2} \quad (12)$$

and Equation (8) may then be written as:

$$n_1 = \frac{2}{r_j^2 V_R} \int_0^{\infty} (V)_{\Delta z_e} r dr. \quad (13)$$

In References 8 and 9, the velocity profile in the core flow region of a uniform jet is described by an equation introduced by Warren in Reference 10.

$$\frac{V}{V_R} = \exp \left[-n_2 \frac{r^2 - r_c^2}{r_{v/2}^2 - r_c^2} \right] \quad (14)$$

where

r_c = inner radius of the shear layer
(for $r = r_c$; $V/V_R = 1$)

$r_{v/2}$ = radius at which $V/V_R = \frac{1}{2}$.

Using Equations (11) and (14) in (13), the equivalent jet velocity profile may be integrated to yield

$$\frac{n_1}{n_2} = \frac{1}{r_c^2} \left[r_c^2 + \frac{r_{v/2}^2 - r_c^2}{\ln 2} \right] z = \Delta z_c \quad (15)$$

This constitutes an implicit equation for Δz_c , provided that the dependence of $r_{v/2}$ and r_c on z is known. In Reference 10, Warren has obtained the relationship between $r_{v/2}$, r_c , and z from a solution of the jet momentum equation and an empirical value of the eddy viscosity coefficient. The solution leads to a complicated, non-linear relationship between $r_{v/2}$, r_c , and Δz_c . In Reference 8, Witze has represented this relationship by a polynomial, which allows direct calculation of Δz_c . Witze's equation is:

$$\Delta z_c = r_c \left[-4.057 \left(\frac{n_1}{n_2} \right)^2 + 24.68 \left(\frac{n_1}{n_2} \right) - 20.62 \right]. \quad (16)$$

In summary, a circular jet with non-uniform exit velocity has been replaced by an equivalent uniform velocity jet whose exit radius is related to that of the real jet by Equation (11), and whose exit is displaced from the real jet exit by an amount given by Equation (16). The core flow length and entrainment distributions discussed in Section 2.1.2 may then be used for this equivalent uniform jet. If the exit velocity distribution is known in detail, the distortion coefficients n_1 and n_2 may be calculated directly. If the exit velocity distribution is unknown, Reference 8 contains calculations of n_1 and n_2 for the thin boundary layer case and for fully developed pipe flow. These values may be used to estimate the effects of jet exit profile distortion.

2.1.6 Exit Turbulence Intensity - The experiments of Reference 4 included the variation of turbulence intensity at the exit of a subsonic circular nozzle. The rms value of the axial velocity fluctuation at the exit was varied from 1.2 to 3.6% of the exit velocity, with no measurable effect on jet mass flow distribution or on the termination of the core flow region. The data does show a small influence of turbulence intensity on the rate of axial velocity decay.

2.2 The Jet Impingement Region

The accuracy of description and modeling of the complex fluid flow interactions within the inner region has been greatly enhanced by the extensive study of free jet impingement by Donaldson and Snedeker, Reference 2. The experimental measurements reported in Reference 2 allow an empirical definition of the velocity, momentum, and mass entrainment distributions for the turbulent wall-jets including the very significant effect of oblique jet

2.2.1 Jet Impingement Angle - The jet impingement angle, α_{ji} , is defined as the angle between the ground surface and the jet-centerline extended downwash to the ground surface. For normal (perpendicular) impingement on the ground plane, $\alpha_{ji} = 90^\circ$. In the general hover flowfield, α_{ji} is a function

of many variables including aircraft roll and pitch angle, nozzle vector and splay angle, and the deflection of the lift jet centerline by cross-winds. Jet path deflections due to cross-winds are described by a relationship presented in Reference 12:

$$\xi = \left[\frac{|V_m|}{|V_{je}|} \right]^{2.6} \xi_0^3 + \xi_0 \tan \theta_0 \quad (17)$$

where ξ and ξ_0 are distances (see Figure 11-1) which have been normalized by the jet diameter, and θ_0 is the complement of the angle between the jet velocity vector and the freestream velocity vector. This equation has been used with good results in studies of jet-induced effects in transition flight, (Reference 13).

2.2.2 Ground Plane Momentum Distribution - The character of the ground wall-jet flowfield is governed largely by the location of the impinged jet stagnation points and the azimuthal distribution of the impinged jet radial momentum. For normal impingement of circular or nearly circular jets, the resulting radial momentum distribution in the wall-jet is uniformly distributed about the impingement stagnation point. However, for non-vertical jet impingement, the actual azimuthal distribution of momentum is non-uniform and heavily biased toward the direction of the horizontal component of mean jet flow. Very detailed measurements of momentum distributions about inclined impinging circular jets were accomplished by Donaldson and Snedeker, and their empirical data are shown for two values of H/D_{je} and two values of jet impingement angle in Figure 13. Shown also in Figure 13, are two solid lines representing analytical curve fits of these data which describe the momentum distribution about the jets as a function of azimuthal angle ϕ . The equations for $f(\phi)$ are:

$$0^\circ \leq \phi \leq 45^\circ$$

$$f(\phi) = 1.0 + (0.535 \cos 4\phi + 0.885) \left(\frac{90^\circ - \alpha_{j1}}{15^\circ} \right) \quad (18)$$

$$45^\circ < \phi \leq 180^\circ$$

$$f(\phi) = 1.0 + \left[-0.7145 \left(\frac{\phi - 82^\circ}{90^\circ} \right) + 0.3327 \left(\frac{\phi - 82^\circ}{90^\circ} \right)^2 \right] \left(\frac{90^\circ - \alpha_{j1}}{15^\circ} \right) \quad (19)$$

The solid lines in Figure 13 are shown for $\alpha_{j1} = 60^\circ$ and 75° . The function $f(\phi)$ is selected to correspond to a value of H/D_{je} of approximately 7 for the current study. In the form above, $f(\phi)$ contains α_{j1} as a parameter, and

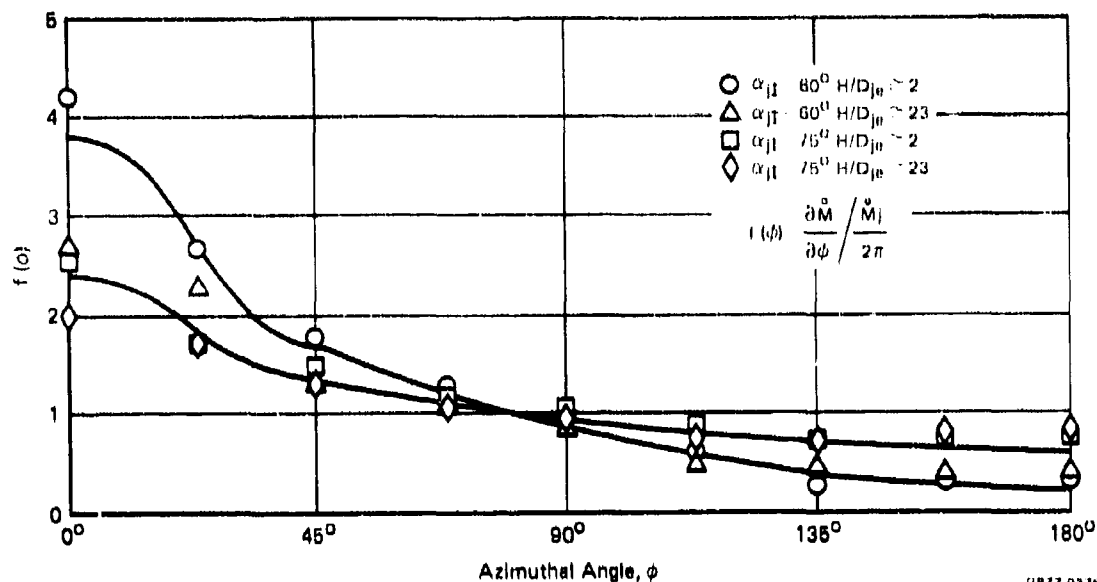


FIGURE 13
RADIAL MOMENTUM
Impinging Jet

can thus be used for any impingement angle. In this study, α_{jl} was limited to angles greater than 60° . The data of Reference 2 shows that at $\alpha_{jl} = 45^\circ$, there is essentially no momentum flow on the "backside" of the impingement region.

It should be noted that the data fit in Figure 13 demonstrates a $\cos 4\phi$ behavior near $\phi = 0$, and that the momentum level on the "frontside" ($\phi = 0$) of the impingement region is roughly six times as high as the "backside" ($\phi = 180^\circ$) for the larger impingement angles. This differs significantly from the simple $\cos \phi$ behavior assumed in Reference 11.

Equations (18) and (19) are further modified to require that the azimuthally integrated momentum flux be equal to the free-jet incident momentum flux for any jet impingement angle. This was accomplished by normalizing the area under each curve in Figure 13 by its own area. The modified ground plane wall-jet initial momentum distributions are as follows:

$$f'(\phi) = \gamma_A f(\phi) \quad (20)$$

where

$$\gamma_A = \frac{1}{1 + 0.115 \left(\frac{90^\circ - \alpha_{jl}}{15^\circ} \right)} \quad (21)$$

and $f(\phi)$ is given by Equation (18) or (19). The integrated momentum correction γ is seen to be a function of impingement angle, α_{jI} , only and becomes one for $\alpha_{jI} = 90^\circ$.

For lift-jets of exit area aspect ratio greater than 2 in close ground effect where a core flow is present at the impingement point, (see Figure 8), a $f(\phi)$ momentum flux distribution as shown schematically in Figure 14, is recommended as a function of jet impingement angle, α_{jI} . The equation for Δf shown in Figure 14 is based on a simple control volume momentum balance for two-dimensional uniform impinging jets.

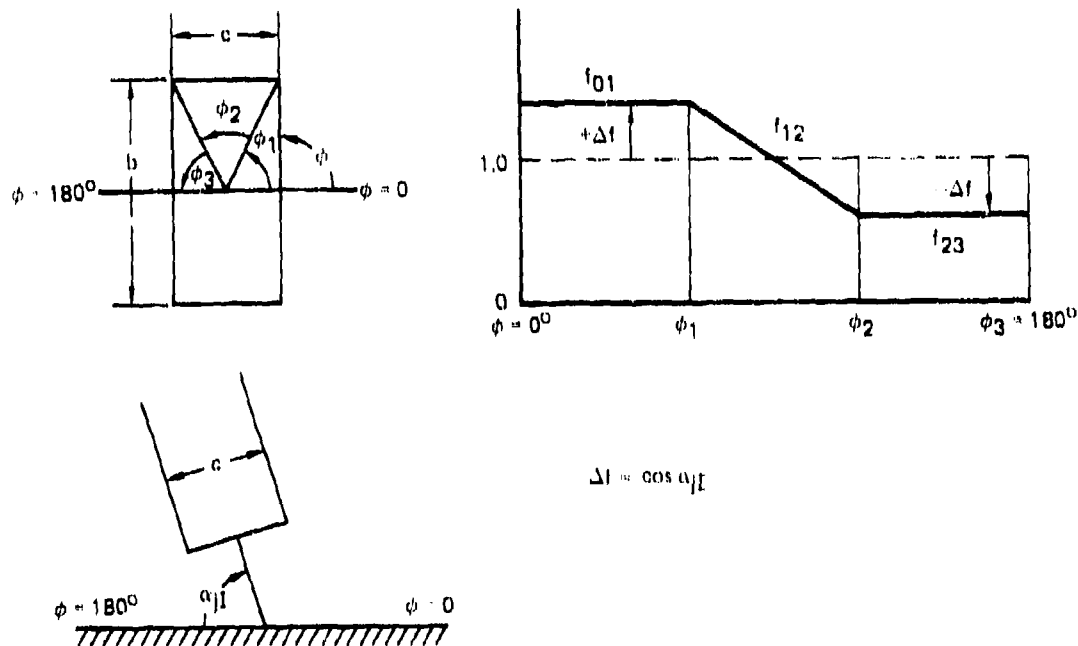


FIGURE 14
MOMENTUM FLUX DISTRIBUTION FOR RECTANGULAR NOZZLE JET ($AR > 2$)
CORE FLOW IMPINGEMENT ON GROUND PLANE

GP77 03/4 21

2.2.3 Stagnation Point Displacement - Experimental observations by Donaldson and Snedeker (Reference 2) have established the shift of the jet stagnation point from the apparent impingement point in the direction $\phi = 180^\circ$ in the ground plane. These results are presented in Figure 15 for circular jets.

2.3 Wall-Jet Flow

A description of the flow in the wall-jet region on the surface of the ground plane has been formulated through the use of the extensive data presented in Reference 2 and other sources. As would be expected, flow properties in the wall-jets are dependent on the properties of the free-jet as it

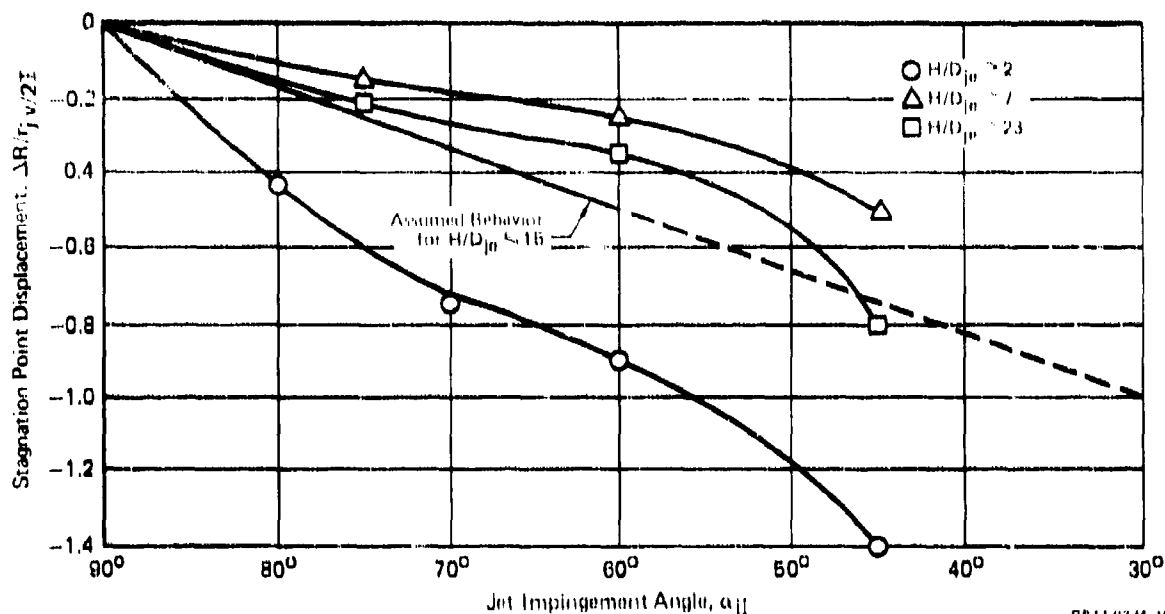
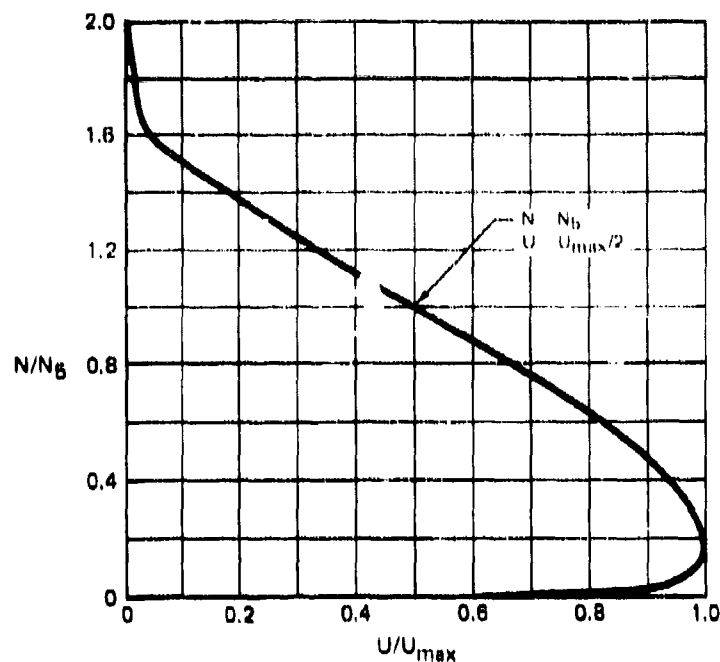


FIGURE 15
STAGNATION POINT DISPLACEMENT
Impinging Jet

enters the impingement region. Therefore, free-jet development from the jet exit to the ground plane must be established prior to definition of the wall-jet flows. This may be accomplished through use of the results presented in Section 2.1. The initial conditions for the wall-jet flows are also dependent on the local flow at the exit of the impingement region.

2.3.1 Wall-Jet Velocity and Thickness Distributions - The extensive experimental measurements described in Reference 2 have established the usefulness of the non-dimensional velocity profile shown in Figure 16 for the turbulent wall-jets. This characteristic shape persisted throughout the wall-jet region, and was found to be essentially independent of R and ϕ even for non-vertical jet impingement. With reference to Figure 12, this non-dimensional profile is assumed to describe the turbulent wall-jet for $R \geq R_1$. Study of MDRL viscous elliptic flowfield solutions for two-dimensional jets and axisymmetric jet impingement data (Reference 2) has led to the result that R_1 is about twice the outer radius, $r_{jmax,1}$, of the impinging free-jet. Therefore, from Figure 4:

$$R_1 = 2 r_{jmax,1} = 4.8 r_{jv/21} \quad (22)$$



UP77 D374 39

FIGURE 16
NON-DIMENSIONAL WALL-JET VELOCITY PROFILE

Through the use of Equation (22) and Figure 5, R_1/D_{je} may be obtained. The radial shift of the impinged jet stagnation point, ΔR_1 may be obtained from Figure 15 as a function of the ground impingement angle, α_{j1} . This is a relatively small correction.

Thus far, the geometry of the free-jet and ground radius R_1 at the beginning of the radial wall-jet have been defined. A relation for N_5 and U_{max} at $R \geq R_1$ is now required. (See Figure 12.) From MDRL turbulent flow field calculations (Reference 14) and limiting cases of the data shown in Reference 2, the following relation was established for vertical jet impingement:

$$U_{max} \left| \begin{array}{l} \alpha_{j1} = 90^\circ \\ R = R_1 \end{array} \right. = 0.55 V_{jet}. \quad (23)$$

The geometry and results of the MDRL two-dimensional turbulent flowfield computation are shown in Figures 17 and 18 (Reference 14). Experimental data from Reference 2 define the dependence of $(U_{max})_{\phi=0}$ on the jet impingement angle α_{j1} . Combination of Equation (23) with a curve fit of the appropriate data in Reference 2 yields the following result:

$$(U_{max})_{\phi=0} = [0.55 + 0.170 \left(\frac{90^\circ - \alpha_{j1}}{15^\circ} \right)] V_{jet}. \quad (24)$$

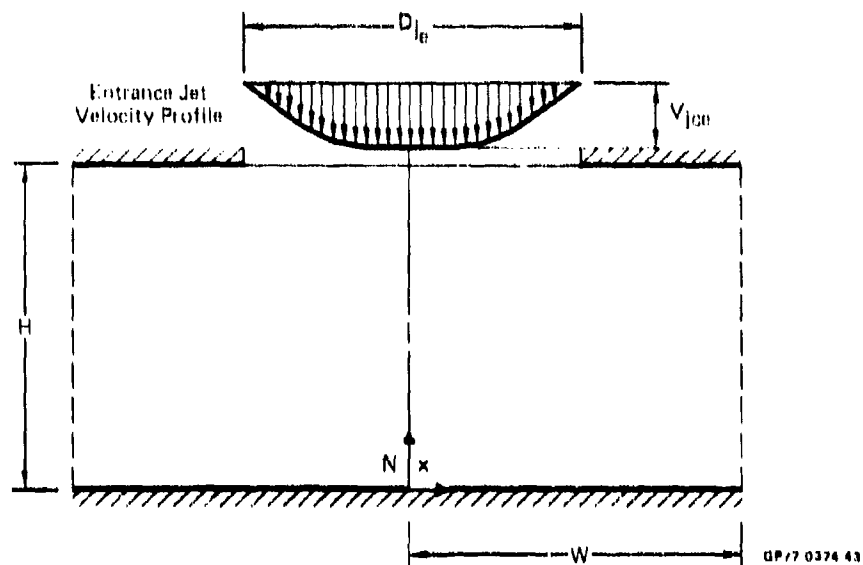


FIGURE 17
GEOMETRY OF TWO DIMENSIONAL JET IMPINGEMENT
COMPUTATION FOR TURBULENT FLOWFIELD

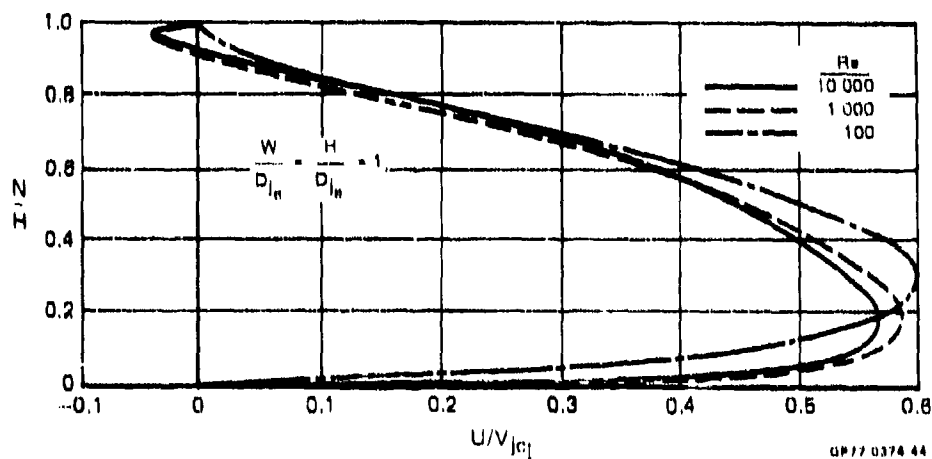


FIGURE 18
NON-DIMENSIONAL WALL JET VELOCITY PROFILE AT EDGE
OF IMPINGEMENT REGION ($X = W$)

Equation (24) relates U_{\max} at the $\phi = 0$ azimuthal position to the centerline velocity of the impinging jet and the jet impingement angle, α_{JI} . Experimental measurements in Reference 2 also define the behavior of U_{\max} with ϕ for nonvertical jet impingement:

$$\frac{U_{\max}}{(U_{\max})_{\phi=0}} = 1.0 - 0.4 \left(\frac{90^\circ - \alpha_{JI}}{15^\circ} \right) \sin \phi/2. \quad (25)$$

Combination of Equations (24) and (25) yields $U_{\max I}$ as a function of ϕ and α_{JI} :

$$U_{\max I} = V_{jet} [0.55 + .170 \left(\frac{90^\circ - \alpha_{JI}}{15^\circ} \right)] [1 - 0.4 \left(\frac{90^\circ - \alpha_{JI}}{15^\circ} \right) \sin \phi/2]. \quad (26)$$

The behavior of U_{\max} with R follows the characteristic radial decay:

$$U_{\max}(R) = \frac{R_I}{R} U_{\max I}. \quad (27)$$

The measurements of N_5 reported in Reference 2 yield required information about N_5 :

$$N_5(\phi) / (N_5)_{\phi=0} = \frac{U_{\max I}}{U_{\max I}}. \quad (28)$$

and, through interpretation of measurements of N_5 over a wide range of radial stations:

$$N_5(R) = N_{5I} + 0.07(R - R_I). \quad (29)$$

The edge of the wall-jet shear layer may be defined from Equation (29) and Figure 16 which shows that

$$N_{\max} = 2 N_5. \quad (30)$$

To complete the description of the wall-jet velocity and thickness distributions, a relationship for N_{5I} is required. This is obtained by equating the total radial wall-jet mass flux at R_I to the total mass in the free-jet at the impingement point, i.e.;

$$\int_0^{2\pi} \int_0^m \rho_{mI} U_{R_I} d\phi dN = \dot{m}_{JET}$$

This may be re-written

$$\rho_{mI} R_I N_{5I} \int_0^{2\pi} U_{\max I} \int_0^{\infty} \left(\frac{U}{U_{\max}} \right) d \left(\frac{N}{N_{5I}} \right) d\phi = \dot{m}_{JET}$$

Let the integral of the area of the velocity profile shown in Figure 16 be designated as L_m^* ,

$$\int_0^{\infty} \left(\frac{U}{U_{\max}} \right) d \left(\frac{N}{N_5} \right) = L_m^*$$

Then substituting $U_{\max I}$ from Equation (26), the following result is obtained:

$$\begin{aligned} \dot{m}_{JET} &= \rho_{mI} R_I N_{5I} L_m^* V_{JET} \times \\ &\times \int_0^{2\pi} \left[1.55 + .170 \left(\frac{90^\circ - \alpha}{15^\circ} \right) \right] \left[1 - 0.4 \left(\frac{90^\circ - \alpha}{15^\circ} \right) \ln \phi / 2 \right] d\phi. \end{aligned}$$

Performing the indicated integration and solving for N_{5I} :

$$N_{5I} = \frac{\dot{m}_{JET}}{\rho_{mI} R_I L_m^* V_{JET} \left[1.55 + .170 \left(\frac{90^\circ - \alpha}{15^\circ} \right) \right] \left[2\pi - .8 \left(\frac{90^\circ - \alpha}{15^\circ} \right) \right]} \quad (31)$$

Therefore, N_{5I} is related to the properties of the free-jet through \dot{m}_{JET} and V_{JET} and to the impingement angle α_{JI} .

Equations (22) through (31) describe the geometry and velocity distribution in the wall-jet region. Although the thickness of the wall-jet region is not a function of ϕ , the velocity is influenced by ϕ (Equation (26)) and therefore, the mass flow rate in the wall-jet will vary with ϕ for non-vertical jet impingement as did the momentum flux. The mass flow rate will also increase with R as the wall-jet entrains ambient fluid. This will be discussed further in Section 2.3.2.

Verification of ground plane wall-jet flow prediction results have been obtained. Figure 19 shows measured values of maximum wall-jet velocity, U_{\max} at the impingement region outer radius, R_I , as computed from Equations (7) and (8). The agreement is seen to be very good. This is significant since the values of U_{\max} and R_I are needed for computation of wall-jet entrainment velocities.

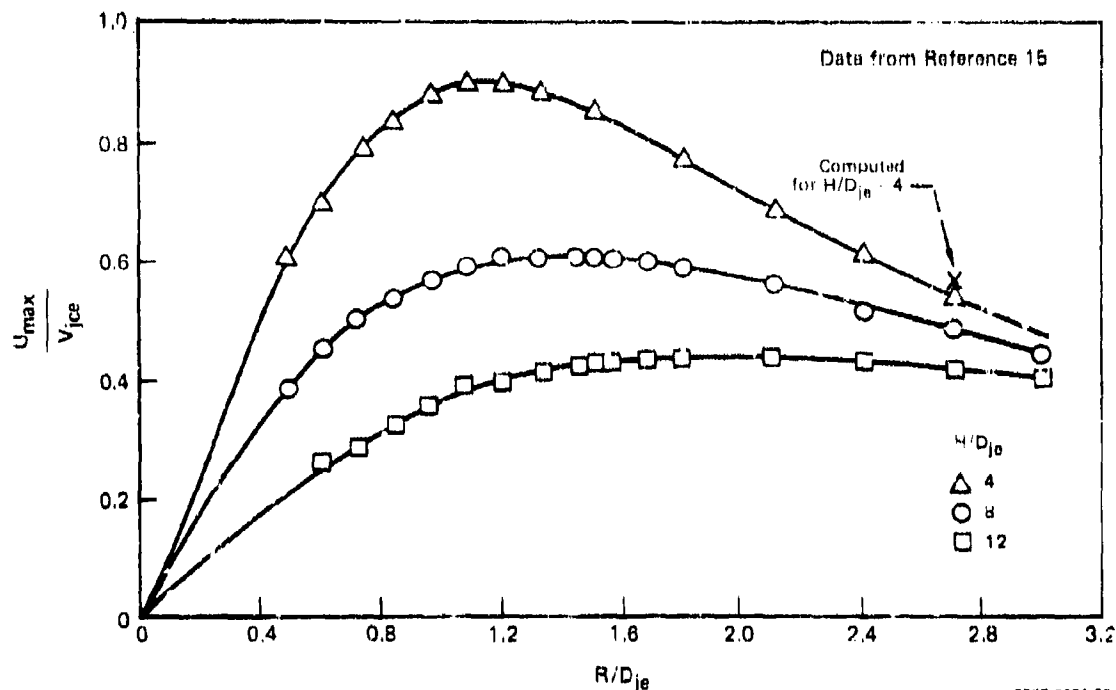


FIGURE 19
VARIATION OF MAXIMUM RADIAL VELOCITY WITH RADIAL DISTANCE -
VERTICAL JET IMPINGEMENT

2.3.2 Wall-Jet Entrainment - Wall-jet entrainment rates can be obtained through use of the results presented in Section 2.3.1 for wall-jet geometry and velocity distributions. The radial wall-jet is a diverging area flow, and since the entire flow occurs in a constant static pressure environment, severe thinning of the jet would occur without the thickening effect of mass entrainment. Equation (29) expresses the growth of the wall-jet thickness with radius, R , with initial value N_{5I} at R_I .

The total mass flow in the free-jet can be computed from empirical data on mass entrainment including density differences between the jet and the ambient density. At the impingement point, a mean jet density can be computed. Let this mean density at the impingement point be designed as ρ_{m1} . This density is used to determine N_{5I} in Equation (31). The total mass flow in the radial wall-jet in an azimuthal sector between the angles ϕ_B and ϕ_A is the following:

$$\dot{m}[(\phi_B - \phi_A), R] = \rho_m \int_{\phi_A}^{\phi_B} \int_0^m U_{max} \left(\frac{U}{U_{max}} \right) R N_5 \left(\frac{dN}{N_5} \right) d\phi$$

using the definition of I_m^* and Equation (27) for the variation of U_{\max} with R , this becomes:

$$\frac{\dot{m}}{\rho_m} [(\phi_B - \phi_A), R] = N_5 I_m^* R_I \int_{\phi_A}^{\phi_B} U_{\max I} d\phi. \quad (32)$$

Now using Equations (29) and (26) for $N_5(R)$ and $U_{\max I}(\phi)$ respectively:

$$\frac{\dot{m}}{\rho_m} [(\phi_B - \phi_A), R] = R_I I_m^* V_{jet} \left[N_{5I} + .07 (R - R_I) \right] \int_{\phi_A}^{\phi_B} \left[1 - 0.4 \left(\frac{90^\circ - \alpha}{15^\circ} \right) \sin \frac{\phi}{2} \right] d\phi. \quad (33)$$

The entrained mass between successive radii R_B, R_A may be expressed as follows:

$$\frac{\dot{m}}{\rho_m} [(\phi_B - \phi_A), R_B] - \frac{\dot{m}}{\rho_m} [(\phi_B - \phi_A), R_A] = \frac{\dot{m}_{\text{entrained}}}{\rho_{\text{ambient}}}. \quad (34)$$

Through the use of Equations (33) and (34), and a successive set of computations along the radius R , the mass flow, entrained mass flow, and mean density of the wall-jet may be determined.

The last term in Equation (34) represents the volume flow rate of entrained flow per unit area of the wall-jet surface. Taking this surface to be approximately parallel to the ground plane (actually it is inclined at an angle of approximately 4°),

$$A_{\text{surface}} = \int_{R_A}^{R_B} \int_{\phi_A}^{\phi_B} R dR d\phi = \frac{R_B^2 - R_A^2}{2} (\phi_B - \phi_A) \quad (35)$$

From Equation (34)

$$\frac{\dot{m}_{\text{entrained}}}{\rho_{\text{ambient}}} = V_N A_{\text{surface}}. \quad (36)$$

Combining Equations (33), (35) and (36) the following expression for V_N is obtained:

$$V_N = \frac{0.14 R_I V_{jet} I_m^* \left[0.55 + .170 \left(\frac{90^\circ - \alpha}{15^\circ} \right) \right] \int_{\phi_A}^{\phi_B} \left[1 - .4 \left(\frac{90^\circ - \alpha}{15^\circ} \right) \sin \frac{\phi}{2} \right] d\phi}{(R_B + R_A) (\phi_B - \phi_A)} \quad (37)$$

For the special case of vertical jet impingement, $\alpha_{JI} = 90^\circ$, Equation (37) becomes

$$V_N = \frac{0.14 R_I V_{JCI} \Gamma_m^* 0.55}{(R_B + R_A)}$$

The numerical value of Γ_m^* is approximately 0.98. Therefore:

$$V_N = .075 V_{JCI} \frac{R_I}{(R_B + R_A)} \quad (38)$$

$\alpha_{JI} = 90^\circ$

2.3.3 Radial Wall-Jet Momentum - The azimuthal distribution of radial wall-jet momentum is obtained at the exit of the impingement region from the results presented in Section 2.2.2. Figure 20 shows the radial dependence of the impinged jet radial momentum, also from Reference 2. These data clearly show that wall shear stress can be neglected in the radial development of the wall-jets since the radial momentum is clearly conserved through a large range of R/D_{ju} . This greatly simplifies the modeling of the wall-jet development region, since the $F(\phi)$ momentum functions will establish the azimuthal momen-

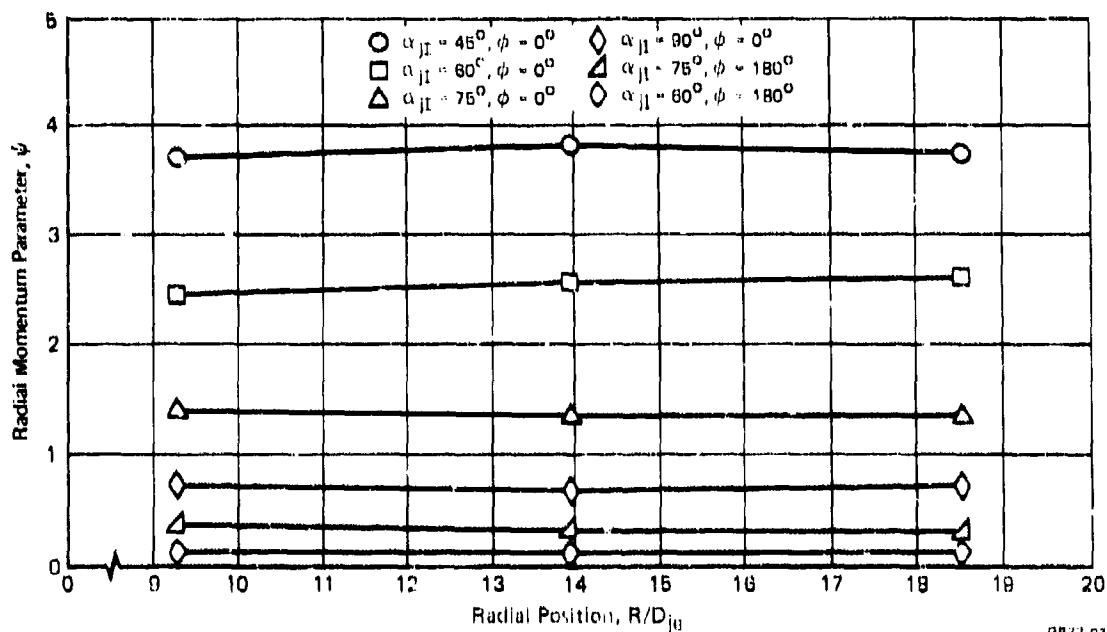


FIGURE 20
RADIAL MOMENTUM R DEPENDANCE

tum distributions for all values of radius, R, up to any wall-jet interaction radius. It should be noted that the data of Figure 20 include impingement angles as low as 45° where there is essentially no momentum flux on the "back-side" of the impingement region ($\phi = 180^\circ$). Mathematically expressed, the data of Figure 20 indicate that

$$\frac{\partial}{\partial R} \left(\frac{\partial \dot{M}/\dot{M}_1}{\partial \phi} \right) = 0 \quad . \quad (39)$$

In contrast, Equation (3-10) of Reference 11 may be differentiated with respect to R to yield

$$\frac{\partial}{\partial R} \left(\frac{\partial \dot{M}/\dot{M}_1}{\partial \phi} \right) = - \frac{1}{2\pi} \frac{\Delta h \cos \phi}{h_r R^2} \quad , \quad (40)$$

indicating dependence on R. This is not a radial decay because of ground wall shear, but is a result of the geometric modeling of the jet impingement region used in Reference 11. This is apparent, since in the modeling of Reference 11, when normal jet impingement occurs, $\Delta h = 0$, in which case Equation (40) would indicate a radial decay of momentum for oblique impingement only. Additionally, the data of Reference 2 indicate that the height of the wall-jet does not vary significantly with azimuthal angle for oblique impingement (Equation (28)).

The simplification of the wall-jet stagnation line computations and the supply of momentum to the bases of fountains that follows from the use of results based on Equation (39) as opposed to Equation (40) will be discussed in Section 3.0.

3. VISCOUS FLOWFIELD WITHIN THE INNER REGION

As discussed in Section 2, the accuracy of description and modeling of the viscous flow in the region between the undersurface of the aircraft and the ground plane has been greatly enhanced by the extensive experimental study of jet impingement by Donaldson and Snedeker, Reference 2. These and other data have been employed to define the properties of the free-jet and wall-jet formed by the flow from any individual lift-jet nozzle. Analysis of a multi-jet VTOL aircraft lift system flowfield requires a complete description of the geometry of the aircraft including individual nozzle vector and splay angles, aircraft height and orientation (pitch, roll) with respect to the ground plane, individual lift-jet trajectories, and jet impingement points and jet impingement angles on the ground plane. These geometric data are required for each jet to enable the application of the fluid flow modeling techniques presented in Section 2.0. After the fluid flow properties of each individual wall-jet are established, the wall-jet interaction stagnation lines are determined from the procedures to be described in Sections 3.2 for any two-jet pair and in Section 3.3 for a 3 or 4 jet VTOL aircraft multi-jet lift system. The final result of the stagnation line computation procedure provides information on stagnation line locations in the ground plane, initial fountain flow directions, and momentum flux entering the bases of fountains located above the stagnation lines.

These procedures have been developed for the flowfield within the inner region between the aircraft under-surface and the ground plane. The inner region is bounded on the sides by geometric planes normal to the ground plane and passing through lines connecting each pair of jet impingement points on the ground. The procedures developed, however, can be easily extended to ground plane flow regions outside of the inner region where fountain impingement on aircraft undersurfaces can also occur and produce loads on the airframe.

3.1 Airframe, Jet, and Ground Plane Geometry

The initial airframe geometry, aircraft orientation, and height above ground must, of course, be specified or known by the user to implement the prediction methodology. A three view drawing of the aircraft including nozzle geometry and nozzle center of rotation or vectoring levure locations and aircraft center of gravity location is helpful for this purpose. It is important that a consistent right handed system of coordinates be used in the airframe such as the conventional Fuselage Station (x), Butt Line (y), Water Line (z) system.

A mathematical procedure has been developed to determine the intersection points of the free-jet centerlines with the ground plane, for an arbitrarily oriented aircraft, including the effects of individual jet deflection. This procedure includes the effects of cross-flow on the free-jet path deflection and the corresponding impingement points. The mathematical formulation of this procedure is described in Appendices I and II. A computer program has been written to carry out the calculations, and has been checked out for several cases. The required geometric inputs to the program are:

1. Aircraft reference c.g. location - Fuselage Station (F.S.), Butt Line (B.L.) and Water Line (W.L.)
2. Number of jets (a maximum of four)
3. Coordinates (F.S., B.L., W.L.) for the center of thrust of each nozzle
4. Vectoring angle, splay angle, jet velocity, and jet diameter for each nozzle
5. Aircraft pitch, roll, and yaw angles; height of the reference c.g. above ground; and freestream velocity.

The program outputs the center of thrust coordinates, thrust vector components, jet impingement points, and jet impingement angle complements, α , referenced to a ground-fixed coordinate system whose origin lies directly below the aircraft c.g., and whose x-axis is aligned with the cross-flow velocity vector. The jet impingement angle complements are defined by the vector tangent to each jet path at its point of intersection with the ground, and the normal vector to the ground plane. The absolute angle in the ground plane (0° to 360°) of the intersection with the ground plane of a plane normal to the ground plane and containing the tangent to the jet path at its intersection with the ground is also output. This angle, γ , defines the negative of the direction in the ground plane of the projection of the horizontal component of jet velocity in the ground plane. This in turn defines the $\phi = 180^\circ$ direction for each jet impingement region in the ground plane coordinate system.

At the impingement points in the ground plane, a basic polar coordinate system is used to define the properties of the wall-jets about each impingement point as shown in Figure 12. This is the local R, ϕ system of coordinates which apply to each radial wall-jet.

3.2 Stagnation Line Computation for a Pair of Wall-Jets

The computation of the stagnation line position between a pair of interacting wall-jets is accomplished through the application of a control-volume momentum balance along a differential segment of the stagnation line. Momentum

fluxes entering the control volume are related to the impingement region exit momentum distributions for each jet as shown in Figure 13 and the angular sector emanating from each jet impingement point that is subtended by the differential stagnation line segment. The result is an equation for the slope of the stagnation line at any point in the ground wall-jet flowfield. The stagnation line is determined by a stepwise marching process using these computed slopes. A similar development for the slope of the stagnation line between one arbitrary wall-jet and a uniform ground cross-flow has been accomplished.

3.2.1 Development of the Stagnation Line Slope Equations - The momentum balance for the determination of the local stagnation line slope is applied to the elemental control volume in the ground plane as shown in Figure 21. The conservation of momentum normal to the stagnation line for the control volume in the absence of any pressure and viscous forces is the following:

$$\iint_{C.S.} \vec{U}_{N\ell} (\rho \vec{U} \cdot d\vec{A}) = 0 \quad (41)$$

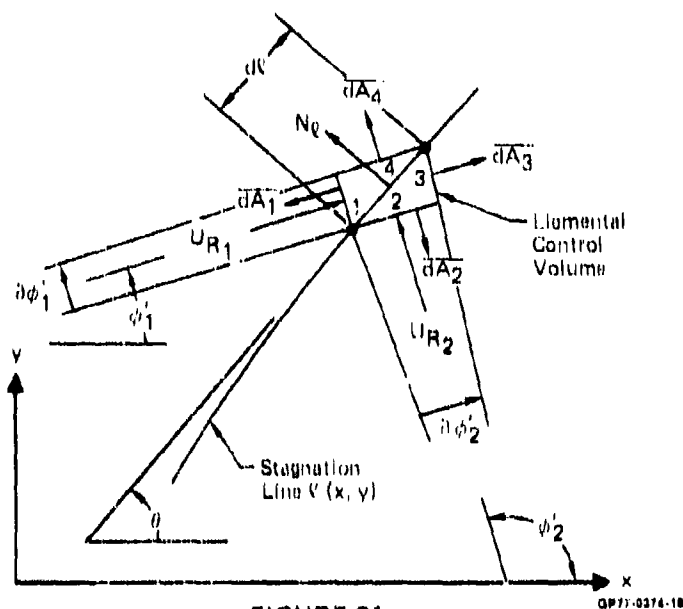


FIGURE 21
CONTROL VOLUME AND GEOMETRY FOR STAGNATION LINE
MOMENTUM BALANCE

Sides 1 and 2 of the control volume are chosen normal to the radial velocity vectors, \vec{U}_{R1} and \vec{U}_{R2} , from the individual jet impingement points. Assuming no loss in wall-jet radial momentum with geometric local radius R

for each wall-jet based on the experimental results shown in Figure 20 (or as expressed by Equation (39)), the momentum flux for each circumferential sector is :

$$\int_0^{\infty} \rho U_R^2 R \partial \phi' dN = \gamma_A f(\phi) \dot{M}_j \frac{\partial \phi'}{2\pi} \quad (42)$$

where N is the distance normal to the ground plane. Applying Equation (41) to the control volume (Figure 21), and using the fact that no flow occurs through control volume sides 3 and 4, the following result is obtained :

$$\begin{aligned} & \int_0^{\infty} \rho U_{R1}^2 R_1 \sin(\theta - \phi_1') \partial \phi_1' dN \\ & = \int_0^{\infty} \rho U_{R2}^2 R_2 \sin(\phi_2' - \theta) \partial \phi_2' dN \end{aligned} \quad (43)$$

where the angles are further defined in Figure 22.

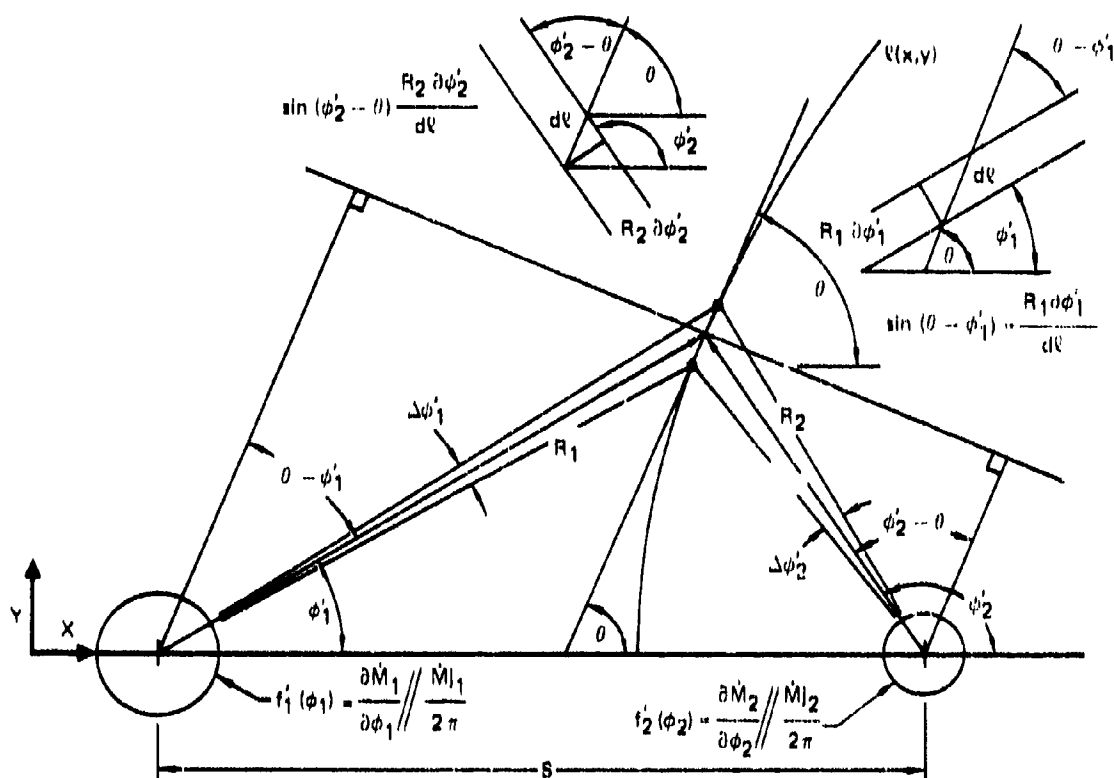


FIGURE 22
WALL-JET INTERACTION GEOMETRY

GPFF 0324 0/1

Substituting Equation (42) into the above result, the following is obtained:

$$\gamma_{A1} f_1(\phi_1) \dot{M}_{j1} \sin(\theta - \phi_1') \partial \phi_1' = \gamma_{A2} f_2(\phi_2) \dot{M}_{j2} \sin(\phi_2' - \theta) \partial \phi_2'. \quad (44)$$

From the geometry shown in Figure 22, the following is obtained:

$$\partial \phi_1' = \frac{dv \sin(\theta - \phi_1')}{R_1} \quad (45a)$$

and

$$\partial \phi_2' = \frac{dz \sin(\phi_2' - \theta)}{R_2} \quad (45b)$$

Substituting equations (45a and b) into Equation (44) there results:

$$\frac{\gamma_{A1} f_1(\phi_1) \dot{M}_{j1} \sin^2(\theta - \phi_1')}{R_1} = \frac{\gamma_{A2} f_2(\phi_2) \dot{M}_{j2} \sin^2(\phi_2' - \theta)}{R_2} \quad (46)$$

Solving Equation (46), the following desired result is obtained after some further geometric substitutions are made from the geometry in Figure 22:

$$\tan \theta = \frac{dy}{dx} \left| x = \frac{\beta \sin \phi_2'}{1 + \beta \cos \phi_2'} \right. \quad (47)$$

where

$$\beta = \frac{R_1}{S} \sqrt{\frac{\gamma_{A2} f_2(\phi_2) / \gamma_{A1} f_1(\phi_1) \dot{M}_{j2} / \dot{M}_{j1}}{R_2 / R_1}} + \frac{R_2}{S} \quad (48)$$

The distinction made in the above equations between the angles ϕ and ϕ' is necessitated by the fact that the $\phi' = 0$ direction is parallel to a line joining the jet impingement points, whereas $\phi = 0$ is related to the individual jet impingement geometries. ϕ' and ϕ are related by a simple rotation about the impingement point of the type of data shown in Figure 13.

The stagnation line solution for any jet pair is obtained by a stepwise marching process beginning at the point where the stagnation line crosses the line joining the jet impingement points. At this common point, the radii R_1 and R_2 as shown in Figure 22 are related as follows:

$$\frac{R_2}{R_1} = \frac{\dot{M}_{J2} \gamma_{A2} f_2(\phi_2)}{\dot{M}_{J1} \gamma_{A1} f_1(\phi_1)} \quad (49)$$

This may be obtained from Equation (46) by setting $\phi_1' = 0$ and $\phi_2' = \pi$ in that equation. For normal jet impingement, Equation (49) simplifies to

$$\frac{R_2}{R_1} = \frac{\dot{M}_{J2}}{\dot{M}_{J1}} \quad (50)$$

A computational program has been written to determine the coordinate of the stagnation lines as determined through the solutions of Equations (47), (48) and (49). The mechanics of this procedure and the implementation of the process for multi-jet flowfields is discussed further in Section 3.3.

3.2.2 Wall-Jet Pair Stagnation Line Solutions - Stagnation line solutions obtained through solution of Equations (47), (48) and (49) are presented in Figures 23 through 25. Figure 23 shows the results of a parametric variation of the interaction of wall-jets formed by two vertical jets of various momentum ratios. Shown also in Figure 23 are stagnation line solutions for non-vertical but equal jet impingement angles of 75 and 60° for jets of equal momentum. Note that the results shown in Figure 23 are shown for the upper right hand quadrant only, and that the ordinate scale is compressed by a factor of two.

The stagnation line patterns for multi-jet interactions may be obtained from results such as shown in Figure 23 by appropriate location, rotation, and application of logical rules of symmetry to individual jet pair stagnation line solutions. For example, a family of stagnation line solutions for a four jet arrangement is shown in Figure 24. These were constructed from curves selected from Figure 23. Likewise, Figure 25 presents a wall-jet interaction stagnation line solution for a three jet arrangement with the two aft jets each having one half the jet momentum of the forward jet (all jets are impinging vertically).

Figure 26 shows a comparison of computed and measured stagnation line locations for a two-jet pair. The experimental data were obtained as part of a McDonnell Aircraft Company Propulsion Department Independent Research and development program (IRAD).

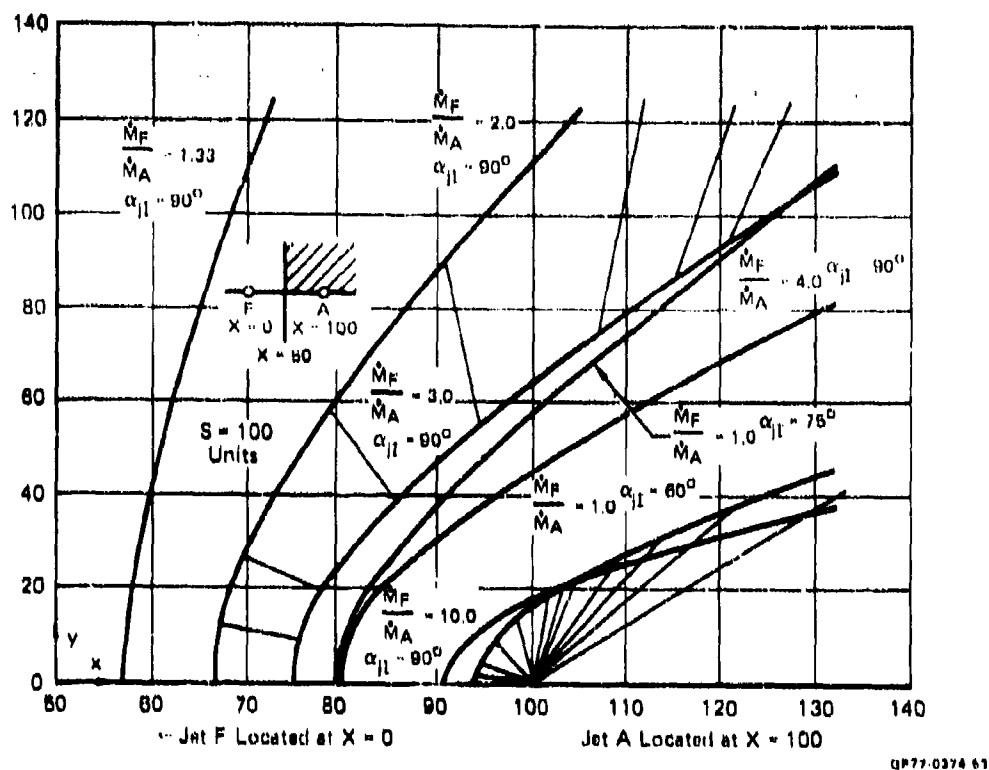


FIGURE 23
COMPUTED JET PAIR STAGNATION LINES IN UPPER RIGHT QUADRANT

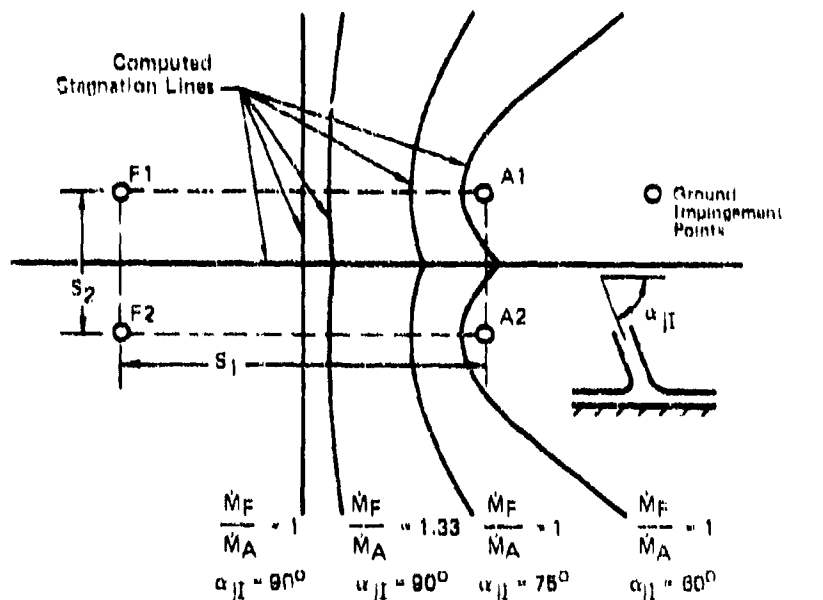


FIGURE 24
COMPUTED STAGNATION LINES FOR 4-JET ARRANGEMENT

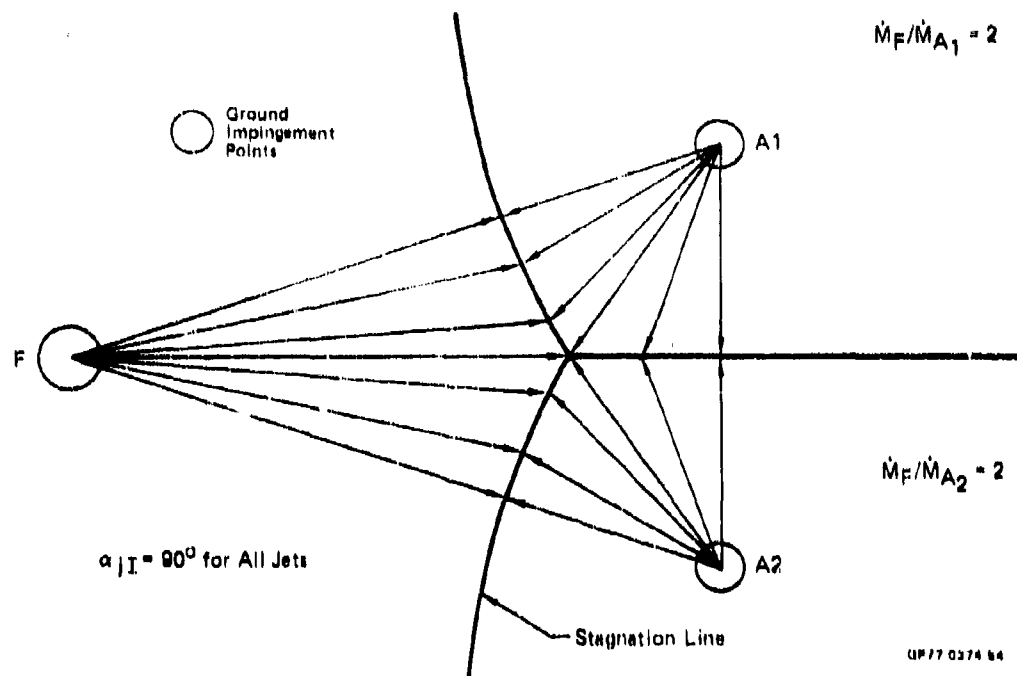


FIGURE 25
STAGNATION LINES FOR 3-JET ARRANGEMENT

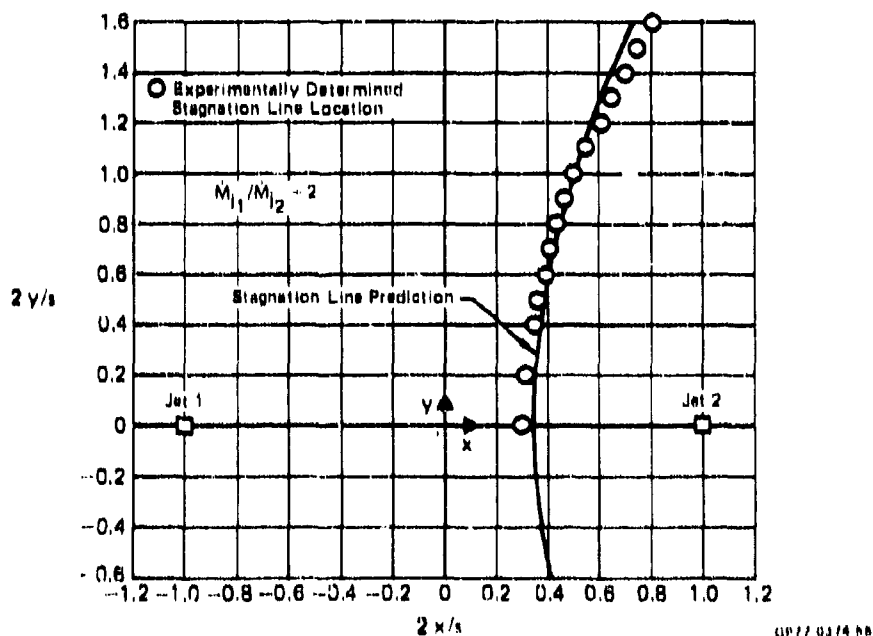


FIGURE 26
COMPARISON OF MEASURED AND PREDICTED WALL-JET STAGNATION LINES

3.2.3 Local Direction of Fountain Flow Above Stagnation Line - An estimate of local fountain flow direction directly above each point on the stagnation line may be obtained through further assumption of conservation of momentum without viscous losses in the turning region at each point on the stagnation line. Consider the stagnation line geometry and momentum flux decomposition shown in Figure 27. The local fountain flow plane shown in Figure 27 is assumed to be perpendicular to the ground plane. Here the momentum flux incident on a stagnation line segment from wall-jet number 2, \dot{M}_{R2} , is resolved into components normal to and tangent to the stagnation line segment. If it is assumed that the vertical momentum flux in the fountain from wall-jet 2, \dot{M}_{FN2} , is equal in magnitude to \dot{M}_{N2} and that the tangential component of momentum flux in the fountain from wall-jet 2, \dot{M}_{FT2} , is equal in magnitude to \dot{M}_{T2} , the angle κ_2 is defined as shown in Figure 27 and may be found to be geometrically equal to $\phi_2' - \theta$.

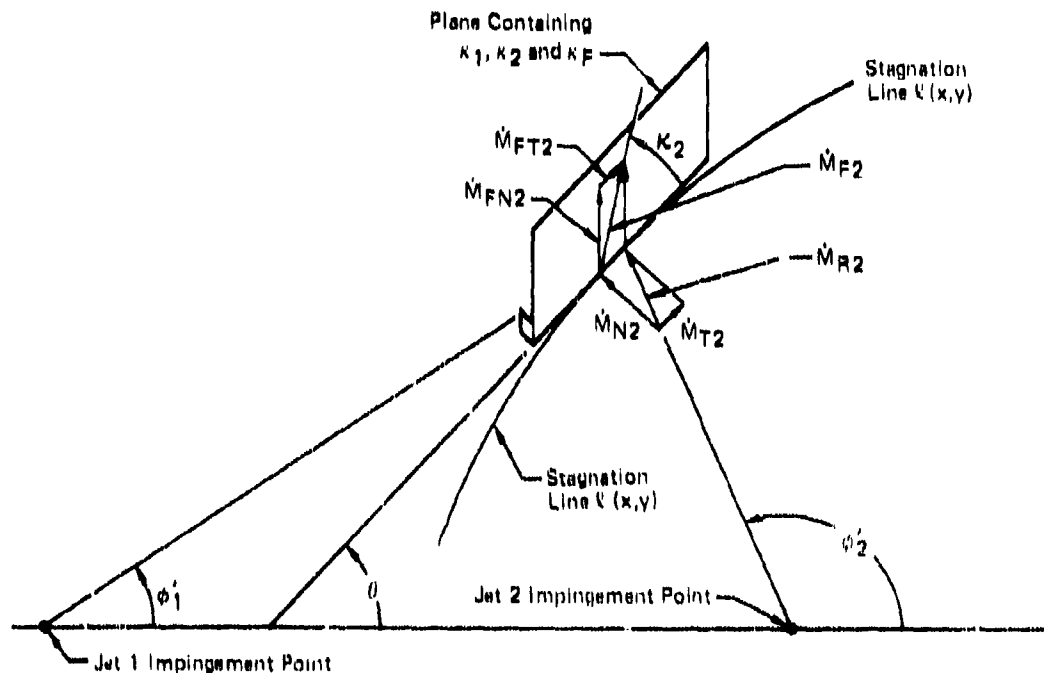


FIGURE 27
RADIAL WALL-JET AND FOUNTAIN MOMENTUM RELATIONSHIP

GP77 0274 22

$$\kappa_2 = \phi_2' = \theta \quad (51)$$

and, likewise for the flow from wall-jet 1,

$$\kappa_1 = \theta - \phi_1' \quad (52)$$

For the two sides of the fountain:

$$\dot{M}_{FNTOT} = \dot{M}_{FN1} + \dot{M}_{FN2} = 2 \dot{M}_{FN} \quad (53)$$

and

$$\dot{M}_{FTTOT} = \dot{M}_{FT1} + \dot{M}_{FT2} \quad (54)$$

The angle κ_F is defined for the fountain as

$$\tan \kappa_F = \frac{\dot{M}_{FNTOT}}{\dot{M}_{FTTOT}} \quad (55)$$

Through substitution of Equations (53) and (54) into Equation (55) there results:

$$\tan \kappa_F = \frac{2 \dot{M}_{FN}}{\dot{M}_{FT1} + \dot{M}_{FT2}} \quad (56)$$

dividing through by \dot{M}_{FN} ,

$$\tan \kappa_F = \frac{2}{\frac{\dot{M}_{FT1}}{\dot{M}_{FN}} + \frac{\dot{M}_{FT2}}{\dot{M}_{FN}}} \quad (57)$$

now, using the angles κ_1 and κ_2 , the above becomes:

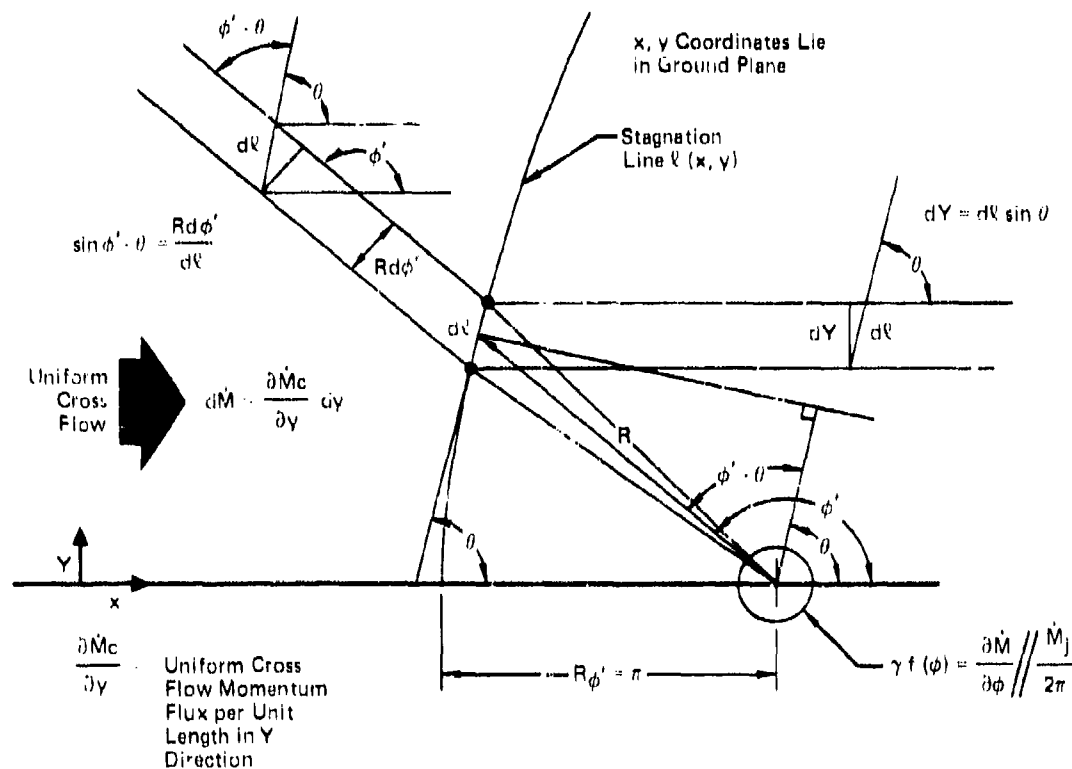
$$\tan \kappa_F = \frac{2}{\cot \kappa_1 + \cot \kappa_2} \quad (58)$$

Based on the assumption of a constant convective velocity in the turning process between the wall-jets and each side of the fountain, resulting in a mixed and averaged convective velocity within the fountain itself, the angle κ_F in Equation (55) is assumed to represent the fountain velocity component ratio as well as the momentum component ratio. Therefore:

$$\tan \kappa_F = \frac{V_{FN}}{V_{FT}} \cdot \frac{\dot{M}_{FNTOT}}{\dot{M}_{FTTOT}} = \frac{2}{\cot \kappa_1 + \cot \kappa_2} \quad (59)$$

The local slope of the stagnation line in the ground plane, θ , and the angle κ_F then determine the local direction of the upward flow in the fountain above each point on the stagnation line as shown in Figure 27.

3.2.4 Stagnation Line Slope Equation for Single Wall-Jet and Uniform Cross-Flow Interaction - The theoretical development presented in Section 3.2.1 has been modified for the determination of the local slope of the stagnation line in the region of interaction of a single wall-jet and a uniform cross-flow. A diagram presenting the geometry of this interaction in the ground plane and the necessary nomenclature is presented in Figure 28.



GP77-0374-82

FIGURE 28
INTERACTION GEOMETRY - RADIAL WALL-JET AND UNIFORM CROSS-FLOW

A control volume enclosing the differential line segment, dL , is used to apply the laws of conservation of momentum in a direction perpendicular to the line segment in the ground (x, y) plane. As in the case of two radial wall-jets, the resulting expression is an equation for the slope of the line

segment, $d\ell$, in the x, y , plane. The momentum distribution in the radial wall-jet is defined identically as it was for the two wall-jet interaction case. The new physical quantity required is the momentum flux per unit length (in the y direction) of the cross-flow.

Along the x axis in Figure 28, where the axis is chosen parallel to the cross-flow direction, the penetration of the radial wall-jet into the cross-flow is given by the magnitude of the wall-jet radius $R_{\phi = \pi}$.

$$R_{\phi = \pi} = \frac{\gamma_A f(\phi = \pi) \dot{M}_j}{2\pi \frac{\partial \dot{M}_c}{\partial Y}} \quad (60)$$

which for a vertically impinging jet becomes

$$R_{\phi = \pi} = \pi = \frac{\dot{M}_j}{2\pi \frac{\partial \dot{M}_c}{\partial Y}} \quad (61)$$

Through the use of Equation (60) or (61), the location of the stagnation line as it crosses the " x " axis may be found. The general equation for the slope of the stagnation line is the following:

$$\tan \theta = \frac{\omega \sin \phi}{1 + \omega \cos \phi} \quad (62)$$

where

$$\omega = \sqrt{\frac{\gamma_A f(\phi) \dot{M}_j}{2\pi R \frac{\partial \dot{M}_c}{\partial Y}}} \quad (63)$$

These equations have the same general form as the corresponding equations for a pair of intersecting radial wall-jets. The solution of the equation follows the same procedure as for the intersecting wall-jets which has been described previously.

The practical difficulty in the application of the above results to cross-flow/radial wall-jet interactions is the determination of the quantity $\partial \dot{M}_c / \partial Y$. The difficulty lies in determination of how much momentum in the vertical direction (normal to the ground plane) should be included in the momentum derivative. Mathematically:

$$\frac{\partial \dot{M}_c}{\partial Y} = \int_0^N \rho U_x^2 dN \quad (64)$$

It is recommended that until pertinent empirical verification data are obtained, N be taken to be equal to the value of N_{\max} computed for the radial wall-jet flow (Equation (30)). Because of the uncertainty involved in definition of the cross-flow momentum magnitude, the stagnation line solution for the wall-jet/cross-flow interaction has not been included in the ground flow-field computer program.

3.3 Computation of Stagnation Lines for Three-or Four Jet Flowfields

The computation of wall-jet stagnation lines in the ground flowfield below a multi-jet VTOL aircraft is accomplished from the results of computations between pairs of interacting wall-jets. The fountains formed above the stagnation lines are assumed to convect the interacting flows upward and away from the ground surface therefore preventing the mutual interaction of any more than two wall-jets on any stagnation line. At points in the flow-field where two or more stagnation lines intersect, the fountain flows from more than one jet pair will interact forming what has been called a central fountain. However, this interaction takes place above the ground plane and occurs only at a "point" in the ground plane surface. The fountains formed above the stagnation lines are three dimensional unless the ground stagnation line is a straight line. If the ground stagnation line is straight, the fountain velocity vectors lie in a common plane, but are diverging in nature forming a "fan". Fountain flows will be discussed in detail in Section 5 and 6 of this report.

3.3.1 Geometry for Three or Four Jet Stagnation Line Computation - For the three or four jet case, the results of Section 3.2.1 are applied to each wall-jet pair. The ground plane geometry required is defined in Figure 29. Here the ground plane reference coordinate system is designated as XOP, YOP where the XOP axis is aligned with the direction of the free-stream or cross-wind velocity direction. The location of the impingement points XOPN, YOPN where N is the jet number are obtained directly from the results described in Section 3.1 and Appendices I and II. A straight line is then constructed between each pair of impingement points forming a triangular or quadrilateral as shown in Figure 29. The angles, ω_N , of each line joining the pairs of impingement points are then determined. The angles, ω_N , must be determined in the absolute sense from 0 to 360° with $\omega = 0^\circ$ taken conventionally along the +XOP axis and $+\omega$ measured counter-clockwise from that reference position. The sense of each straight line joining the jet impingement point pairs is taken in the order of the numbering of the jet impingement points. For example, the line joining impingement points 1 and 2 in Figure 29 has associated with it an ω_1 direction of slightly more than 90°, and likewise the value of ω_4 is slightly less than 360°.

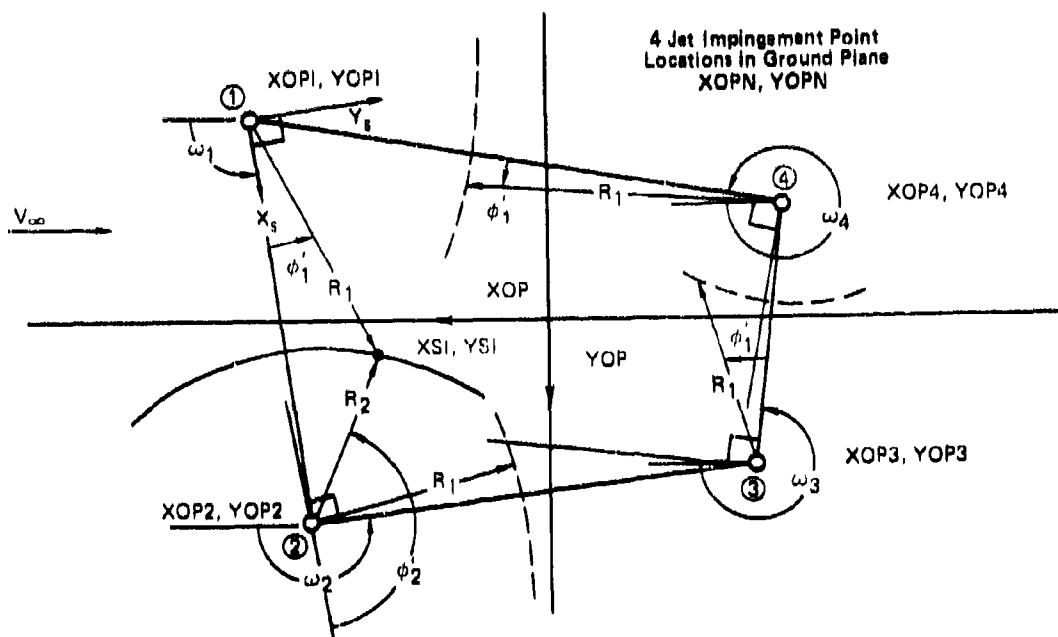


FIGURE 29
COMPUTATION OF STAGNATION LINES

GP77-6374-18

The individual stagnation line solutions are then computed for each wall-jet pair in the double-polar coordinate system shown in Figure 22. The results of these computations, which determine the coordinates of the stagnation lines in the local polar systems, are then transformed to the XOP, YOP ground plane reference system through the use of the angles ω_N ; the local polar coordinates R, ϕ' ; and the jet impingement point coordinates, XOPN, YOPN. Each stagnation line is computed in the positive sense of ϕ_1' , thereby determining the portion of the stagnation line in the inner region. Stagnation lines of "symmetry" (perpendicular bisectors of the line joining the jet impingement point pairs) must be determined separately since, in this case, $\tan \theta = \infty$, and Equation (47) is singular since the denominator on the right hand side of the equation becomes zero.

3.3.2 Rotation of Basic Momentum Distribution, $f(\phi)$ - In the computation of the wall-jet pair stagnation line solutions, the local polar coordinate system R, ϕ' will not always result in an orientation such that $\phi' = 0$ in the direction $\phi = 0$ as defined for each jet impingement point. In these cases, the angular rotation of the momentum distribution $f(\phi)$ as shown in Figure 30, must be utilized. In Figure 30, the angle, γ , described in Section 3.1 establishes the projection of the direction of the negative of jet mean

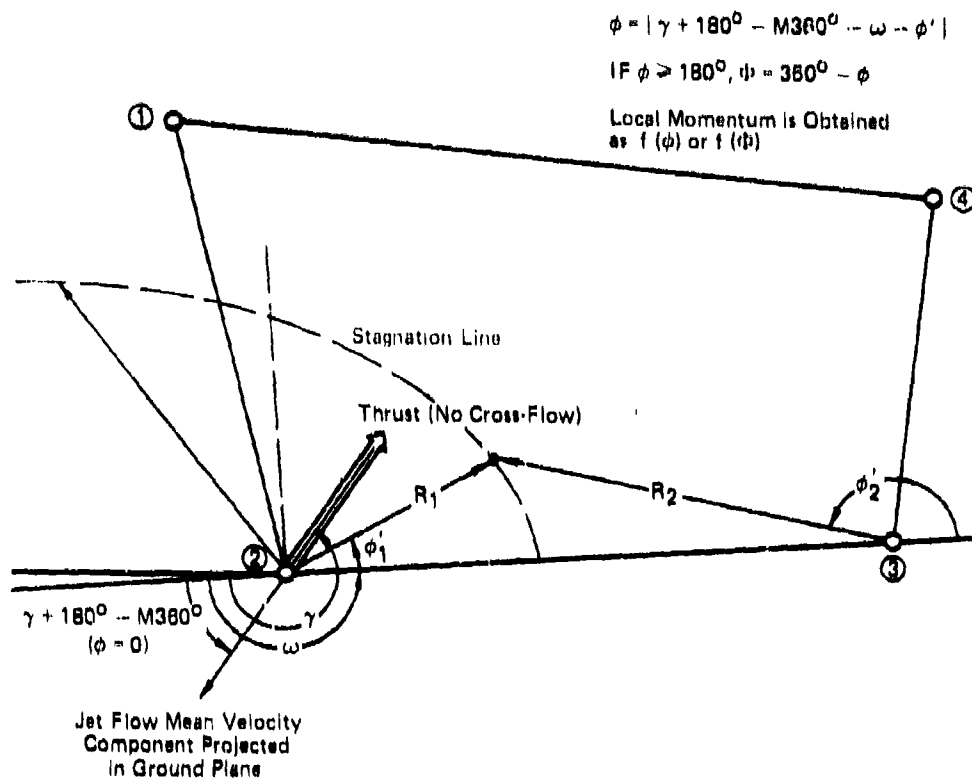


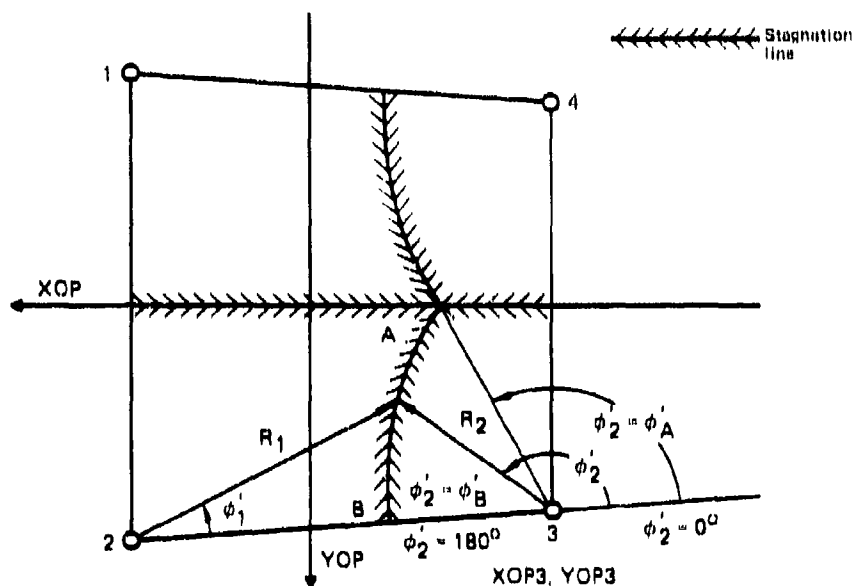
FIGURE 30
ROTATION OF MOMENTUM DISTRIBUTION $f(\phi)$

velocity in the ground plane. This corresponds to the projection of the thrust vector in the ground plane if there is no cross-flow. The negative γ direction then corresponds to the direction in which $\phi = 0$. The ϕ used to determine the momentum flux distribution $f(\phi)$ from Figure 13 is then given by the following (from Figure 30):

$$\phi = | + 180^\circ - M 360^\circ - \omega - \phi' | \quad (65)$$

when $\phi \geq 180^\circ$, $\phi = 360^\circ - \phi$, and the local momentum flux is obtained from Equation (18) or (19) as $f(\phi)$ or $f(\phi')$ accordingly.

3.3.3 Determination of Wall-Jet Momentum Flux Entering the Base of a Fountain—A stagnation line pattern for a typical four jet case is shown schematically in Figure 31. The total momentum flux to the base of the fountain located above a stagnation line segment such as A-B in Figure 31, is obtained by integrating the momentum flux in a sector subtended by the angles ϕ_A' and ϕ_B' also shown in Figure 31. The geometry is defined by the appropriate values of coordinates of the points A and B as determined by the stagnation line solution for wall-jets 2 and 3.



DP77 0374 88

FIGURE 31
GEOMETRY FOR DETERMINATION OF MOMENTUM FLUX INTO FOUNTAIN BASE
(STAGNATION LINE) SEGMENT A-B

The total flux of momentum entering the arbitrary fountain base segment A-B is given by *

$$\dot{M}_{FAB} = \frac{\dot{N}_{13}}{2\pi} \gamma_{A3} \int_{\phi_A}^{\phi_B} f(\phi) d\phi_2' \quad (66)$$

* The expressions developed in Reference 11 for the momentum flux entering the bases of three and four jet fountains are more restrictive since, for the case of non-vertical jet impingement, the radial wall-jet momentum flux is dependent on the local radius R about the impingement point. This is indicated by Equation (40). This R dependence apparently necessitated the assumption of a "dividing streamline" perpendicular to the line connecting the jet impingement point pair for the fountain base momentum flux determination in Reference 11. Through the use of Equation (66), the coordinates of each point in the stagnation line segment in the ground plane are not required.

the angle ϕ in Equation (66) is related to the angle ϕ_2' through the use of Equation (65) applied at impingement point number three, i.e.

$$\phi = |\gamma_3 + 180^\circ - M 360^\circ - \omega_3 - \phi_2'| \quad . \quad (67)$$

The formulation of the momentum flux given in Equation (66) requires values of pertinent angles in the local flowfield only, and does not depend on the value of the local radius R about the local impingement point. This is a direct result of the independence of wall-jet radial momentum from local radius about the jet impingement point (see Figure 20).

4. CALCULATION OF THE INDUCED FLOW FIELD

For a VTOL configuration in hover, the mass entrainment of the free-jets and wall-jets induces an external flow field surrounding the aircraft. Because the induced field is essentially incompressible, inviscid, and irrotational, potential flow theory can be employed to calculate the resultant forces and moments.

The pertinent flow boundaries are illustrated in Figure 2. In accordance with the methodologies of the preceding sections, the geometry and mass entrainment rates for both free and wall-jets can be calculated. For application to potential flow theory, the distribution of mass entrainment rates provides prescribed normal velocity boundary conditions on the jet surfaces. Simultaneous boundary conditions for the aircraft are obtained corresponding to flow tangency requirements on all solid surfaces. The complete distribution of Neumann normal velocity boundary conditions is theoretically sufficient to determine the entire induced flowfield, including the aircraft pressure distribution.

The Douglas Neumann Three-Dimensional Potential Flow Computer Program (Reference 16) was selected as the fundamental tool for calculating the induced field. Section 4.1 briefly describes the program and explains the motivation for its selection. Program modifications which tailored the Douglas Neumann method to VTOL applications are described in Section 4.2. In addition to allowing for arbitrary Neumann boundary conditions, these modifications simplify user input requirements and provide increased accuracy and efficiency for configurations with wall-jets. Section 4.3 presents the results of numerical experimentation conducted to establish program user guidelines for jet-induced flow problems.

A detailed user's manual for the modified program has been written (Reference 17). The manual contains complete input instructions for the program plus sample input/output for a simple but illustrative case.

4.1 The Douglas Neumann Method

The Douglas Neumann method is based on the fact that any incompressible potential flow velocity field can be considered as being induced by a particular surface distribution of source singularities on all flow boundaries. For example, in jet interaction problems the appropriate boundaries of the inviscid flowfield are the aircraft surface, free-jet surface, and wall-jet surface. The Douglas Neumann solution philosophy involves the representation of a continuous source distribution over the boundaries by a discrete distri-

bution of constant strength source quadrilateral panels. A consequence of the linear nature of potential flow is that the complete velocity at any field point is simply the linear combination of free stream velocity plus the sum of the velocities induced by each individual source panel. Furthermore, the velocity induced by a single source panel is directly proportional to the panel source strength. Consequently, it is possible to establish a system of linear algebraic equations relating prescribed normal velocity boundary conditions at discrete control points to the unknown panel source strengths. Solution to the system of equations generates the complete source distribution which is used to calculate the complete velocity vector at any point of interest in the potential field. Use of the Bernoulli equation converts velocity magnitude to local pressure coefficient for use in force and moment integration.

The modeling of arbitrary flow boundaries by a quadrilateral panel network is illustrated in Figure 32, where the paneled boundaries include the aircraft, free-jets, and ground wall-jets. The paneled geometry is dictated by the user, who must input the corner point coordinates of each panel. Except at boundary edges, each corner point is common to four adjacent panels. The four corner points which define a panel need not be exactly coplanar, because the program automatically generates the flat panel having the least square error at the corners.

Prescribed Neumann Boundary Conditions

Zero Normal Velocity on Aircraft

Entrainment Normal Velocity on Jets

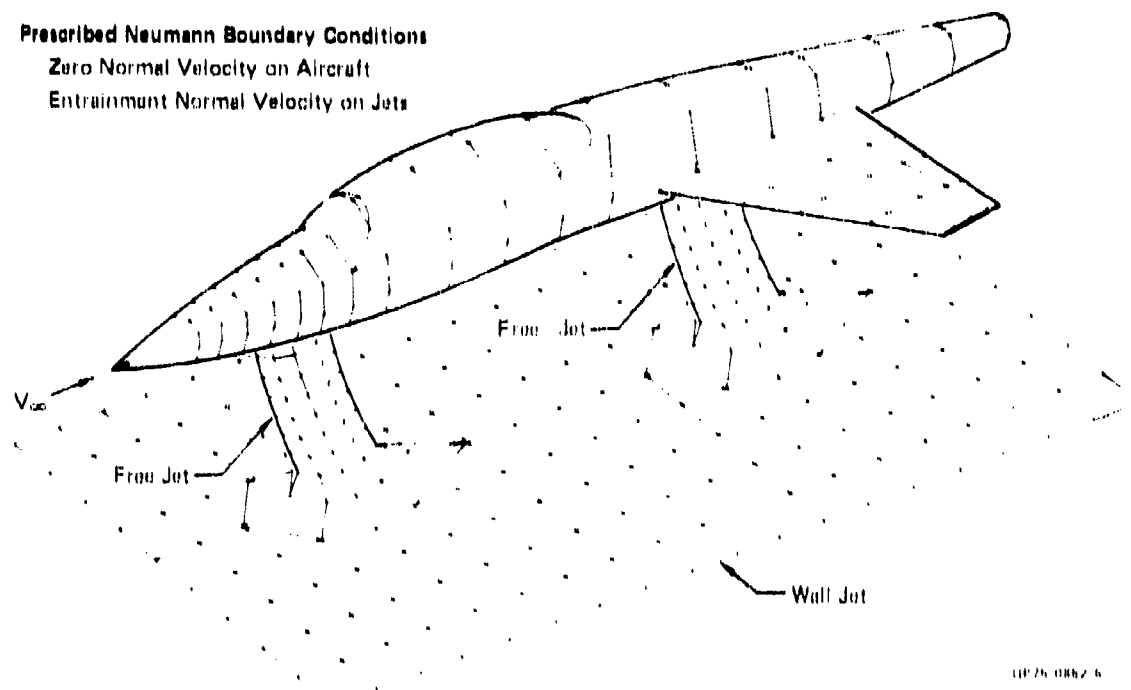


FIGURE 32
DOUGLAS NEUMANN PANEL MODELING

Paneling a configuration is somewhat of an art and requires knowledge of basic procedural rules. The program allows a maximum of one thousand panels, which will provide adequate accuracy for typical configurations. Panels with large taper ratios or high aspect ratios should be avoided where possible. Greater panel density should be applied in regions of strong pressure gradient, typically where surface curvature is highest. Thin geometries require increased panel density, and it is important that panel corner points be aligned on opposite surfaces of a thin geometry.

Selection of the Douglas Neumann program was predicated upon a careful trade off of advantages and disadvantages. A desirable feature of the program is the fact that no small disturbance assumptions are made. Therefore, the prediction accuracy is limited only by the number of panels; as this number increases without bounds, the calculated numerical solution will approach the exact analytical potential flow solution. The wide acceptance and extensive checkout by both industry and government personnel provide a degree of confidence in the capabilities and coding accuracy of the Douglas Neumann method. Presently, an automatic geometry paneling routine is being developed by Douglas Aircraft Company under contract to NASA Langley Research Center. Upon completion, this routine can be coupled directly with the existing program to provide a simplified user-oriented package.

However, there are two disadvantages to the Douglas Neumann method that require recognition. First, the computational expense tends to increase with the cube of the number of panels N , while prediction accuracy only increases linearly with N . Therefore, prediction accuracy tends to vary as computational expense to the third power. Second, numerical instabilities can be generated if the program is applied to thin lifting geometries because source strength magnitudes become excessively large. Fortunately, work is in progress to alleviate these two shortcomings.

The higher order curved panel approach of Hess (Reference 18) will generate prediction accuracies that vary as computational expense to power two instead of power three, and this approach is presently being formulated and coded for the three-dimensional program by Douglas Aircraft Company under contract to NADC.

The thin surface anomaly can be eliminated by incorporating the mild source-doublet combination corresponding to the classical Green's Identity relationship (Reference 19). McDonnell Aircraft Company has modified the two-dimensional Douglas Neumann method by implementing a recently developed Green's Identity formulation (Reference 20). Typical numerical results are

presented in Figure 33, where a supercritical airfoil in incompressible flow and 4° angle of attack was modeled by 40 panels. A conformal mapping solution by the method of Cathall-Sells (Reference 21) provides a virtually exact two-dimensional pressure distribution for purposes of comparison. The Cathall-Sells value of lift coefficient ($C_L = 0.905$) was prescribed for each of three panel methods to prevent the possibility of arbitrary Kutta condition selection clouding the comparison. The conventional low order Douglas Neumann solution is seen to deviate significantly from the exact solution near the thin highly loaded trailing edge. Resorting to the higher order curved panel approach with the Douglas Neumann program is seen to improve, but not eliminate the anomaly. However, using the Green's Identity approach with the higher order curved panels virtually eliminates the trailing edge problem. Furthermore, the Green's Identity solution is at least as accurate as each of the other two panel solutions over the entire remainder of the airfoil surface. McDonnell Aircraft Company is presently under contract to NASA Langley Research Center to modify the three-dimensional Douglas Neumann program to accommodate the Green's Identity formulation.

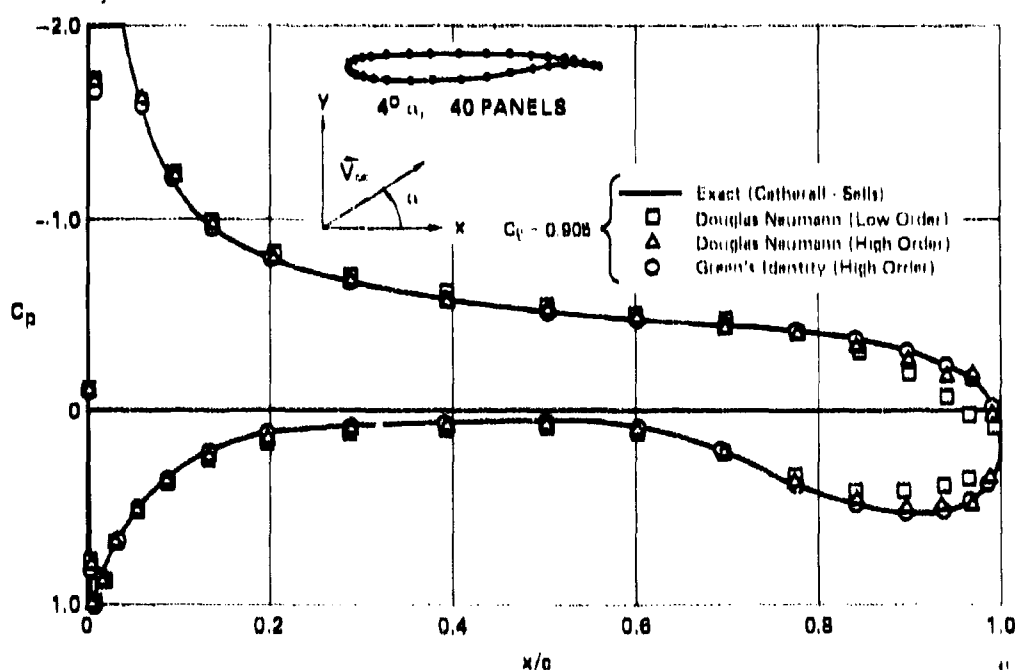


FIGURE 33
SUPERCritical AIRFOIL PRESSURE DISTRIBUTION

It is apparent that the shortcomings of the Douglas Neumann three-dimensional program should be balanced against the fact that significant improvements to the program are currently under development. It is therefore reason-

able to select the conventional Douglas Neumann program as the basic potential flow tool for this study, with the knowledge that in the future, the improvements being made under other independent studies can be merged to form one highly flexible, efficient, and accurate potential flow computer program.

4.2 Modifications to Douglas Neumann Program

In order to facilitate the application of the three-dimensional Douglas Neumann program to typical aircraft/jet/ground interaction problems, the five program modifications to be discussed below have been implemented and fully checked out. These modifications impose minimal workload on the program user and do not impair any existing program capabilities.

4.2.1 Option to Allow Arbitrary Neumann Boundary Conditions - In the formulation and coding for the existing Douglas Neumann program in Reference 16, flow tangency boundary conditions are assumed to apply on all boundary surfaces. Since prescribed entrainment normal velocities on jet boundaries violate this restriction, it was necessary to modify the program to accept an arbitrary prescribed value of normal velocity as the boundary condition at each panel control point. The modification was accomplished in a fashion such that the user need prescribe values only on geometric sections selected by him and the program will assume flow tangency elsewhere. For example, on solid aircraft surfaces no normal velocity values need be input since the program will assign a zero value on these panels automatically.

4.2.2 Option to Allow Wake-Free Configuration - The existing program always assumes the presence of a trailing vortex wake, characteristic of the flowfield induced by an aircraft in forward flight. For VTOL aircraft in hover, the effects of wind gusts are usually no more significant than the jet-induced flowfield, thereby invalidating the concept of a trailing wake. The program was therefore modified to accept either the presence or absence of a trailing vortex sheet at the discretion of the user.

4.2.3 Simplified Geometry Modification Option - The existing program required geometric coordinates to be input at the rate of two points per card. Therefore, if the user desired to make a localized geometry modification he was forced to add or delete an even number of points or else face the prospect of repunching input cards for every subsequent point (possibly several thousand values). The program was therefore modified to allow an arbitrary mixture of cards each having coordinates for either one or two points. The modified program now assumes each card to have two points unless a non zero value is placed in card column 70, at which time the program automatically accepts just the desired single point coordinates on the card.

4.2.4 Coordinate Transformation Option - The existing program assumed all geometric panel coordinates to be input in a common Cartesian coordinate system. Therefore, if the user desired to change an aircraft attitude or location with respect to a ground plane, every aircraft coordinate had to be recomputed by hand and repunched on cards. The coordinate transformation option enables the user to arbitrarily move an individual geometry section such as a wing, fuselage, or jet without disturbing the remainder of the geometry. For example, the roll, pitch, and height of the aircraft in Figure 32 could easily be changed with respect to the ground plane.

The transformation procedure consists of rotation first, translation second. If the panel input coordinates of a section are in the (x_1, y_1, z_1) system of Figure 34, the program rotates the coordinates through Euler angles Ψ , then θ , and finally ϕ , where these angles are arbitrary input values. Next, the rotated coordinates are translated by arbitrary input values Δx , Δy , and Δz . The formulas relating the input coordinates (x_1, y_1, z_1) to the final transformed coordinates (x, y, z) follow.

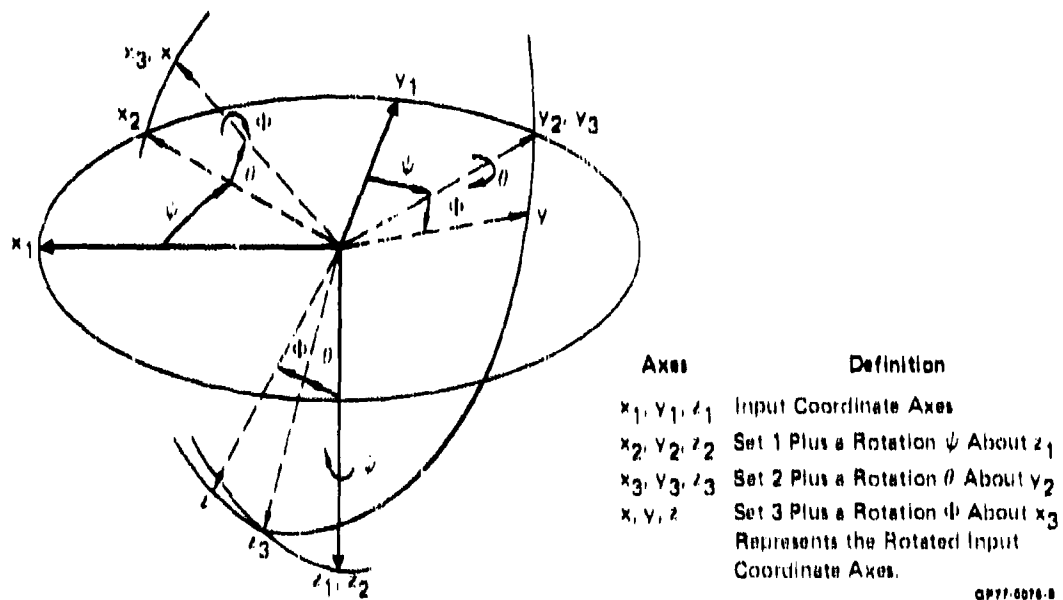


FIGURE 34
COORDINATE TRANSFORMATION OPTION: ROTATION

$$x = \Delta x + l_1 x_1 + m_1 y_1 + n_1 z_1 \quad (68a)$$

$$y = \Delta y + l_2 x_1 + m_2 y_1 + n_2 z_1 \quad (68b)$$

$$z = \Delta z + l_3 x_1 + m_3 y_1 + n_3 z_1 \quad (68c)$$

$$\begin{aligned}
\text{where } x_1 &= \cos \theta \cos \psi \\
m_1 &= \sin \phi \sin \theta \cos \psi - \cos \phi \sin \psi \\
n_1 &= \sin \psi \sin \phi + \cos \phi \sin \theta \cos \psi \\
x_2 &= \cos \theta \sin \psi \\
m_2 &= \cos \phi \cos \psi + \sin \psi \sin \phi \sin \theta \\
n_2 &= \sin \phi \cos \psi + \sin \psi \cos \phi \sin \theta \\
x_3 &= -\sin \theta \\
m_3 &= \cos \theta \sin \phi \\
n_3 &= \cos \theta \cos \phi
\end{aligned}$$

The coordinate transformation option is of limited value for conventional aerodynamic problems, but is essential for V/STOL aerodynamics in which roll, pitch, and ground height are commonly varied parameters.

4.2.5 Modified Method of Images Option - For the solution to aircraft-jet ground interaction problems, the application of a method of images concept generates significant improvements in both computational efficiency and prediction accuracy. This concept has been implemented in the Douglas Neumann Program as an option designated "Modified Method of Images". Subject to the mild restriction that all wall-jet panels lie in a common plane, the modified method of images approach eliminates as unknowns the source strength densities on the wall panels. Because the computing time required to solve a system of linear equations is proportional to the cube of the number of unknowns, even a small reduction in unknowns will be significant for the large number of panels associated with V/STOL aerodynamics.

The basic geometry paneling for the modified method of images is illustrated in Figure 35. In addition to the aircraft, free-jet, and wall-jet paneling, the program will automatically panel an image aircraft and image free-jet upon activation of the modified method of images option. The presence of the image panels violates no theoretical restrictions because they do not lie within the actual inviscid flowfield. For each unknown source density on an aircraft or free-jet panel, there is an equal strength source density on the corresponding image panel. By symmetry, the normal velocity induced by the aircraft and free-jet panels plus image panels at any point on the wall-jet will be identically zero. Therefore, the net normal velocity on the wall-jet is attributable only to the freestream component plus the component induced by the wall-jet source distributions. Under the restriction that the wall-jet panels are coplanar, this latter component can be shown to be exactly twice the local source density. Since the net normal velocity on the wall-jet is prescribed as a boundary condition from the known wall-jet entrainment velocities, it is possible to determine the source density dis-

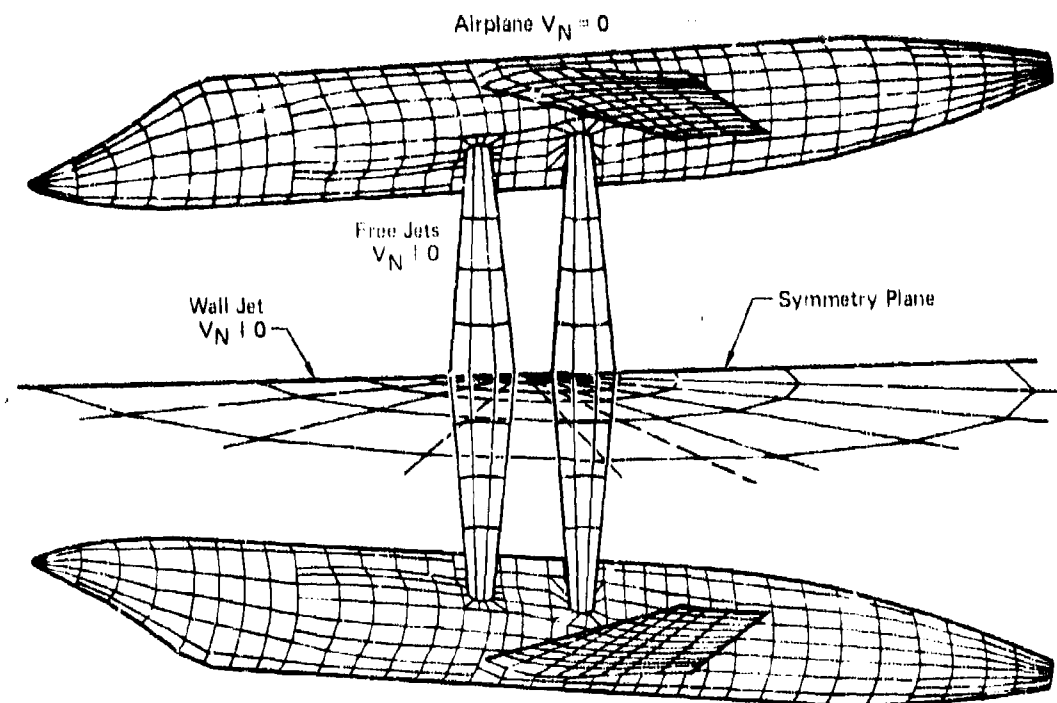


FIGURE 35
SAMPLE PANELLED GEOMETRY FOR THE MODIFIED
METHOD OF IMAGES OPTION
 Airplane - Free Jet - Wall Jet

GP 77 0374 23

tribution on the wall-jet panels immediately without solving for aircraft and free-jet source densities. Therefore, the velocity field induced by the wall-jet can be computed beforehand. The only remaining unknowns to be solved are the source densities on the aircraft panels and free-jet panels where the known entrainment velocities V_N of themselves determine the source densities. The extra expense required in calculating the image panel influence coefficients is typically insignificant because the simple flowfield formulas of Hess (Reference 16) are employed whenever the distance to an influenced point is sufficiently large compared to the influencing panel dimensions. A secondary advantage of the modified method of images is that the boundary conditions will be more nearly satisfied between wall-jet panel control points than in the conventional solution approach, which is a consequence of the fact that symmetry conditions apply at all points in the wall-jet instead of control points only.

Because the program allows more than one symmetry plane, the modified method of images option does not force the user to panel both the right and left-hand-sides of a symmetrical aircraft above a wall-jet.

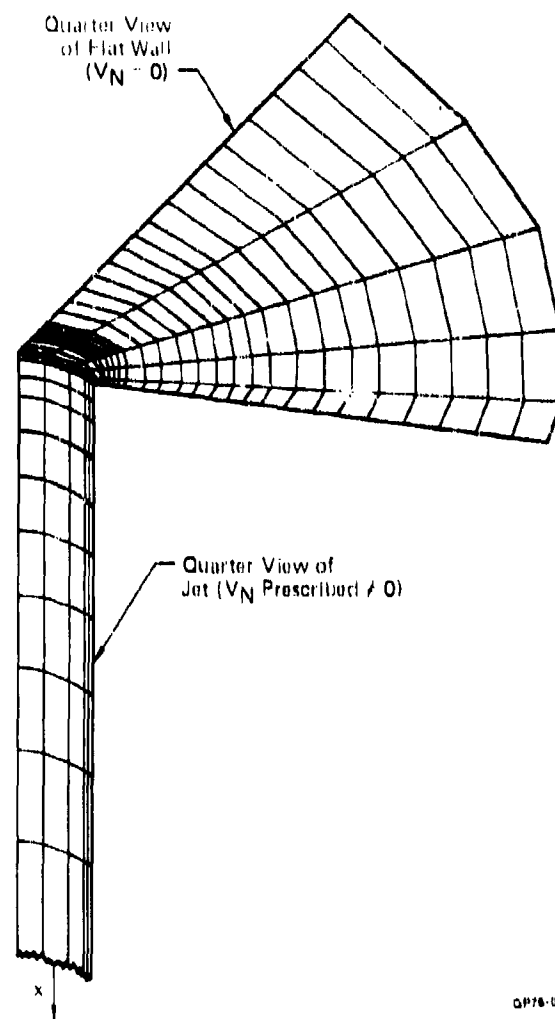
4.3 Numerical Experiments with Douglas Neumann Program

Because previous applications of the Douglas Neumann program to jet interaction problems have been limited, it was considered beneficial to conduct a sensitivity study of jet panel modeling effects on calculated solutions. Such a study would reveal basic user paneling rules and indicate the proper degree of prediction accuracy versus panel density.

In accordance with the philosophy that the simplest possible case should be used to isolate numerical trends, a systematic panel study was conducted for an axisymmetric jet exhausting from an infinite flat wall. This simple case is especially attractive because both experimental data and an alternate exact potential flow solution are available for the wall pressure distribution (Reference 22).

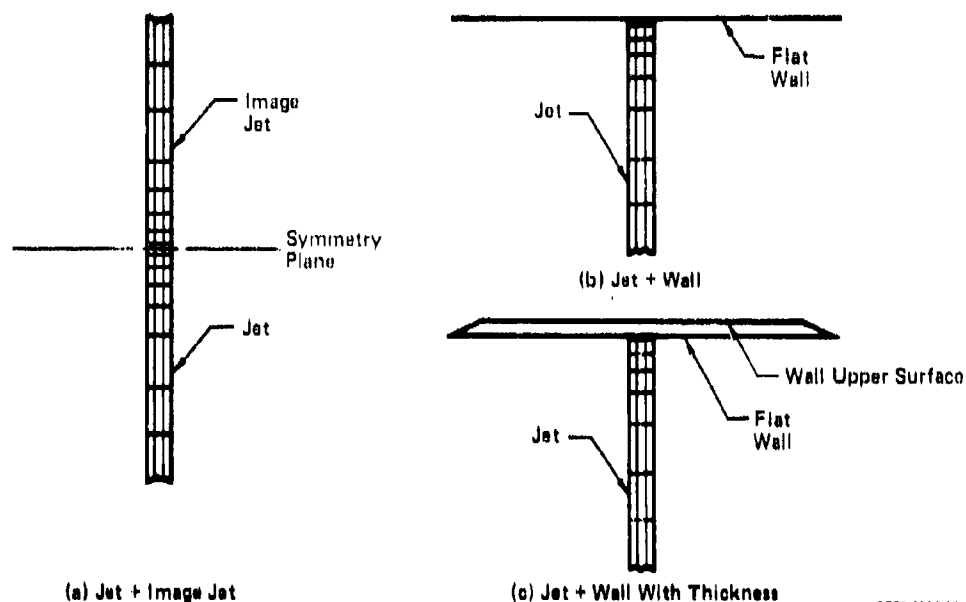
The basic panel model is illustrated in Figure 36. Entrainment normal velocities consistent with those of Reference 22 are prescribed on the jet, and flow tangency is prescribed along the flat wall. The entrainment normal velocity distribution, from Reference 22, is $V_N = -.032 V_{je}$ for $0 \leq Z \leq 6 D_j$ and $V_N = -.114 V_{je}$ for $Z > 6 D_j$. The pressure coefficient is defined as the negative of the square of the ratio of local speed to V_{je} .

The objective of the study was to determine the sensitivity of the calculated wall pressure distribution to systematic changes in the basic panel modeling of Figure 36. In that regard, five separate panel modelings were established. The first modeling was generated by removing the wall panels of the basic setup of Figure 36 and then adding an image jet in accordance with the method of images (Figure 37a). Illustrated in Figure 37b are the second, third, and fourth models. The second model is simply the basic setup of Figure 36. To demonstrate the effect of reduced panel density, the third model was created from the basic setup by a fifty percent reduction in panel density both on the jet in the axial direction and on the wall in the radial direction away from the jet axis. The fourth model was established by extending the flat wall of the basic setup across the jet exit, thereby effectively capping the jet. A total of eighty panels (twenty per quarter view) were used to cap the jet, and flow tangency boundary conditions were applied to each such panel on the side facing the jet ($x = 0^+$). The fifth model represents a jet emanating from a wing of small, but finite thickness (Figure 37c). The paneling was established by adding an upper surface wall to the basic setup. The wall upper surface panel corner points project onto the lower surface corner points, in accordance with a basic panel rule of Hess. Flow tangency was prescribed on both the upper and lower surface of the wall, in order to characterize a wing-type configuration.



GP76-0984-14

FIGURE 36
PANEL MODEL FOR AN AXISYMMETRIC JET EXHAUSTING
FROM A FLAT WALL



CP76-0984-13

**FIGURE 37
THREE PANEL MODELS OF AN AXISYMMETRIC JET EXHAUSTING
FROM A FLAT WALL**

Calculated results for the wall pressure and source density distributions appear in Figures 38 through 41. Of the five panel models, the one incorporating the method of images is of necessity the most accurate because symmetry guarantees the absence of leakage anywhere on the wall plane. A comparison (Figure 38) of the wall pressure distribution calculated by the Douglas Neumann program using the jet plus image jet paneling (Figure 37a) demonstrates excellent agreement with both experimental and analytical values from Reference 22. The analytic curve was obtained by assuming the jet to be a concentrated source filament and then applying the method of images. Virtually all the discrepancy between the analytic curve and the calculated Douglas Neumann values is attributed to the approximations associated with a finite panel density.

Errors associated with the introduction of the flat wall panels are evident in Figure 39 for both the dense and sparse paneling of Figure 37b. Calculated pressures are quite good except for the five or six panels closest to the jet. It is noted that within this region, the sparse panels introduce approximately twice the relative error of the dense panels, which is a consequence of the fact that the low order approach of the existing program generates prediction accuracy that varies as the first power of panel density. However, the simple technique of capping the jet eliminates most of

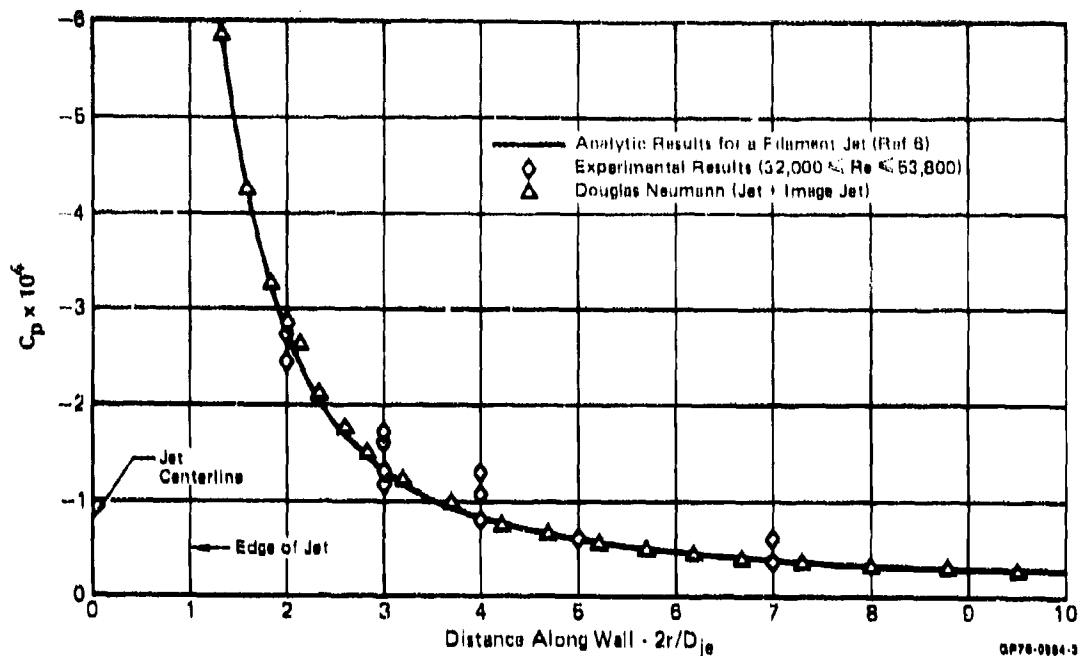


FIGURE 38
PRESSURE DISTRIBUTION DUE TO AN AXISYMMETRIC JET

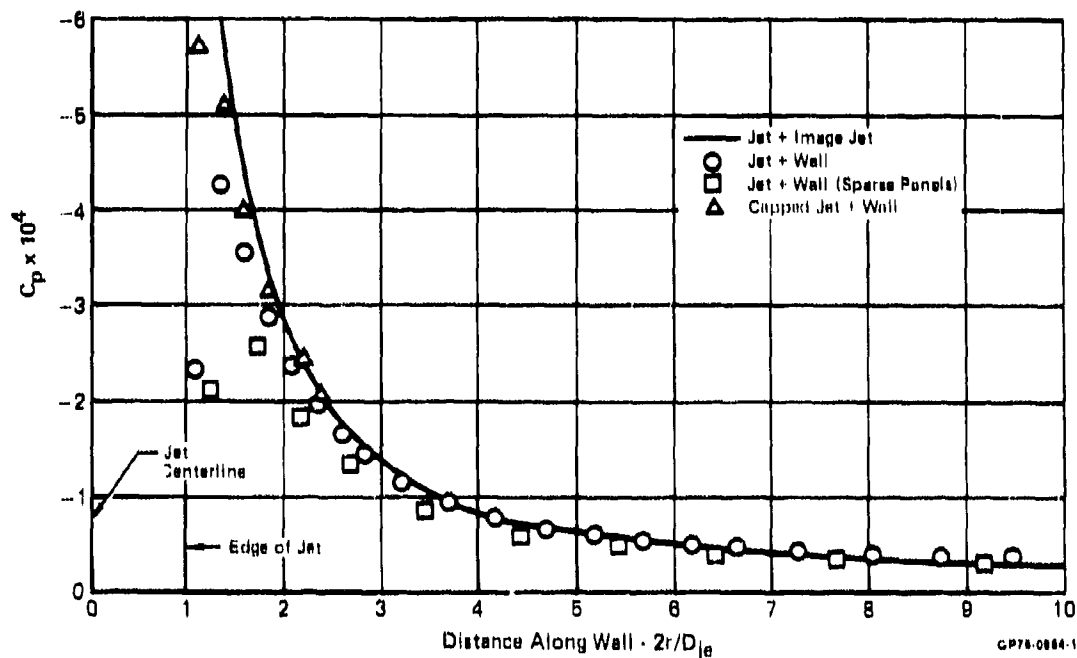


FIGURE 39
PRESSURE DISTRIBUTION DUE TO AN AXISYMMETRIC JET CALCULATED BY
THE DOUGLAS NEUMANN PROGRAM

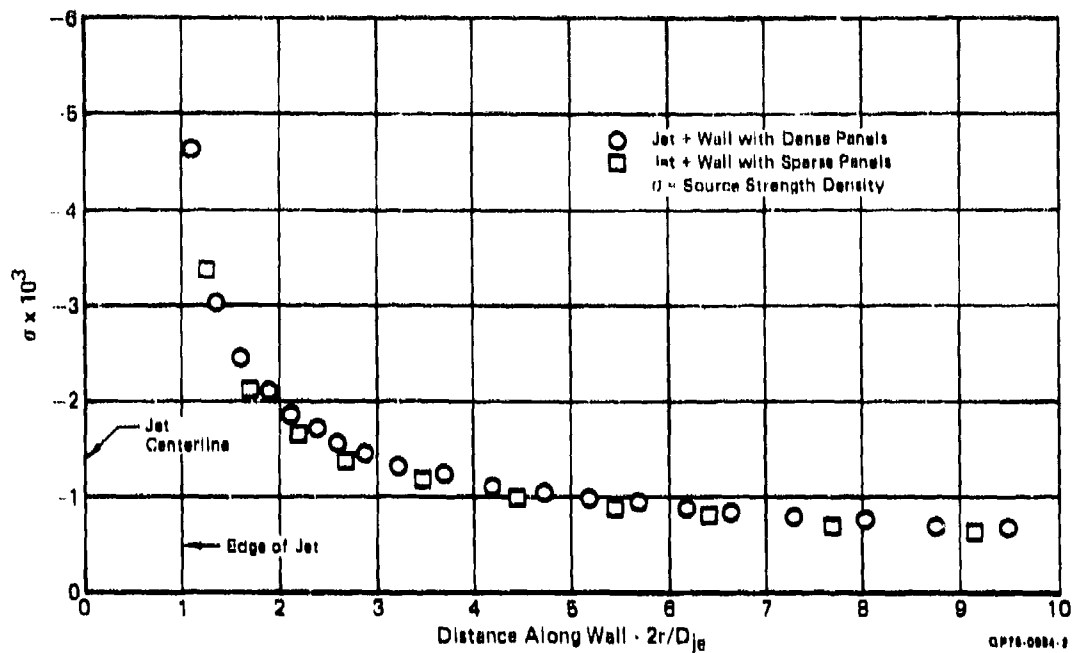


FIGURE 40
SOURCE DISTRIBUTION DUE TO AN AXISYMMETRIC JET CALCULATED
BY THE DOUGLAS NEUMANN PROGRAM

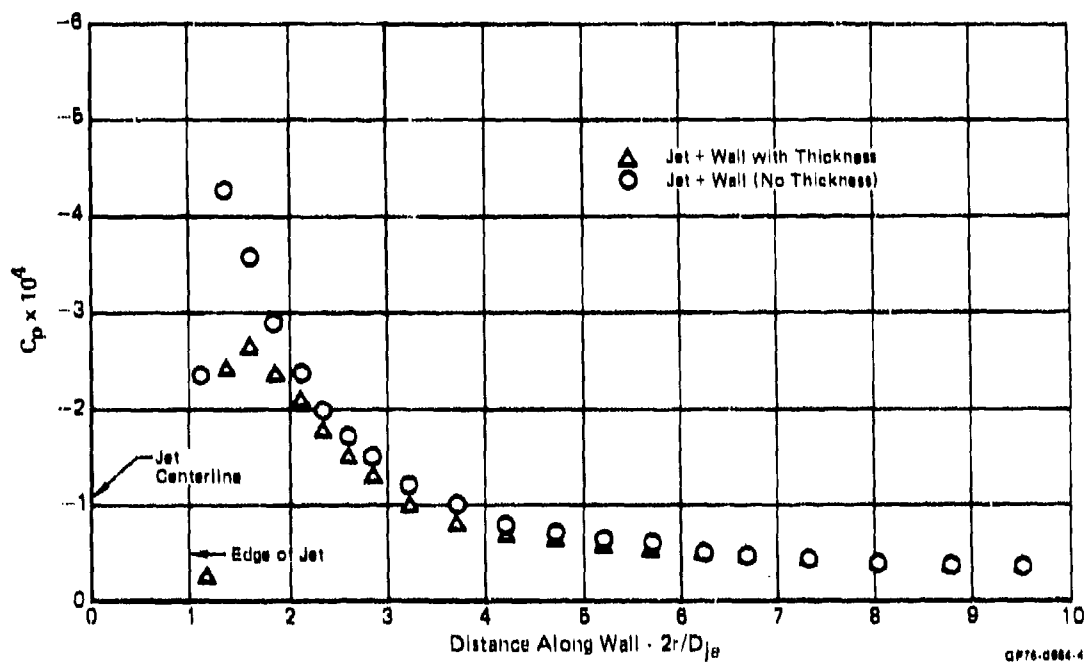


FIGURE 41
PRESSURE DISTRIBUTION DUE TO AN AXISYMMETRIC JET CALCULATED
BY THE DOUGLAS NEUMANN PROGRAM

the problem, but at the expense of adding more panels. Corresponding to the calculated pressure distribution of Figure 39 are the calculated wall source distributions of Figure 40. The close agreement between the source distributions is expected for a flat wall. The disagreement in pressure distributions is simply attributable to the neglect of source gradients on a panel, which is obviously of increasing importance near the edge of the jet.

Figure 41 demonstrates that the addition of the wall upper surface thickness impairs the calculated pressure distribution within approximately five panel widths of the jet edge. Again, however, the results are good outside this range.

It is concluded that:

- (1) The method of images should be used where possible.
- (2) Panel density should increase near the juncture of a jet and solid surface.
- (3) Prediction accuracy is proportional to panel density.
- (4) Wings with thickness require greater panel density than infinite flat walls.
- (5) Jets should be capped with additional panels.

A complete user's manual for the modified Douglas Neumann program is available (Reference 17). In accordance with the user's manual instructions, a four lift-jet VTOL attack aircraft in hover was panelled for the program. The set-up incorporated approximately one thousand panels to model the left-hand-side of the aircraft/free-jet/wall-jet configuration. Approximately three man-weeks (120 hours) were required to complete the panelling. On the IBM 360, the computing time for one complete solution was fifteen minutes. Several values of free-stream or cross-wind velocity can be computed for a fixed geometry at no significant increase in computing time.

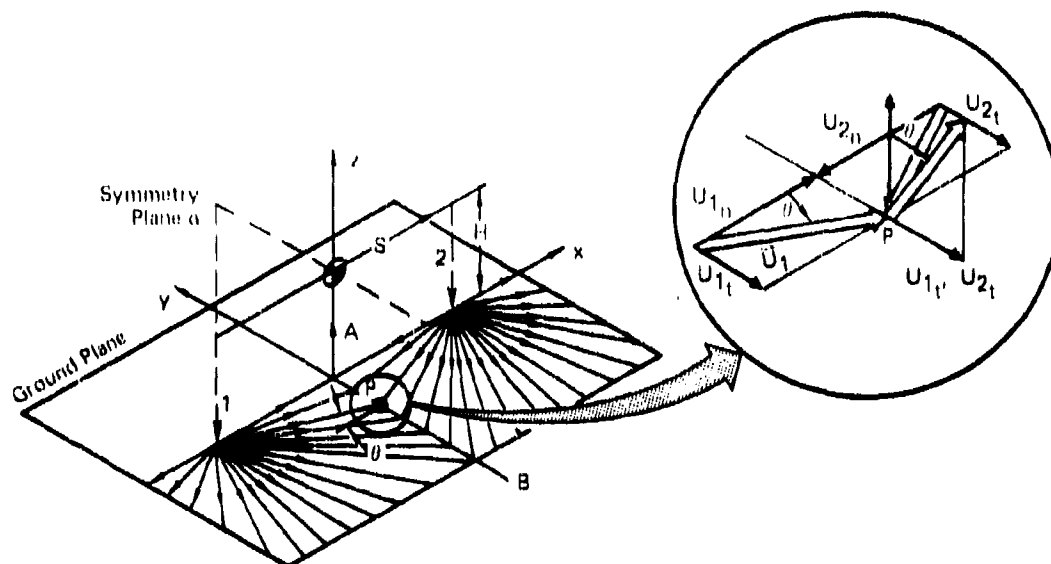
5. FOUNTAIN UPWASH FLOW CHARACTERISTICS

The study of fountain flow characteristics has concentrated on cases where the jets are circular, perpendicular to the ground plane, and of equal thrust. In addition, the pattern in which the nozzles are arranged has been usually assumed to possess at least one plane of symmetry. The existence of one or more planes of symmetry simplifies the flowfield geometry considerably, and leads to a better understanding of the fundamental fountain upwash properties. For a configuration with two perpendicular jets of equal thrust, certain assumptions about the flow turning process result in an analogy between the fountain and a jet. Basic features of this analogy have been verified in a test program conducted in a parallel MCAIR IRAD effort. Based upon the two-jet results, the analogy between fountains and jets has been extended to configurations with three and four perpendicular jets of equal thrust.

An initial, qualitative description of the upwash in asymmetric two-jet fountains has been developed, and a plausible analogy between the fountain and a conical flow has been postulated. A quantitative description of the flowfield is not possible at present, however, due to a lack of adequate data for this type of three dimensional fountain.

5.1 Equivalence Between Symmetric Two-Jet Fountains and Radial Jets

The simplest possible fountain flow is that generated by the jet arrangement shown in Figure 42. Two circular jets of equal diameter and thrust impinge at 90° to the ground plane. The jets are separated by a distance S and located at an equal height H from the ground. The wall-jets flow radially outward from the impingement point below each vertical jet, and separate along the line AB to form the fountain. Because of symmetry, the separation line AB is straight and is located halfway between the jet impingement points. The entire flowfield, including the fountain, is symmetric about plane α (and also about the plane containing the jet centerlines). The radial lines emanating from the impingement points represent the direction of flow in the axisymmetric wall-jets. Oilflow studies of jet impingement patterns indicate that as the separation line AB is approached, the oil flow lines curve and become tangent to this line, but the region of curvature is limited to the immediate neighborhood of the line. At the line AB, the wall-jets turn and leave the surface, forming the fountain. The turning process is idealized as depicted in the enlargement of the flow region around point F shown in Figure 42. The vectors \vec{U}_1 and \vec{U}_2 are velocities in the wall-jet profiles corresponding to jets 1 and 2, respectively. These vectors have normal (subscript n) and tangential (subscript t) components to the separation line AB. It is assumed

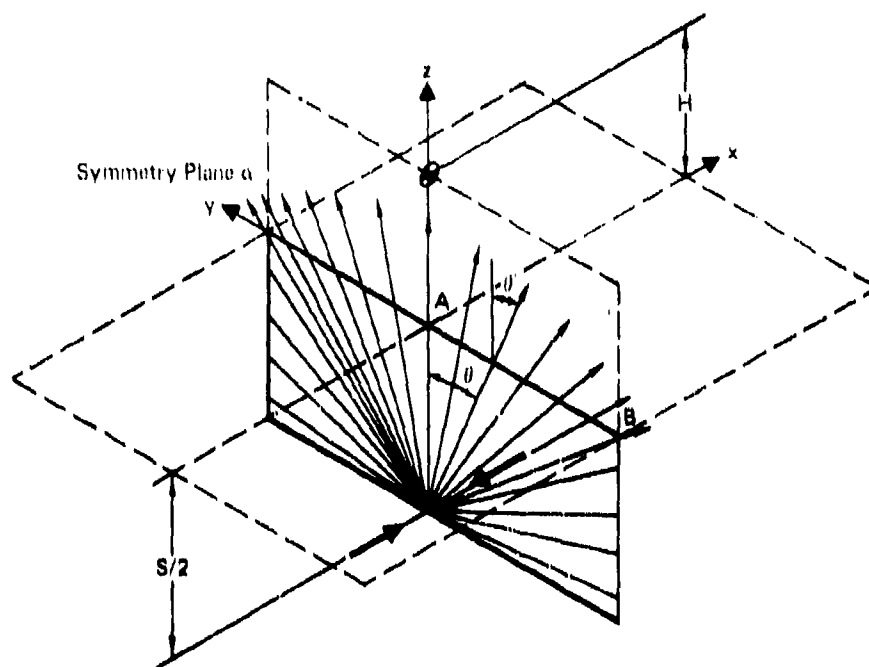


NP77 0374 78

FIGURE 42
IDEALIZED WALL JETS AND FOUNTAIN TURNING
Two Symmetric Jets

that in the turning process, the normal velocity components U_{1n} and U_{2n} are rotated to be perpendicular to the ground plane, and the tangential components U_{1t} and U_{2t} are unchanged. Thus, the angle θ as defined in Figure 42 is preserved in the turning process. With the exception of the immediate neighborhood of the stagnation line, to a first approximation the static pressure in the fountain is taken to be constant. Consequently, streamlines in the fountain are straight, and the fountain velocity profile remains at an angle θ to the vertical. The angle θ is different for different points along AB, and the flow is equivalent to what would be obtained by folding the ground plane along the separation line AB, which causes the impingement points for jets 1 and 2 to rotate by 90° . This process is illustrated in Figure 43. The flow in the fountain would then be analogous to a radial flow originating from a virtual origin located at a distance $S/2$ below the ground plane. A radial flow such as this may be generated by two opposing axisymmetric jets which impinge upon each other. Flows of this type have been extensively studied in Reference 8.

In order to verify the postulated analogy between a symmetrical two-jet fountain and the flow in a radial jet, a test was conducted as part of a MCAIR IRAD program (Reference 23). Properties of the fountain flowfield were investigated by means of flow visualization and flowfield surveys with a total pressure



GP77-0374-80

FIGURE 43
EQUIVALENCE BETWEEN TWO-JET FOUNTAIN AND RADIAL JET

rake. The results are compared to data obtained from pressure surveys of an axisymmetric radial jet created by the impingement of two opposed, circular jets. The apparatus consisted of a pair of 1.05 in. ID pipes, supplied with high pressure air. For the fountain studies, the pipes were arranged so that they impinged at 90° to a ground board, as indicated in Figure 42. One value of $H = 2.0d_{je}$ was used, and three values of

$$S/d_{je} = 3.81, 8, 12$$

were tested. The total pressure in the pipes was varied between

$$13 \leq p_{op} \leq 37 \text{ in Hg}$$

An oil film technique was used for flow visualization. A total pressure rake, located perpendicularly to the symmetry plane a in Figure 42 was used to survey the fountain velocity distribution. The probes were aligned with the local fountain velocity, using the flow visualization results. To generate a radial jet, the pipes were aligned end-to-end, so that the jets impinged on each other. One value of the jet spacing-to-diameter ratio

$$\Delta x/d_{je} = 0.5$$

was tested. Total pipe pressures of 30 and 40 psi were tested. Total pressure surveys were conducted with the rake perpendicular to the plane of the jet, and the probes were aligned with the radial velocity vector. (See Figure 43.) The output of the total pressure rake was read on water manometers, and the pipe total pressures were read on mercury manometers.

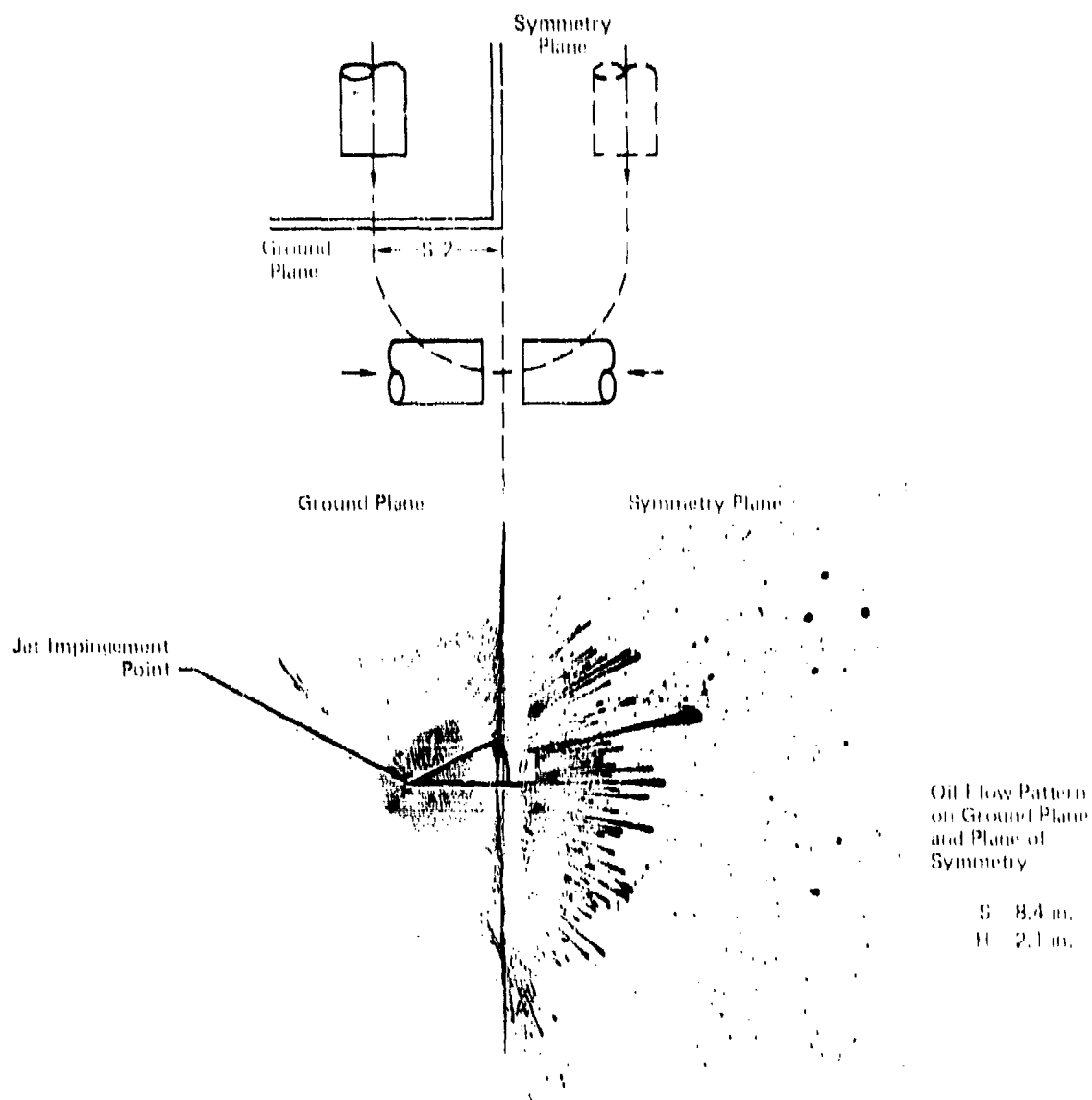
Figure 44 indicates the test arrangement used for fountain flow visualization. The plane of symmetry between the jets was replaced by a solid board, perpendicular to the ground board. A sheet of paper was attached to the ground and symmetry plane surfaces. An oil film was brushed on the paper, and the jet was then turned on. The resultant oil flow pattern is shown on the lower part of Figure 44, (after unfolding the sheet of paper). It is evident that the oil flow lines on the plane of symmetry are straight extensions of the oil flow lines on the ground plane, confirming the flow turning process described in Figure 42. The oil flow does indicate a region of separation right at the corner between the two planes, but this region is very small. Figure 44 shows the results for $S/d_j = 8$. Figures 45 a and b indicate a similar behavior for

$$S/d_j = 12 \text{ and } 6,$$

respectively. The photographs show that oil flow lines on the ground plane are slightly curved. This is due to the fact that in the experimental setup, the ground plane was located vertically.

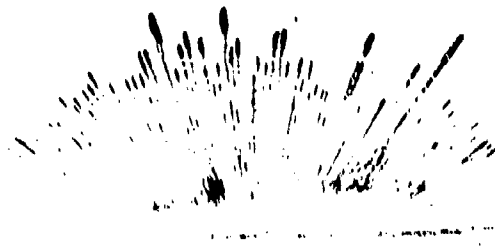
The oil flow data indicated that there is a qualitative equivalence between the flow in a symmetric, two-jet fountain, and a radial flow originating from a virtual origin located at a distance $S/2$ below the ground plane. Measured velocity profiles will now be compared to quantitatively verify the analogy between the fountain and a radial jet.

The first question to be investigated was whether the fountain flow was axisymmetric about the virtual origin. For this purpose, fountain velocity profiles were measured at constant values of the radius R from the virtual origin, and different values of θ , as indicated by the sketch in Figure 46. The plots in Figure 46 are fountain velocity profiles, normalized by the jet exit velocity V_{j0} , and plotted vs x (see Figure 42). Each plot corresponds to a different value of R . The curves indicate that for a fixed value of R , profiles at $\theta = 8^\circ$ and 20° are in good agreement. However, measurements at $\theta = 40^\circ$ show consistently higher velocity profiles. This would indicate that the fountain flow is not axisymmetric about the virtual origin. The result is somewhat inconclusive, however, because oil flow patterns on the ground board indicate that the jets producing the fountain are not quite axisymmetric.



GP77-0374-71

FIGURE 44
WALL JET AND FOUNTAIN FLOW VISUALIZATION



(a)

$S/d = 12$



(b)

$S/d = 6$

DB 7-0374 9

FIGURE 45
WALL JET AND FOUNTAIN FLOW VISUALIZATION
AT DIFFERENT VALUES OF JET SPACING

S: Jet Spacing
H: Height of Jet Nozzles
Above Ground Board - ($2 D_{je}$)

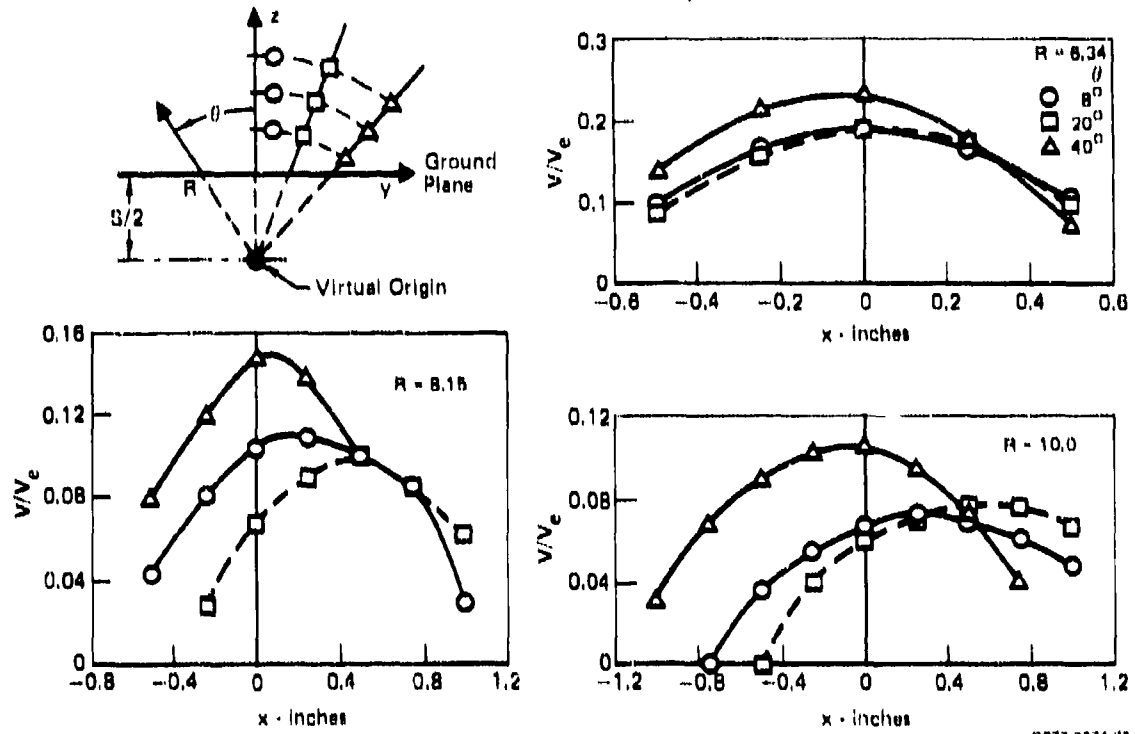


FIGURE 46
VELOCITY PROFILES IN TWO-JET FOUNTAIN $S/D_{je} = 8$

Figure 47 compares the fountain and radial jet velocity profile shapes at several values of the distance R from the fountain virtual origin, or from the radial jet's axis of symmetry. The velocities are plotted in similarity variables. That is, at any given value of R the velocities are normalized by the maximum velocity at that value of R , and the distance x is normalized by the distance $x_{1/2}$ at which the velocity has decayed to one half of its maximum value. The data show that the velocity profiles are approximately self-similar, since correlation is achieved for the fountain and jet profiles, for different values of R and values of θ up to 20° . The dotted curves in Figure 47 have been obtained from a fairing of the correlated radial jet data in Reference 8. The plots in Figure 47 then indicate that the measured fountain velocity profile is in good agreement with that for a radial, axisymmetric jet. Self-similarity of the fountain velocity profiles implies that its velocity field may be specified by the half-velocity width $x_{1/2}$ and the local peak velocity, V_m , in addition to the profile shape.

Figure 48 shows the dependence of $x_{1/2}$ on the distance R , for the radial jet and for the fountain. The fountain data show that $x_{1/2}$ grows linearly with R , independently of the jet spacing S/d_{je} and the pipe pressure. For the radial jet, $x_{1/2}$ also grows linearly and is independent of pipe pressure. The spreading rates for the fountain and radial jet tested are quite different. However, it has been shown in Reference 8 that the spreading rate for a radial jet depends on the spacing between the radially opposed nozzle exit planes, Δx_j . Figure 49 shows the spreading rate for radial jets, as a function of $(d_{je}/\Delta x)$. The curve is based on the data of Reference 8. When Δx is large, the opposed jets develop as free-jets before they impinge upon each other. The spreading rate of the resultant radial jet is then very high. As Δx decreases the spreading rate decreases, until a point is reached at which the space between the jet exit planes begins to act as an annular nozzle. With further decreases in Δx , the spreading rate becomes independent of Δx . In Reference 8, Witze refers to this type of radial jet as a "constrained" radial jet. The indicated fountain data lie fairly close to the constrained radial jet results from Reference 8.

Figure 50 shows the decay of the normalized peak velocity $(V_m/\sqrt{p_{0p}})$, as a function of distance from the fountain virtual origin, or distance from the radial jet axis. The data correlate well for different values of the pipe pressure. The fountain curves merge into the radial jet decay curves, but the value of $V_m/\sqrt{p_{0p}}$ depends on the jet spacing S/d_{je} . Figure 50 suggests that for different jet spacings S , the fountain may have to be simulated by constrained radial jets of different initial radius R_{je} .

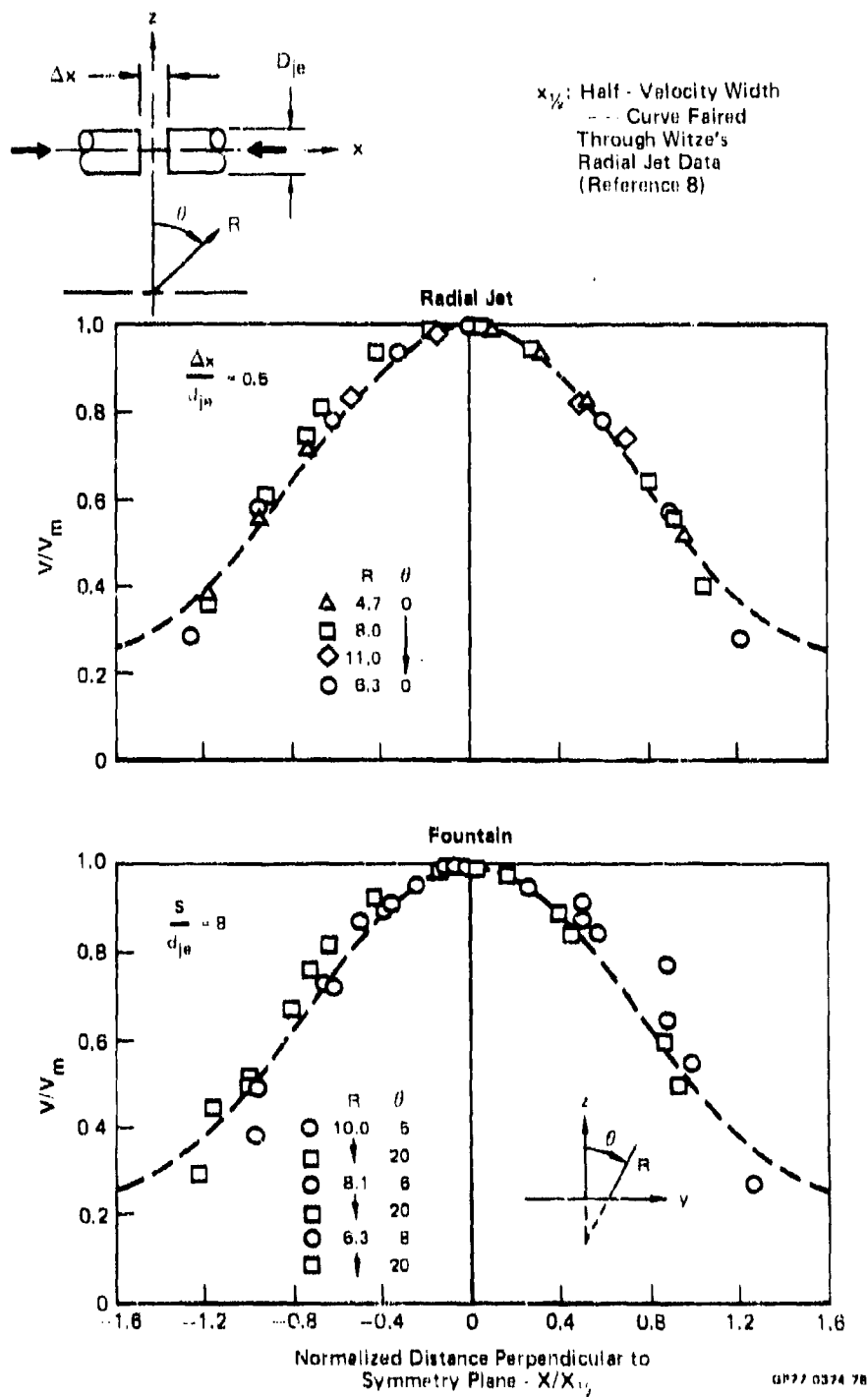


FIGURE 47
 RADIAL JET AND FOUNTAIN VELOCITY PROFILES

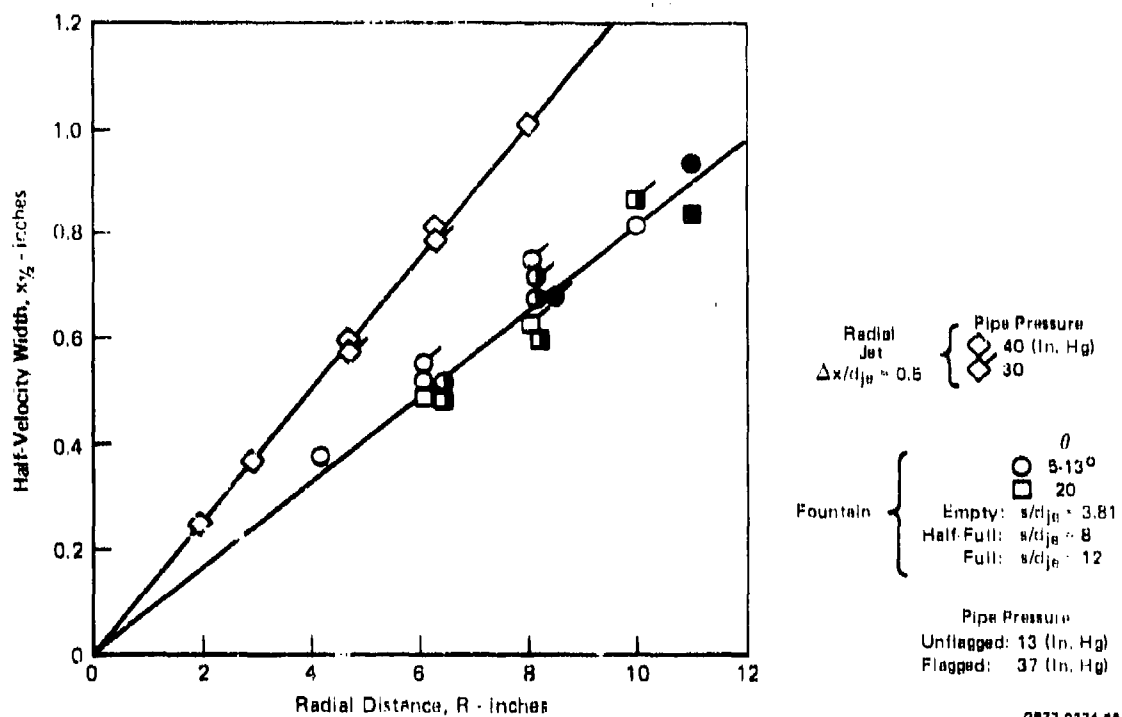


FIGURE 48
RADIAL JET AND FOUNTAIN SPREADING RATES

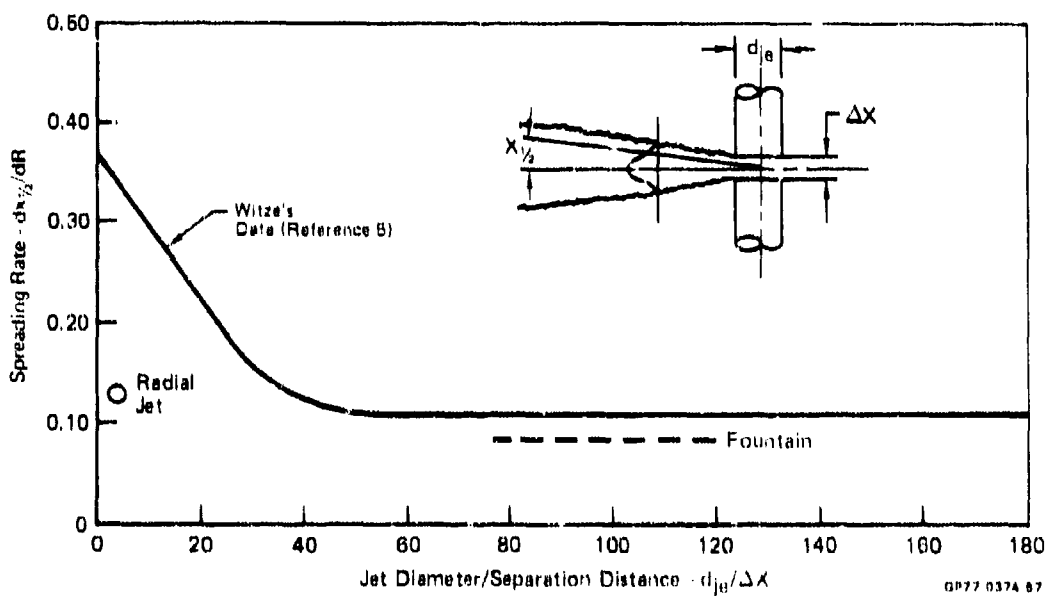


FIGURE 49
SPREADING RATE FOR FOUNTAIN, MCAIR RADIAL JET DATA, AND
RADIAL JETS TESTED BY WITZE

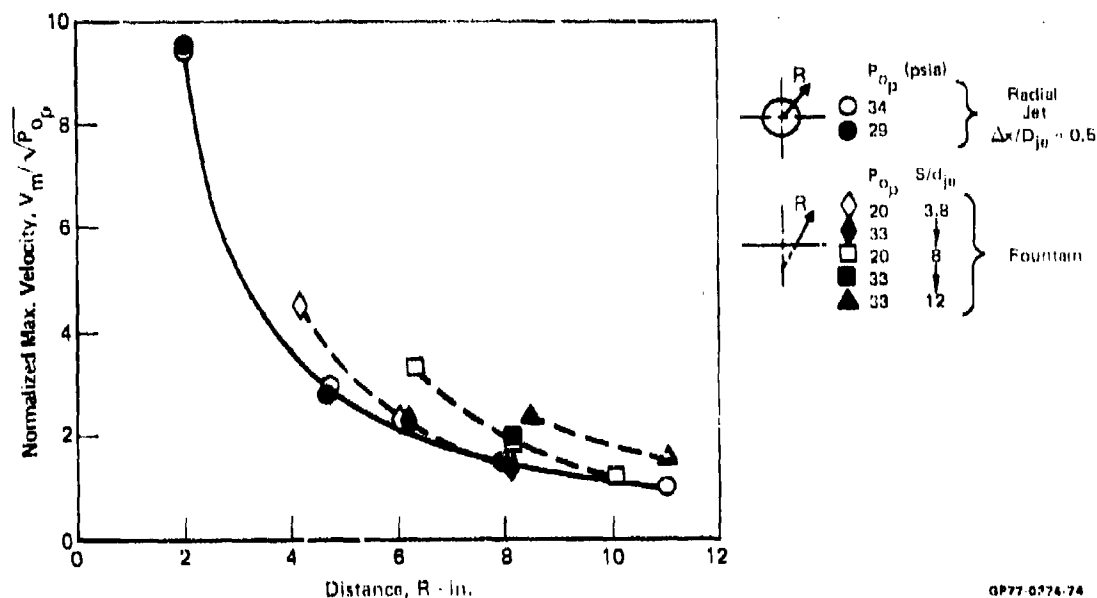


FIGURE 50
PEAK VELOCITY IN A FOUNTAIN, AND A SINGLE RADIAL JET

Summarizing the conclusions reached from an analysis of the fountain and radial jet data:

1. The flow in a symmetric two-jet fountain may be regarded as a radial flow from a virtual origin located below the ground plane.
2. At constant radius from the virtual origin, the fountain velocity profiles are approximately equal at angles of 0° and 20° from the vertical, but higher at 40° off the vertical. This result, however, is inconclusive because of possible asymmetries in the jet nozzles.
3. Fountain velocity distributions are self-similar, and the shape is in good agreement with that for a radial jet.
4. Fountain spreading rate is independent of the jet spacing S , and is in good agreement with that measured in Reference 8 for "constrained" radial jets.
5. Fountain velocity decay is in reasonable agreement with that for a radial jet, but the diameter of the equivalent annular nozzle used to generate a radial jet may depend on the spacing S .

In spite of some remaining uncertainties, the analogy between a symmetric two-jet fountain and an axisymmetric constrained radial jet has been substantiated by the data. The analogy permits a definition of the fountain upwash flowfield and, as described in Section 6, leads to a method for predicting fountain impingement forces on the underside of an airframe. Some general conclusions regarding

the flow in three and four-jet symmetric fountains may also be drawn, and they are discussed in the next section.

5.2 Extension of Two-Jet Fountain Results to Three and Four-Jet Configurations

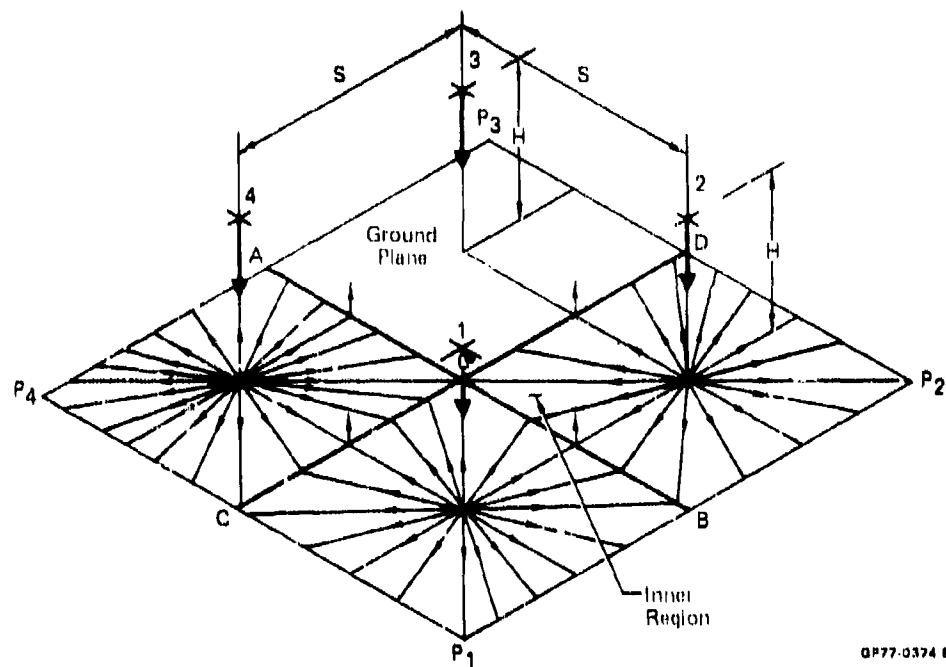
An idealization of the flow turning process when two equal axisymmetric wall-jets meet to form a fountain has led to an analogy between the fountain and a radial flow. This equivalence has been substantiated by experiment. The same idealized flow turning process will now be used to deduce fountain configurations for arrangements of three and four perpendicular jets of equal thrust. Because of its greater simplicity, a square arrangement of four jets will be discussed first.

Figure 51 is an idealized sketch of the ground impingement process for four equal vertical jets at equal heights H from the ground plane. Along each of the lines OA, OB, OC, and OD in Figure 51, the wall-jets are turned such that the angle θ defined in Figure 42 is preserved. Therefore, the fountain segments generated above each of these separation lines are radial flows. Unlike the two-jet case, however, these radial flows along vertical planes will impinge upon each other in the neighborhood of the vertical line through the point O. The radial flows are turned once again in this region, and a central fountain is formed whose flow direction is expected to be primarily vertical. Examination of Figure 51 shows that only a sector of the wall-jets generated by jets 1 and 2 will contribute to the fountain segment above the line OB. The rest will contribute to the segments formed above the lines OC and OD. The analogy between the four-jet fountain and radial jets may then be formulated as indicated in Figure 52. The ground plane is "cut" along the diagonals OP_1 , OP_2 , OP_3 , and OP_4 , and then folded along the lines OA, OB, OC, and OD, such that four radial jets are formed with origins at a distance $(S/2)$ below the ground plane. Note that for each radial jet, only the sector

$$\frac{\pi}{4} \leq \theta \leq \frac{3\pi}{4}$$

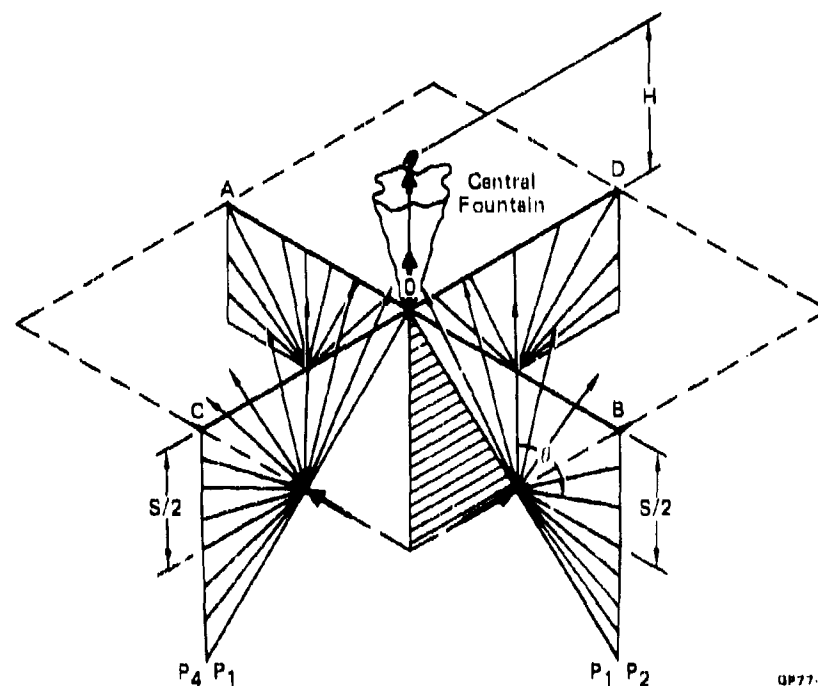
is relevant. Indeed, only the sector $(\frac{\pi}{4} \leq \theta \leq \frac{3\pi}{4})$ will contribute to a vertical fountain force. The four radial jets coalesce at point O, forming the central fountain. A flow pattern such as that indicated in Figure 52 may be generated by four pairs of opposing axisymmetric jets, provided that the radial jets are prevented from mixing until the point O is reached.

Figure 53 shows the impingement points for a rectangular arrangement of four perpendicular jets of equal thrust. The equivalent arrangement of radial jets would in this case be developed by once again "cutting" the ground plane



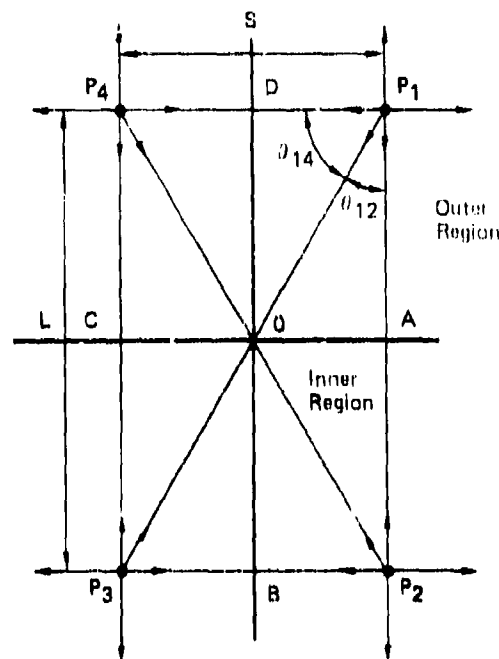
QP77-0374 81

FIGURE 51
IDEALIZED WALL JETS - FOUR SYMMETRIC JETS



QP77-0374 82

FIGURE 52
EQUIVALENCE BETWEEN FOUR-JET
FOUNTAIN AND SECTORS OF FOUR RADIAL JETS



P_n : Impingement Points

$$\theta_{12} = \tan^{-1} (S/L)$$

$$\theta_{14} = \frac{\pi}{2} - \theta_{12}$$

DP77-0374-13

FIGURE 53

RECTANGULAR ARRANGEMENT OF FOUR EQUAL, PERPENDICULAR JETS

along diagonals OP_1 , OP_2 , OP_3 and OP_4 ; and then folding the plane along symmetry lines OA, OB, OC, and OD. The virtual origins for the OA and OC fountain segments now lie at a distance $(L/2)$ below the ground plane, and the origins for fountain segments OB and OD are located at $(S/2)$ below the ground plane. The relevant radial jet sectors will now be:

$$\text{Fountain segments OA and OC: } 0_{12} \leq \theta \leq \frac{\pi}{2}$$

$$\text{Fountain segments OB and OD: } 0_{14} \leq \theta \leq \frac{\pi}{2}$$

$$\text{where } 0_{12} = \tan^{-1} (S/L)$$

$$0_{14} = \frac{\pi}{2} - 0_{12}$$

Figure 54 depicts the idealized flow pattern for three equal perpendicular jets in an isosceles triangle arrangement. Three fountain segments are generated in this case: OA, OB, and OC. Because of symmetry, the fountain segments lie along the perpendicular bisectors of the triangle sides. The virtual origin for the fountain segment OB is located at a distance $(S/2)$ below the ground plane, and the virtual origins for segments OA and OC are located at $(L/2)$ below the ground plane. The equivalent radial jets are now made up by three pairs of

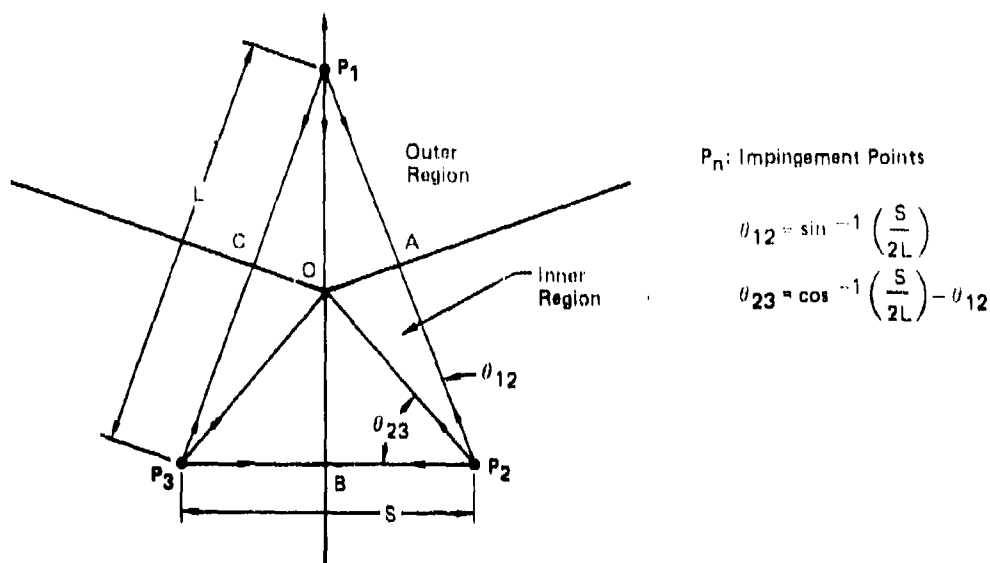


FIGURE 54
ISOSCELES TRIANGULAR ARRANGEMENT OF THREE EQUAL,
PERPENDICULAR JETS

QP77-0374-14

opposed jets, with each pair centered about each of the virtual origins. The relevant radial jet sectors are:

Fountain segments OA and OC: $\theta_{12} \leq \theta \leq \frac{\pi}{2}$

Fountain segment OB: $\theta_{23} \leq \theta \leq \frac{\pi}{2}$

where from the geometry in Figure 54:

$$\theta_{12} = \sin^{-1} \left(\frac{S}{2L} \right)$$

$$\theta_{23} = \cos^{-1} \left(\frac{S}{2L} \right) - \theta_{12}$$

As in the four-jet arrangements, a central fountain is formed above point O, where the three fountain segments impinge on each other.

Using the equivalence between fountain segments and radial jets, it is possible to compute the vertical momentum flux for various jet arrangements. This will be done in the next subsection.

5.3 Normal Momentum Flux in Fountains

The fountain impingement force on the underside of an airframe is related

to the total vertical momentum flux in the fountain flow, and calculation of this momentum flux provides a measure of the maximum fountain impingement force available for a particular jet arrangement. The fountain velocity is not vertical, so it is important to take into account the momentum flux components. The analogy between fountain and single radial jets, or combinations of radial jets, permits calculation of these components.

As discussed in previous sections, symmetrical two-jet fountains have been replaced by equivalent radial jets. Fountains for configurations with three and four perpendicular jets of equal thrust have been divided into segments and each segment related to the flow from an appropriate sector of a radial jet. Some of the fountain segments contain portions of a central fountain, which has been taken to be equivalent to the flow generated by the impingement of the various radial jet sectors. Given a group of two to four vertical jets, the calculation of the resultant fountain vertical momentum flux requires the following information:

1. A relation between the momentum flux of the vertical jets and wall-jets which generate the fountain, and the radial jets which have replaced the fountain.
2. Calculation of the vertical momentum flux for the various radial jet sectors which make up the fountain, and for any central fountain which may have been created by the impingement of these sectors.

Item 1 is discussed below, and Item 2 is the following subsection.

It has been shown that when a circular jet impinges at 90° to a ground plane, the total momentum flux is conserved, and at the boundary of the "impingement zone" in Figure 12, the total momentum flux per unit azimuthal angle in the wall-jet is equal to the total momentum flux per unit angle in the free-jet. Furthermore, it has been shown in Section 2.3.3 that as the wall-jets develop, the total momentum flux per unit angle remains unchanged, indicating that the viscous shear stress on the ground plane does not significantly affect the wall-jet development. It will now be assumed that when two axisymmetric wall-jets impinge upon each other and form a fountain, the total momentum flux per unit angle is also conserved in the turning process. Since the fountain combines the momentum from the wall jets on each side of it, the total momentum flux per unit angle in the fountain will be equal to twice the momentum flux per unit angle in a single wall jet. Since the fountain and equivalent radial jet have the same momentum flux, it follows (see Figure 42) that if

$$\dot{M}_{f1} = \dot{M}_{f2}$$

denote the momentum fluxes in the vertical jets, then

$$\dot{M}_{JR} = 2\dot{M}_J \text{ or } 2$$

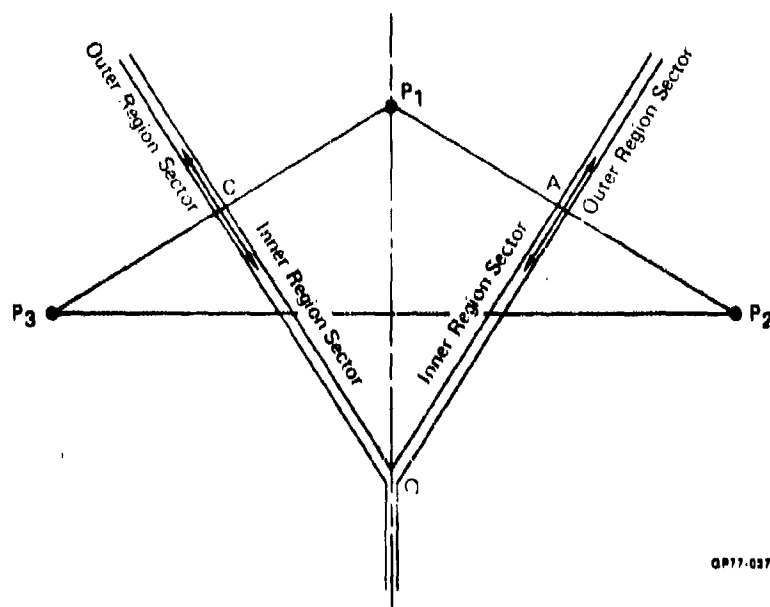
where \dot{M}_{JR} denotes the total momentum flux in the radial jet which replaces the fountain. The flow in a fountain segment is in the radial direction about the segment's virtual origin, so the available vertical momentum flux is only a fraction of the total segment's momentum flux. The magnitude of this fraction will be computed in the following subsection.

5.3.1 Ideal Normal Momentum Flux in a Fountain Segment - In Figures 51, 53, and 54, the wall-jet's flowfield has been subdivided into an inner region and an outer region. The boundary between these is the polygon constructed by connecting the jet impingement points. Since the jets are all perpendicular and of equal thrust, each fountain segment will form along the perpendicular bisector of each side of the polygon. Thus, one part of the fountain segment lies at least partially in the inner region, and is denoted the "inner region sector." The rest of the segment lies in the outer region and is correspondingly called the "outer region sector." The inner region sectors from different jet pairs will intersect to form one or more central fountains.

The jet arrangements will now be restricted to cases where all inner region sectors intersect within the inner region. The geometries in Figures 51, 53, and 54 all satisfy this condition.* Figure 55 shows a case where this is not so.

At central fountains, the radial jets simulating the various segments impinge on each other. The vertical momentum flux across a plane parallel to the ground, located a distance z above the ground, will partly come from undisturbed portions of the radial jets, and partly from the central fountain or fountains. However, for central fountains which lie within the inner region, examination of Figures 51 and 52 will reveal that there is no vertical momentum flux through the lateral area of the inner region. Consequently, the total vertical momentum flux across planes parallel to the ground plane is independent of z , and can therefore be computed at $z = 0$. That is, where the ground plane was located. At the plane $z = 0$, it is assumed that the central fountain has not yet formed, and consequently the vertical momentum flux in the region may be calculated from the momentum distribution for the individual radial jet sectors.

* This is not a serious restriction, since most practical designs would seek to maximize the fountain's impingement force by locating the central fountain within the inner region, where it will usually impact on a greater aircraft planform area.



QR77-0374-15

FIGURE 55
ISOSCELES TRIANGULAR ARRANGEMENT OF THREE EQUAL JETS WITH
FOUNTAIN SEGMENTS INTERSECTING OUTSIDE THE INNER REGION

Figure 56 shows the wall jets and equivalent radial jet sectors for one segment of a multiple-jet fountain. The fountain vertical momentum in the inner region sector is calculated by computing the vertical momentum flux in the radial jet sector subtended by the line OA in Figure 56b. The fountain vertical momentum in the outer region is calculated by computing the vertical momentum flux in the radial jet sector subtended by a finite value of y , and then letting y approach infinity. The characteristics of constrained radial jets described in Reference 58 will be used to calculate the vertical momentum in the fountain sector. For a strip of width dy , the momentum flux in the z -direction is given by

$$dM_z = \int_{-\infty}^{+\infty} \rho w^2 dx dy \quad (69)$$

where w is the radial jet velocity in the z -direction

$$w = V_R \cos \theta$$

where V_R is the radial jet velocity in the R direction. Equation (69) may then be written as

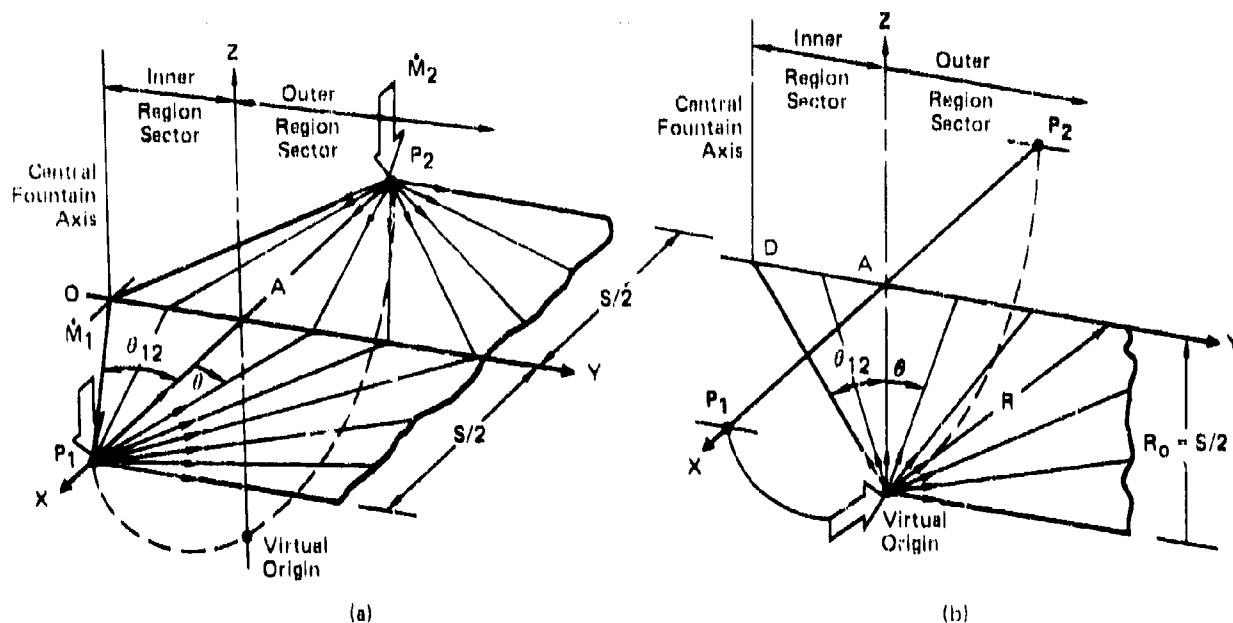


FIGURE 56
WALL JETS AND EQUIVALENT RADIAL JET FOR A FOUNTAIN SEGMENT

GP77-0374-16

$$d\dot{M}_z = \cos^2 \theta \int_{-\infty}^{+\infty} \rho V_R^2 dx dy. \quad (70)$$

From total momentum conservation in the radial jet

$$\dot{M}_{jR} = 2\pi R \int_{-\infty}^{+\infty} \rho V_R^2 dx, \quad R > R_j \quad (71)$$

where, as before, \dot{M}_{jR} is the total momentum flux through the radial jet's annular nozzle (of radius R_j).

Consequently, Equation (70) may be written as:

$$d\dot{M}_z = \frac{\dot{M}_{jR}}{2\pi} \frac{\cos^2 \theta}{R} dy$$

since

$$y = R_0 \tan \theta,$$

and

$$R_0/R = \cos \theta,$$

the total vertical momentum flux becomes simply

$$\dot{M}_z = \frac{\dot{M}_{JR}}{2\pi} \int_{\theta_0}^{\theta_f} \cos \theta \, d\theta$$

or

$$\dot{M}_z = \frac{\dot{M}_{JR}}{2\pi} [\sin \theta_f - \sin \theta_0] \quad (72)$$

where θ_0 and θ_f denote the initial and final limits of integration, respectively. Referring to Figure 56, in the limit

$$y \rightarrow \infty ; \quad \theta_f \rightarrow \frac{\pi}{2}.$$

So, for the total sector, the vertical momentum flux is

$$\dot{M}_z = \frac{\dot{M}_{JR}}{2\pi} [1 + \sin \theta_{12}] \quad (73)$$

where θ_{12} is positive

The simple result in Equation (73) may be used to calculate the ideal vertical momentum flux for the combination of radial jet sectors which make up multiple-jet fountains.

5.3.2 Ideal Momentum Fluxes for Two, Three, and Four-Jet Fountains, and Optimum Arrangements of Three and Four-Jet Fountains - For a two-jet fountain, the angle θ_{12} in Figure 56 is $\pi/2$, and Equation (73), then yields

$$\dot{M}_z = \frac{\dot{M}_{JR}}{\pi}$$

and since, as shown before,

$$\dot{M}_{JR} = 2\dot{M}_j$$

where \dot{M}_j denotes the momentum flux for each one of the two jets, it follows that the ideal fountain momentum flux divided by the total jet thrust will be

$$\frac{\dot{M}_z}{2\dot{M}_j} = \frac{1}{\pi}. \quad (74)$$

An "optimum" three or four-jet fountain arrangement is considered to be

one for which the total fountain vertical momentum is a maximum. The conditions under which this occurs will be derived.

Considering first the isosceles triangular arrangement in Figure 54 and summing the radial jet sector contributions using Equation (73):

$$\dot{M}_Z = \frac{\dot{M}_J R_{12}}{2\pi} [\sin \theta_{12} + 1] + \frac{\dot{M}_J R_{23}}{2\pi} [\sin \theta_{23} + 1] + \frac{\dot{M}_J R_{31}}{2\pi} [\sin \theta_{31} + 1] \quad (75)$$

now

$$\dot{M}_{JR_{12}} = \dot{M}_{JR_{31}} = 2\dot{M}_J$$

and

$$\dot{M}_{JR_{23}} = 2\dot{M}_J$$

where \dot{M}_J is the momentum flux for a single vertical jet; and also,

$$\theta_{12} = \theta_{31}.$$

Equation (75) then becomes

$$\dot{M}_Z = \frac{\dot{M}_J}{\pi} \left[2 [\sin \theta_{12} + 1] + \sin \theta_{23} + 1 \right],$$

and dividing by the total vertical jet momentum:

$$\frac{\dot{M}_Z}{3\dot{M}_J} = \frac{1}{3\pi} \left[2 \sin \theta_{12} + \sin \theta_{23} + 3 \right]. \quad (76)$$

From the expressions for θ_{12} and θ_{23} included in Figure 54, these angles depend on the ratio (S/L) . Differentiating Equation (76) with respect to (S/L) and setting the result equal to zero leads to:

$$[2 \cos \theta_{12} - \cos \theta_{23}] \frac{d}{d(S/L)} [\sin^{-1} (\frac{S}{2L})] + \cos \theta_{23} \frac{d}{d(S/L)} [\cos^{-1} (\frac{S}{2L})] = 0.$$

Expanding the derivatives leads to the result that

$$\theta_{12} = \theta_{23}.$$

showing that the maximum ideal fountain momentum flux is achieved when the jets are arranged in an equilateral pattern.

Considering the rectangular jet arrangement shown in Figure 53 and summing the radial jet sector contributions using Equation (73), the total vertical momentum flux in the fountain becomes

$$\dot{M}_z = \frac{\dot{M}_{JR12}}{\pi} [\sin \theta_{12} + 1] + \frac{\dot{M}_{JR14}}{\pi} [\sin \theta_{14} + 1],$$

where geometrical symmetry has been taken into account.

Using the relation between radial and vertical jet momentum fluxes, the above may be written as:

$$\dot{M}_z = \frac{2}{\pi} \dot{M}_j [\sin \theta_{12} + \sin \theta_{14} + 2].$$

Dividing again by the total momentum flux of the vertical jets

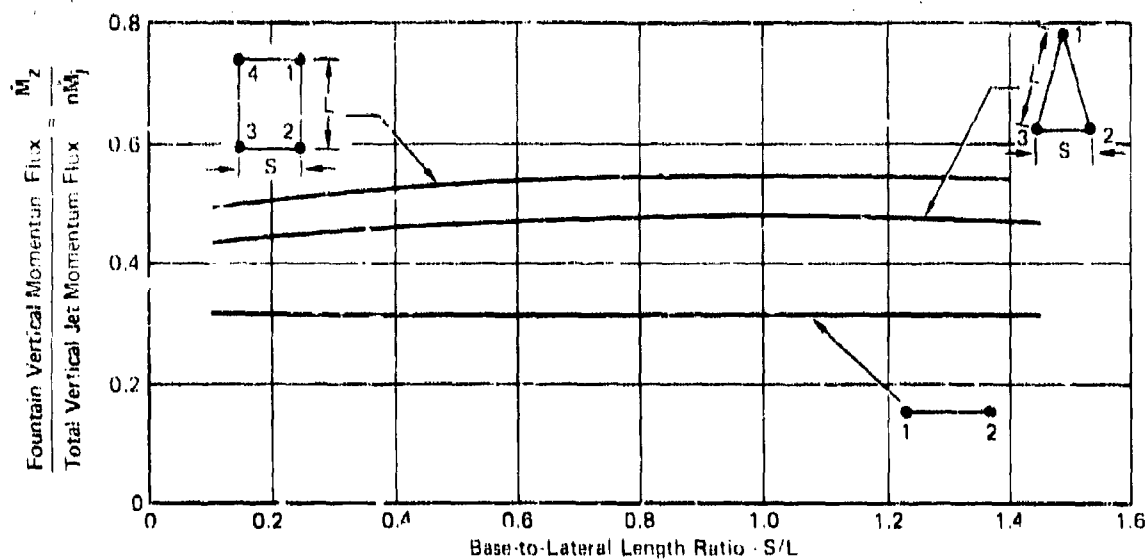
$$\frac{\dot{M}_z}{4\dot{M}_j} = \frac{1}{2\pi} [\sin \theta_{12} + \sin \theta_{14} + 2]. \quad (77)$$

By finding the maximum value of this function, it is possible to show that the maximum ideal fountain vertical momentum flux is achieved when the jets are arranged in a square pattern.

Figure 57 shows the ratio of ideal fountain vertical momentum flux to total jet momentum flux, plotted against S/L , for two, three, and four-jet fountains. The figure indicates that the variation with (S/L) is very weak, so that configurations which differ from the optimum equilateral triangular, or quadrilateral square patterns will experience a very small reduction in fountain vertical momentum flux.

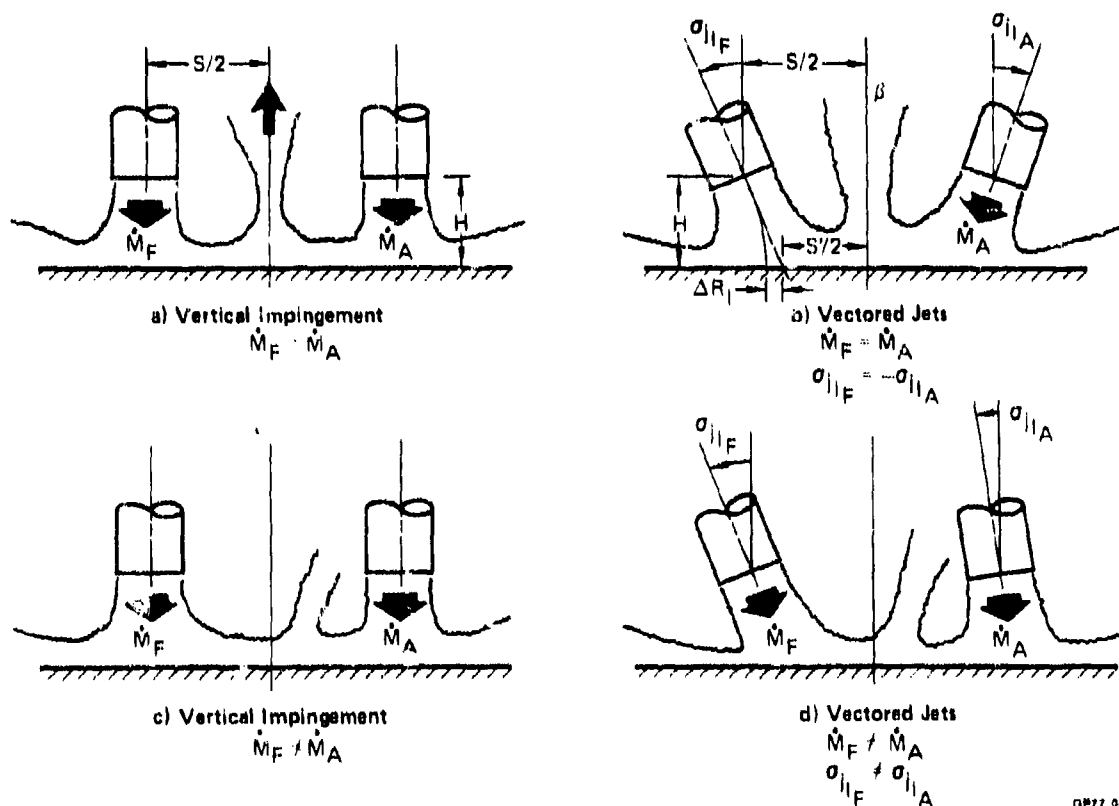
5.4 Asymmetric Two-Jet Fountains

The description of two-jet fountain flowfields has so far been confined to cases in which the two jets that generate the fountains are perpendicular and have equal thrust. In Figure 58, this simplest jet arrangement is labeled "configuration A." A more complicated situation arises for configuration B, in which the jets are vectored as mirror images, while their thrusts are still kept equal. The flow-field is still symmetric about the plane β , and consequently the fountain remains planar and the fountain velocity profile is symmetric about β . The discussion of



GP77-0483-49

FIGURE 57
NORMALIZED IDEAL FOUNTAIN VERTICAL MOMENTUM FLUX
FOR TWO, THREE, AND FOUR-JET FOUNTAINS



GP77-0483-50

FIGURE 58
TWO-JET FOUNTAIN CONFIGURATION

oblique jet impingement in Section 2.2.3 has indicated that the free jet impingement stagnation point on the ground plane is displaced from the projected jet axis by a distance AR_I . Thus, the minimum distance between the jet impingement point and the symmetry plane β is given by

$$S'/2 = S/2 - H \tan \sigma_{jI} + AR_I.$$

If it is once again assumed that in forming the fountain, the wall-jets are turned as if they were "folded" along the intersection between the plane β and the ground plane, it follows that for configuration B the fountain flow is analogous to a radial flow emanating from a virtual origin located at a distance $S'/2$ below the ground plane. Due to the asymmetric momentum distribution in the wall-jet, however, the azimuthal momentum distribution in this fountain will differ from that for configuration A. Assuming momentum conservation in the turning process, the azimuthal momentum distribution in the fountain may be calculated from the known momentum distribution in the wall-jets.

In Figure 58 configurations C and D are no longer symmetric, so that the fountains no longer lie on a plane. Due to a lack of data, it is impossible to specify the fountain flowfield with any certainty in these cases, but a qualitative picture of the fountain geometry has been established. For configuration C, the "separation surface" (analogous to the plane β) is postulated to be conical with the cone apex located below the ground plane. Figure 59 depicts the conical separation surface originating from a hyperbolic ground separation line. The cone semi-apex angle is denoted by α_0 , and the cone apex lies on the z axis, at a distance z_0 below the origin. The fountain flow would then be conical, with streamlines radiating from a virtual origin at the cone apex. A conical separation surface has several properties which make it plausible:

1. The intersection of the cone and ground plane is a hyperbola, and it will be shown that this is compatible with the separation lines calculated in Section 3.2.2.
2. With the fountain velocity vectors located approximately along generatrices of the cone, the fountain streamlines are straight. This is consistent with a constant pressure, free turbulent flow.
3. As the jet momenta \dot{M}_F and \dot{M}_A become equal, the cone semi-apex angle can approach $\pi/2$, and the planar radial flow postulated for configuration A is recovered.

Section 3.2.2 has described calculations of the wall-jet separation lines for a pair of vertical jets operating at different thrusts. Results of these

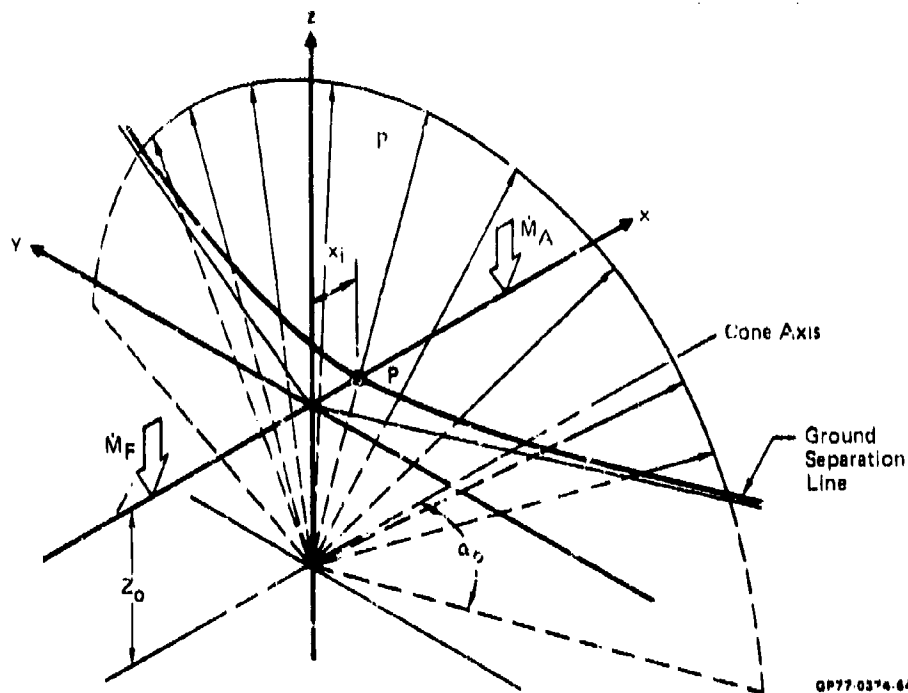


FIGURE 59
FOUNTAIN GEOMETRY FOR PERPENDICULAR JETS OF UNEQUAL THRUST

calculations have been used to obtain an expression for the asymptotic angle of a hyperbolic fit to the separation lines, and thus to the conical fountain's semi-apex angle. The points in Figure 60a indicate the asymptotic angles measured from the exact numerical results. The dotted line in the same Figure shows that the points are closely approximated by the expression

$$\tan \alpha_0 = \frac{(1.56) (\dot{M}_A / \dot{M}_F)^{1/2}}{1 - (\dot{M}_A / \dot{M}_F)} \quad (78)$$

The location of the cone apex z_0 may be obtained from the location of the separation point P on the x axis of Figure 59. From the stagnation line equations it may be shown that for two perpendicular jets:

$$\bar{x}_1 = \frac{1 - (\dot{M}_A / \dot{M}_F)}{1 + (\dot{M}_A / \dot{M}_F)} \quad (79)$$

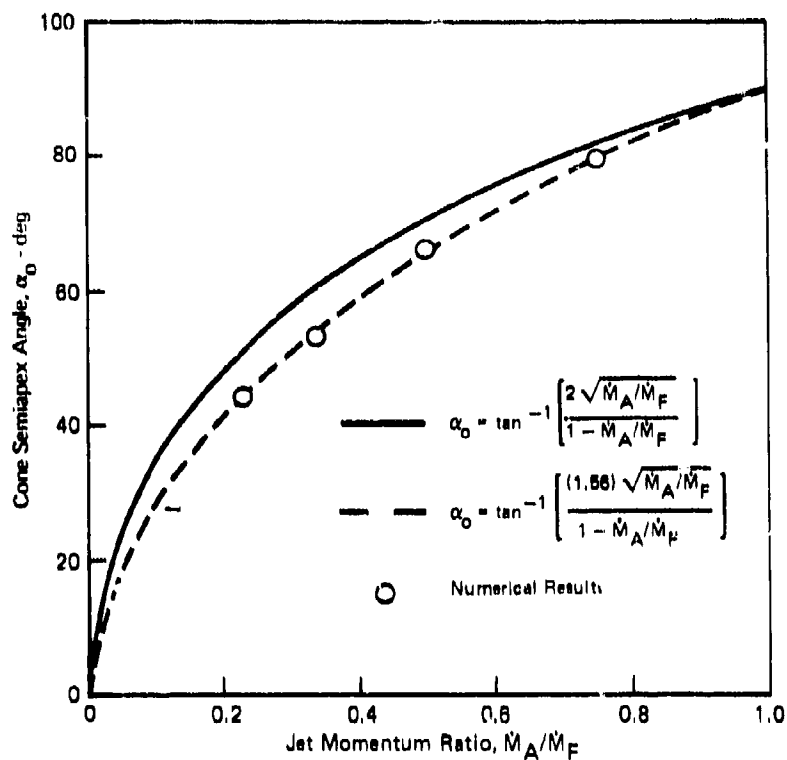


FIGURE 60a
CONICAL FOUNTAIN SEMIAPEX ANGLES AS A FUNCTION OF
JET MOMENTUM RATIO

where

$$\bar{x}_1 = 2x_1/S.$$

From the geometry of Figure 59

$$\bar{z}_0 = -\bar{x}_1 \tan \alpha_0$$

where a bar again denotes normalization by $(S/2)$, and using Equations (78) and (79)

$$\bar{z}_0 = - \frac{(1.56) (\dot{M}_A/\dot{M}_F)^{1/2}}{1 + (\dot{M}_A/\dot{M}_F)} \quad (80)$$

A plot of Equation (80) is shown by the dotted line in Figure 60b. Equation (80) does not approach the correct limit

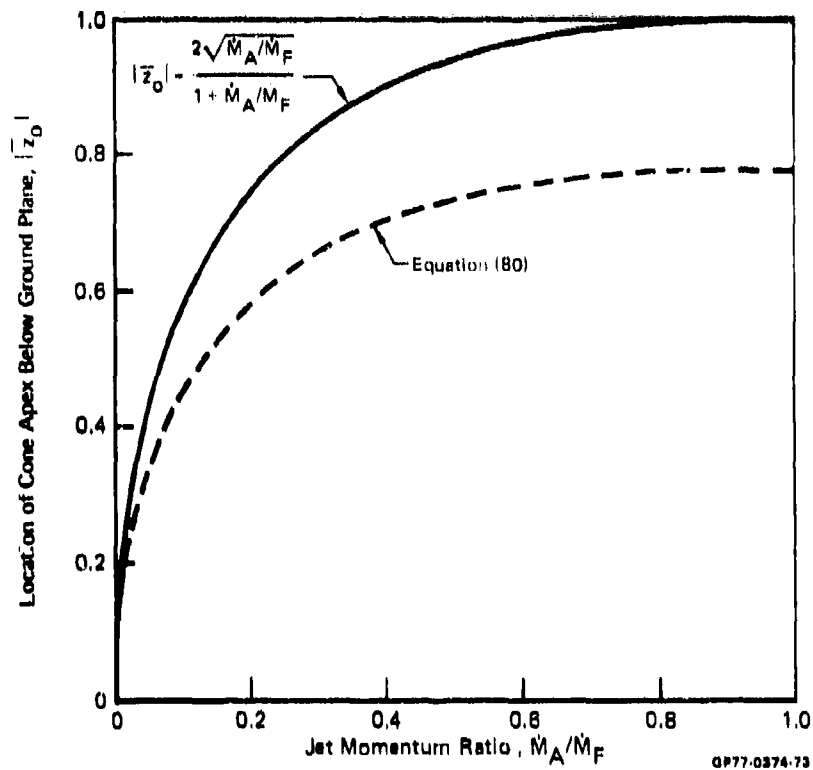


FIGURE 80b
CONICAL FOUNTAIN APEX LOCATION AS A FUNCTION OF
JET MOMENTUM RATIO

$$\bar{z}_0 \rightarrow -1$$

as

$$(\dot{M}_A/\dot{M}_F) \rightarrow 1.$$

Adjusting constants in Equations (78) and (79) so that this condition is satisfied yields the relations

$$\tan \alpha_0 = \frac{2 (\dot{M}_A/\dot{M}_F)^{1/2}}{1 - (\dot{M}_A/\dot{M}_F)} \quad (81)$$

$$\bar{z}_0 = -\frac{2 (\dot{M}_A/\dot{M}_F)^{1/2}}{1 + (\dot{M}_A/\dot{M}_F)} \quad (82)$$

Equations (81) and (82) are plotted as solid lines in Figures 60a and 60b respectively. For $(\dot{M}_A/\dot{M}_F) > 0.5$, Equation (81) still provides a good approximation to the computer program results. Equations for the complete stagnation line may now be written. Choosing the numerical constants for the correct limiting behavior as $(\dot{M}_A/\dot{M}_F) \rightarrow 1$, and for a good fit to the calculated results, the equations are:

$$\bar{y} = \frac{2 (\dot{M}_A/\dot{M}_F)^{1/2}}{1 - (\dot{M}_A/\dot{M}_F)} \left\{ \bar{x}^2 - \left[\frac{1 - (\dot{M}_A/\dot{M}_F)}{1 + (\dot{M}_A/\dot{M}_F)} \right]^2 \right\}^{1/2} \quad (83)$$

$$\text{for} \quad 0.5 \leq (\dot{M}_A/\dot{M}_F) < 1$$

$$\text{and} \quad \bar{y} = \frac{(1.56) (\dot{M}_A/\dot{M}_F)^{1/2}}{1 - (\dot{M}_A/\dot{M}_F)} \left\{ \bar{x}^2 - \left[\frac{1 - (\dot{M}_A/\dot{M}_F)}{1 + (\dot{M}_A/\dot{M}_F)} \right]^2 \right\}^{1/2} \quad (84)$$

$$\text{for} \quad 0 < (\dot{M}_A/\dot{M}_F) \leq 0.5.$$

These equations are compared to the computer program calculations in Figure 61.

The above discussion has provided a plausible qualitative description of the fountain geometry for the case of two jets of different thrust impinging perpendicularly to a ground plane. In order to compute the force generated by such an asymmetric fountain on an airframe, data on fountain velocity profiles and spreading rates are required. This information is not currently available. Indeed, the whole description of this asymmetric fountain geometry is speculative at present, and requires experimental verification. When the jets have different thrust and are vectored at different angles (configuration D in Figure 58) the picture is complicated still further. It may still be possible to postulate a conical fountain flow for which conditions vary for each meridional angle. The overall fountain geometry might still be obtained by adjusting cone parameters to fit calculated or measured values of the fountain separation line.

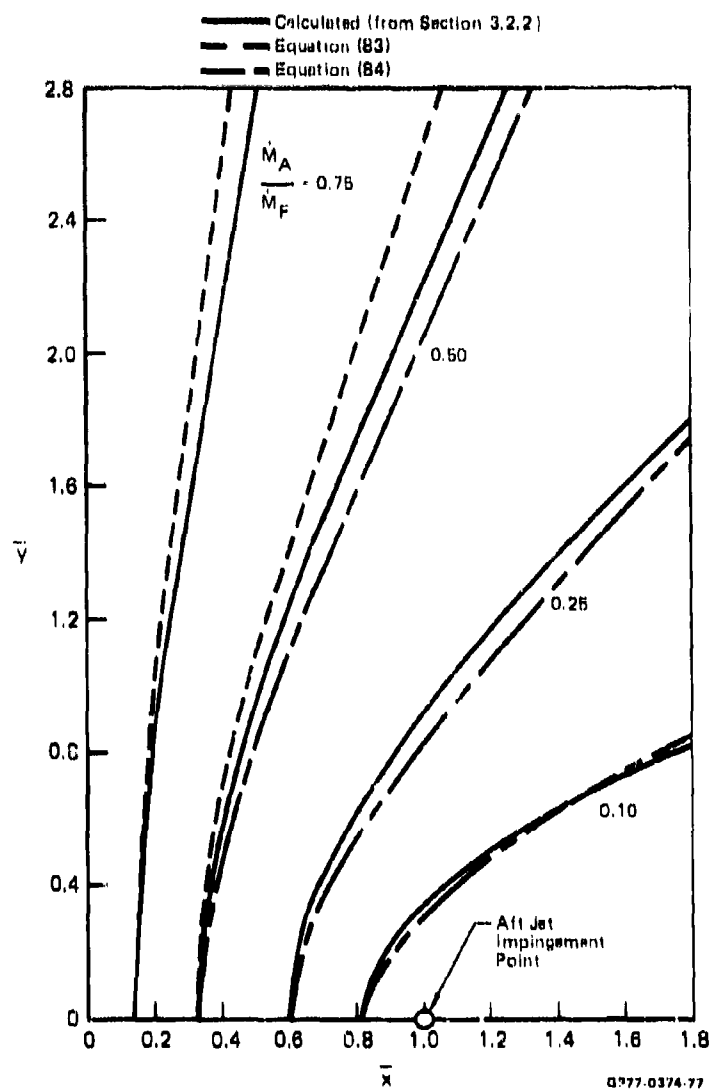


FIGURE 81
 APPROXIMATION TO CALCULATED STAGNATION LINES BY HYPERBOLAS

6. FOUNTAIN IMPINGEMENT ON A FUSELAGE-WING

A description of the fountain flowfields generated by two to four circular, vertical jets of equal thrust impinging on a ground plane has been given in Section 5. The total, ideal vertical momentum flux generated in such fountains has also been calculated. This section describes how this vertical momentum flux is converted into a positive normal force when a fountain strikes the airframe undersurface. It has also been found that in addition to this positive impingement force, the fountain induces a negative suckdown force. This force is to be added to the suckdown forces generated by the free-jets and wall-jets, and it is related to the fountain entrainment. An approximate method to account for the fountain suckdown force has been derived, and is also described in this Section.

In a parallel MCAIR IRAD effort, (Reference 23), an apparatus to simulate two and four-jet fountain configurations was designed and fabricated. The forces produced on a representative aircraft configuration by these simulated fountains were measured. The experimental forces have been compared to the sum of predicted fountain impingement and suckdown forces, and the results are described in this Section.

6.1 Two-Jet Fountain Impingement and Suckdown

In Section 5, the flow in the fountain produced by two circular, vertical jets of equal thrust has been shown to be approximately equivalent to the flow in a constrained radial jet. This analogy will be used to calculate the pressures induced by fountain impingement, and the terms "two-jet fountain" and "radial jet" will be used interchangeably. Based on available data on the pressures generated by the impingement of two axisymmetric wall jets, a simple relationship between local jet dynamic pressure and the pressure generated on the surface upon which the jet impacts has been obtained. This relationship is used to calculate the force generated by the radial jet impingement on an airframe undersurface. The calculation of two-jet fountain suckdown forces is also discussed in this subsection. The simpler case of suckdown produced by a radial jet impinging on a rectangular wing is discussed first, and the more complex case of a trapezoidal wing is discussed later.

6.1.1 Fountain Impingement Force - The constrained radial jet used to represent the two-jet fountain is an axisymmetric, turbulent flow which spreads out from an annular nozzle and whose width grows linearly with distance from the nozzle radius (See Reference 8 and Figure 48). Referring to Figures 42 and 43, the analogy between radial jet and fountain implies that the radial jet development on each side of the symmetry plane is approximately equivalent to that of the corresponding wall jets which merge to form the fountain. It has been postulated (and experimentally confirmed) that when the wall-jets turn to form the fountain, the velocity components normal to the plane of symmetry are rotated 90° , and the tangential components are unchanged.

(See the enlarged sketch in Figure 42). It is postulated that the same turning process occurs when the radial jet impinges on the underside of an aircraft planform. Figure 62 depicts the impingement of a radial jet on a rectangular plate, for a completely symmetrical situation. The sectors of the radial jet which do not impinge on the plate are assumed to remain undisturbed. The deflected sector is first split along the line IL, and then deflected such that the local angle θ as defined in Figure 62 is preserved in the turning process. The direction of the flow along the plate undersurface would then be as indicated in the Figure.

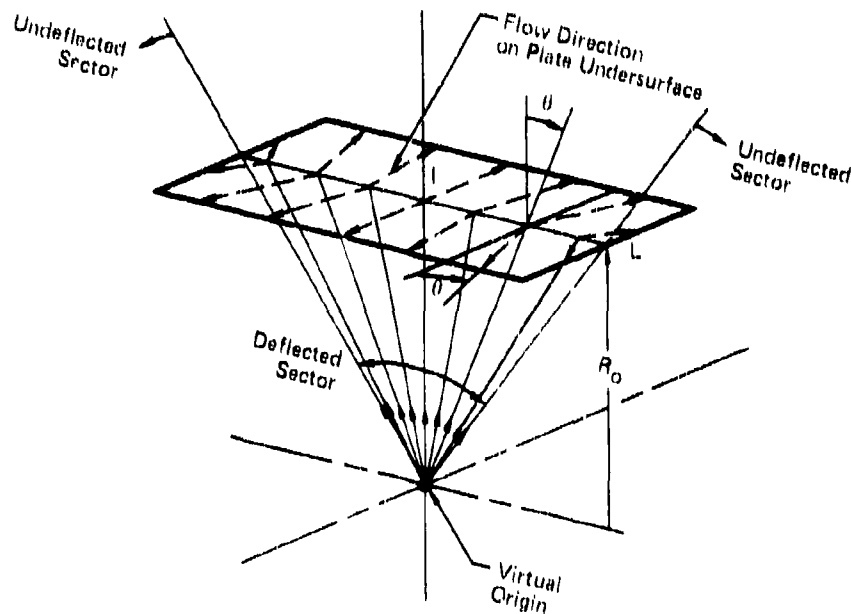


FIGURE 62
IDEALIZED RADIAL JET SPLITTING AND TURNING UPON
IMPINGEMENT ON A RECTANGULAR PLATE

QP77-0374-80

6.1.1.1 Pressures Generated by Axisymmetric Wall-Jets Impinging on Each Other -

It has been assumed above that the turning process when two wall-jets meet at a plane of symmetry to form a fountain is the same as that when each half of a radial jet encounters the underside of an aircraft planform. Consequently, pressure data obtained for the former case can be used to derive an expression for calculating pressures in the latter case. For a symmetrical, two jet arrangement, Reference 24 contains measured pressure distributions along a line which corresponds to the intersection between the ground plane and the plane of symmetry (y axis in Figure 42). It has been possible to relate the measured pressures to the peak velocity which would exist at each point P in the wall-jet, if the jet continued as a free wall-jet.

The basic concept is that the pressure distribution caused by an impinging turbulent flow can be calculated from the undisturbed dynamic pressure normal to the surface. Thus, the peak pressures generated when two wall-jets impinge on each other are related to the peak dynamic pressures on the wall-jet profiles.

Referring once again to Figure 42, the wall-jets develop along the ground plane at essentially constant static pressure, outside of regions in the immediate neighborhood of the impingement points 1 and 2. Near the (y, z) plane of symmetry, the wall-jets turn and form the fountain. In this turning process, the pressure on the ground plane increases, since the wall-jet flows are retarded. The pressure reaches its maximum value along the y axis, and this maximum may be calculated by relating it to the peak velocity in the wall-jet profile, $U_m(r)$. Results in References 7 and 8 indicate that for normal impingement of a round jet on a plane, the peak velocity in the axisymmetric wall jet far from the impingement point may be calculated from:

$$\left(\frac{U_m}{V_{je}} \right) \left(\frac{H}{R_{je}} \right) = (1.97) \left(\frac{r}{H} \right)^{-1} \quad (85)$$

where: V_{je} = jet exit velocity
 H = nozzle height above ground plane
 R_{je} = nozzle exit radius

This equation holds for an established wall-jet far from the impingement point.

At a point P along the y axis where the radial wall-jets interact (see Figure 42), it is postulated that the pressure is given by:

$$p_m - p_\infty = \frac{\rho}{2} U_m^2 \cos^2 \theta$$

or

$$C_p = \frac{p_m - p_\infty}{p_{oj} - p_\infty} = \frac{U_m^2}{V_{je}^2} \cos^2 \theta$$

Substituting Equation (85)

$$C_p = (1.97)^2 \left(\frac{R_{je}}{H} \right)^2 \left(\frac{r}{H} \right)^{-2} \cos^2 \theta$$

and since

$$\cos \theta = \frac{S}{2r}$$

and along the y axis

$$r = [y^2 + (S/2)^2]^{1/2}$$

this may be written in the form:

$$C_p = (1.97)^2 \frac{s^2 D_{je}^2}{[(2y)^2 + s^2]^2} \quad (86)$$

It must be noted that Equation (86) is independent of the nozzle height H . This conclusion is supported by the data of Reference 24. Figure 63 compares Equation (86) to the data of Reference 24 for four values of the nozzle spacing S/D_{je} . The agreement is very good, except for the case

$$S/D_{je} = 4.$$

In this instance, the nozzles are probably so close together that the wall-jet has not become fully established prior to the fountain formation.

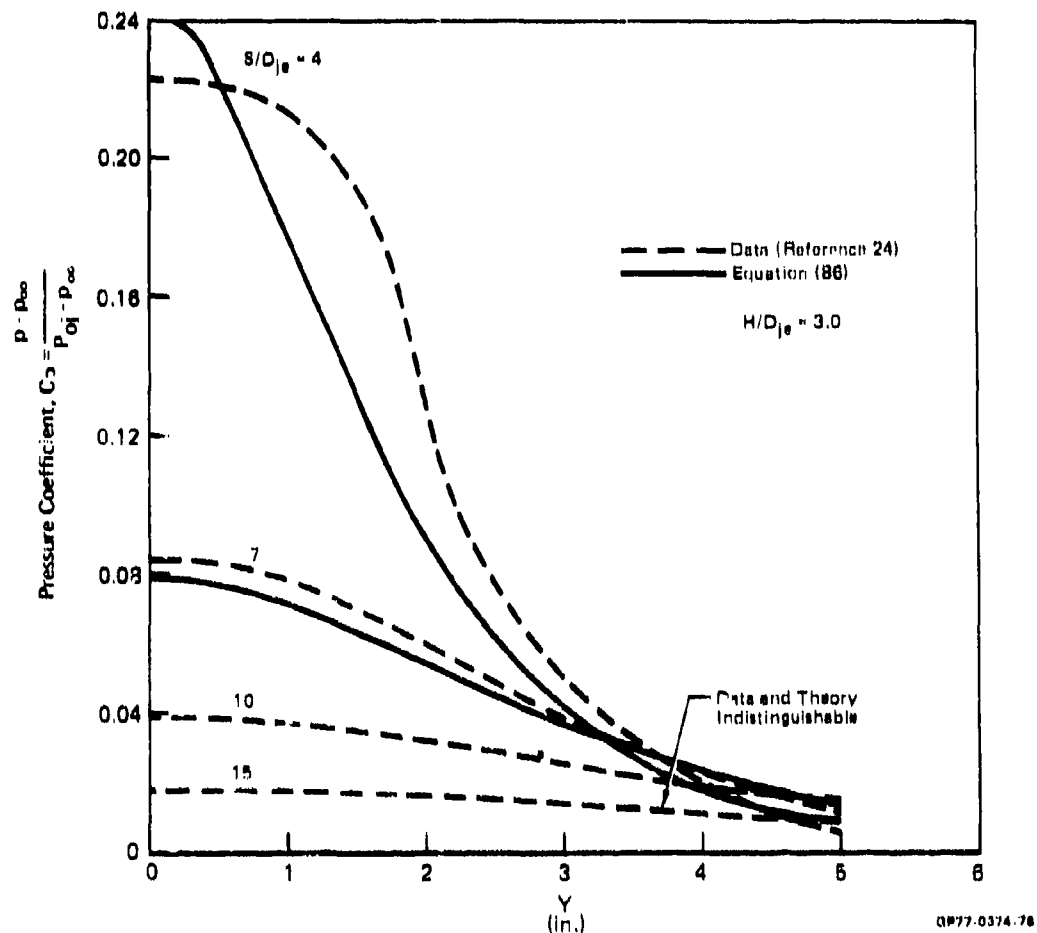


FIGURE 63
PEAK PRESSURE DISTRIBUTIONS BENEATH FOUNTAIN

The basic assumption that the peak pressure generated by the impingement of two radial wall jets is equal to the normal component of the maximum dynamic pressure in the wall jet has therefore been substantiated by the data.

6.1.1.2 Pressures Generated by Fountain Impingement on an Airframe Under-surface - Figure 64 illustrates a two-jet fountain, represented by a radial jet with origin at a distance R_0 below the indicated fuselage reference point, and with initial radius R_j . It is assumed that ambient pressure acts on the planform upper surface. It is further assumed that those portions of the annular jet which are not blocked by the planform are unaltered, and do not in any way affect the jet impingement force on the aircraft. The net force on a strip of width dy will then be:

$$dF_z = \left[\int_{x_T(y)}^{x_L(y)} (p - p_\infty) dx \right] dy$$

where x_L and x_T denote the upper and lower limits of integration. Replacing the aircraft by its planform, and equating the pressure difference to the normal component of the jet dynamic pressure:

$$dF_z = \frac{\rho}{2} \left[\int_{x_T(y)}^{x_L(y)} (V_R^2 \cos^2 \theta) dx \right] dy \quad (87)$$

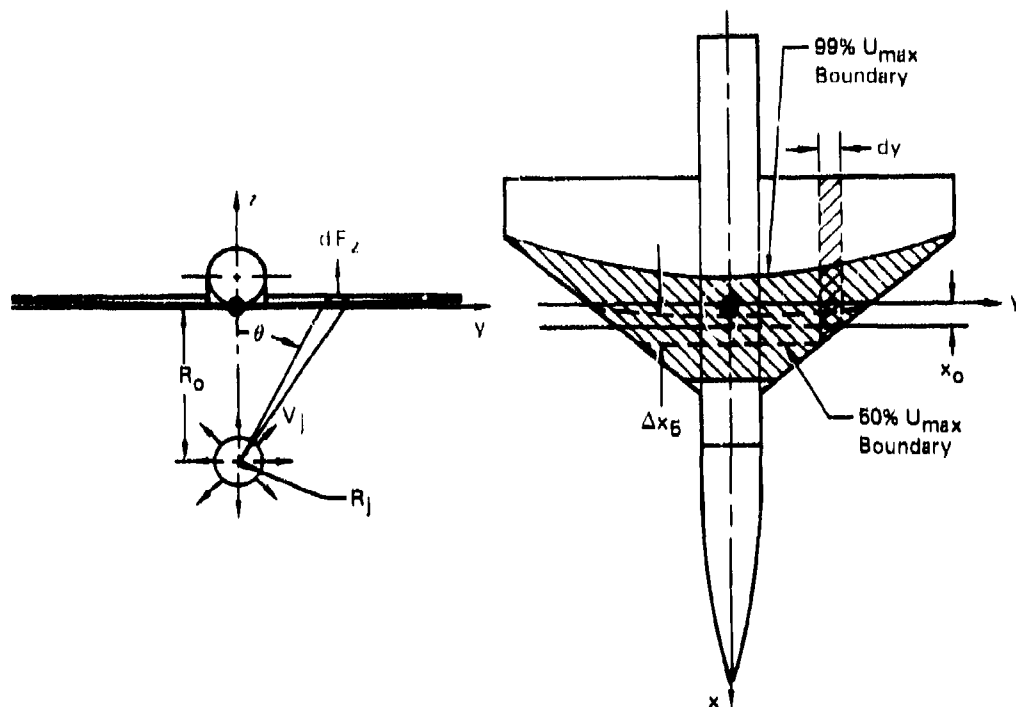
Since the radial jet has a finite width, the radial jet momentum is distributed in a neighborhood of the plane $x = x_0$. The crosshatched area in Figure 64 represents the "footprint" of this region on the planform located at $z = 0$. It is assumed that (for a configuration without stores or flaps), the pressure decays to ambient values outside this footprint region. Consequently, the integration limits x_T and x_L are determined by the shape and location of the fountain footprint, since the only non-zero force contribution arises from the area common to the strip and footprint, indicated by the double crosshatching in Figure 64.

The data of Reference 8 are used to analytically define the radial jet velocity distribution, which then leads to an integral for the total fountain impingement force. Letting Δx denote the total jet width, the data of Reference 8 have shown that for a constrained radial jet:

$$\Delta x = K_t (R - R_j), \quad (88)$$

and from Figure 64:

$$R = [R_0^2 + y^2]^{1/2},$$



GP77-0374-7B

FIGURE 64
CALCULATION OF FOUNTAIN IMPINGEMENT FORCE

then substituting in Equation (88):

$$\frac{\Delta x}{R_o} = K_t \left\{ \left[1 + (y/R_o)^2 \right]^{1/2} - \frac{R_j}{R_o} \right\} \quad (89)$$

For $P_j/R_o \ll 1$ the footprint boundary is given by two hyperbolas which represent the intersection between the conically shaped annular jet and the plane $z = 0$. The constant K_t depends on the location of the annular jet boundary, which is presently defined as that value of x for which the velocity has decayed to a specified fraction of the peak value for the profile at that point. The data of Reference 8 indicate that for the half-velocity boundary

$$K_t = 0.212$$

and then,

$$\Delta x_5 = (0.212) (R - R_j) \quad (90)$$

This boundary is shown schematically in Figure 64. It was felt that a greater fraction of the velocity profile should be included, however, and the boundary at which

$$\frac{V_R}{V_{\max}} = 0.01$$

was chosen. It is shown in Figure 8 that the self-similar radial jet velocity profiles are well represented by the universal function:

$$\frac{V_R}{V_m} = \text{sech}^2 \left[(1.763) \frac{x}{\Delta x_5} \right] \quad (91)$$

and this equation can be used to show that, if Δx^* denotes the 99% velocity boundary:

$$\Delta x^* = (3.394) \Delta x_5$$

which in Equation (89) results in:

$$\frac{\Delta x^*}{R_o} = (0.719) \left\{ \left| 1 + (y/R_o)^2 \right|^{1/2} - \frac{R_1}{R_o} \right\} \quad (92)$$

This equation permits calculation of the radial jet's footprint on the airframe undersurface. Since the annular jet velocity profiles are self-similar, it is advantageous to write Equation (87) in similarity variables. The equation is first written as:

$$\frac{dF_z}{dy} = \frac{\rho}{2} V_m^2 \cos^2 \theta \int_{\xi_T'}^{\xi_L'} \left(\frac{V}{V_m} \right)^2 d\xi'$$

where

$$\xi' = x - x_o$$

Normalizing the force by the total annular jet momentum flux

$$\dot{M}_j = 2\pi \rho R_j V_j^2 \Delta x_j$$

and normalizing all distances by R_o :

$$\frac{d\bar{F}_z}{dy} = \frac{1}{4\pi} \left(\frac{V_m}{V_j} \right)^2 \frac{\cos^2 \theta}{\Delta x_j} \left(\frac{R_o}{R_j} \right) \int_{\xi_T'}^{\xi_L'} \left(\frac{V_R}{V_m} \right)^2 d\xi'$$

and defining

$$\xi = \frac{x - x_o}{\Delta x_5} \quad (93)$$

$$\frac{d\bar{F}_z}{d\bar{y}} = \frac{1}{4\pi} \left(\frac{v_m}{v_j} \right)^2 \left(\frac{R_o}{R_j} \right) \left(\frac{\Delta x_j}{\Delta x_j} \right) \cos^2 \theta \int_{\xi_T}^{\xi_L} \left(\frac{v_R}{v_m} \right)^2 d\xi \quad (94)$$

It has been found in Reference 8 that the maximum velocity in the jet may be represented by

$$\frac{v_m}{v_j} = (2.496) \left[\frac{\Delta x_j R_j}{R(R - R_j)} \right]^{1/2} \quad (95)$$

Using Equations (90) and (95) in (94)

$$\frac{d\bar{F}_z}{d\bar{y}} = \frac{(0.660)}{2\pi} \left(\frac{R_o}{R} \right) \cos^2 \theta G(\xi_T, \xi_L) \quad (96)$$

where

$$G = \int_{\xi_T}^{\xi_L} (v_R/v_m)^2 d\xi$$

Using Equation (91) for the velocity profile, the function G may be integrated explicitly. The result is

$$G = (1.763)^{-1} \left[\tanh \xi^* - \frac{1}{3} \tanh^3 \xi^* \right]_{\xi_T^*}^{\xi_L^*}$$

where

$$\xi^* = (1.763) \xi$$

From the geometric relation

$$\cos \theta = \frac{R_o}{(y^2 + R_o^2)^{1/2}} = \frac{1}{(1 + \bar{y}^2)^{1/2}}$$

the y-integration may be written out. The final result for the fountain impingement force is:

$$\bar{F}_z = \frac{(0.374)}{2\pi} \int_0^{\bar{y}} \frac{[\tanh \xi^* - \frac{1}{3} \tanh^3 \xi^*]_{\xi_T^*}^{\xi_L^*} d\bar{y}}{(1 + \bar{y}^2)^{3/2}} \quad (97a)$$

and

$$\xi^* = (1.763) \left[\frac{x - x_0}{\Delta x_5} \right] \quad (97b)$$

In the limiting case of an infinitely large plane ($\xi_L^* \rightarrow \infty$, $\xi_T^* \rightarrow -\infty$, $\bar{y} \rightarrow \infty$), it may be shown that Equation (97a) reduces to

$$\bar{F}_z \sim \frac{0.5}{2\pi}$$

and consequently the total impingement force coefficient on an infinite plane would be

$$C_N = 2\bar{F}_z \sim \frac{1}{2\pi} \quad (98)$$

This is half the value given by Equation (74) showing that the normal force coefficient generated on an infinite plane is one half of the total vertical momentum flux in the fountain. This implies that there is a vertical momentum loss in the impingement process. The difference occurs because the normal dynamic pressure, rather than the normal momentum flux has been converted to normal force. The dynamic pressure leads to better agreement with data and will be retained, although it is realized that it results in the above anomaly.

Equations (97a and b) have been incorporated into a computer program to calculate the fountain impingement force. The aircraft planform is subdivided into strips of width Δy . At a given value of x_0 , integration limits (x_T and x_L) at the centerline of each strip are determined from a drawing of the aircraft planform and fountain footprint, analogous to the plan view in Figure 64. Equation (97a) and the fountain width distribution given by Equation (89) scale with R_0 , so as R_0 increases, the aircraft planform shrinks and a smaller section of the annular jet is captured, thus reducing the fountain impingement force. The integration limits are input to the program, and the integral in Equation (97a) is calculated. For symmetric situations such as indicated in Figure 64, the result may be multiplied by 2 to obtain the total impingement force. For an offset fountain where the axes of the opposed jets do not coincide with the x -axis ($y_0 \neq 0$), the computations would be carried out separately for each side $y \geq y_0$ and $y \leq y_0$. The hyperbolic functions in the integrand of Equation (97a) remain constant for $\xi^* > \xi^*_{.99}$, so the input can be simplified by selecting the wing trailing edge (or leading edge) for the integration limits, whenever their x coordinates exceed $|\Delta x_{.99}/2|$.

6.1.2 Calculation of Fountain Suckdown Force - Examination of data obtained from the test program to be described in Section 6.3.1 reveals that the calculated

fountain impingement force does not account for all the forces acting on the model. Although the calculation predicts the shape of the normal force curve obtained as the fountain impinges along different fuselage stations fairly well, the magnitude of this force, and in some cases its sign, were incorrect. Furthermore, the calculated fountain impingement force decreases as the distance R_0 between the virtual origin and the airframe (see Figure 64) increases, whereas the data revealed an opposite trend over a considerable range of R_0 . The reason for this behavior is that the fountain induces a suckdown force, in addition to an impact force.

Figure 65 shows a symmetric two-jet fountain impinging on a rectangular plate. As before, the fountain has been replaced by an equivalent radial jet. In this instance, however, the radial jet issues from a slot cut in the ground plane, with the plate located at a height H above this plane. This slot is shown in the section view A-A. The radial jet and the flow along the plate bottom entrain mass from the surrounding medium. Consider a control volume bounded by the plate lower surface, the projected plate area on the ground plane, and the lateral area of the volume bounded by these two areas. Continuity requires that there be a net mass flux of external air into this control volume, to balance the mass flux entrained by turbulent portions of the flowfield. This influx from the surrounding medium is responsible for reducing the pressure on the bottom of the plate, and creating a suckdown force.

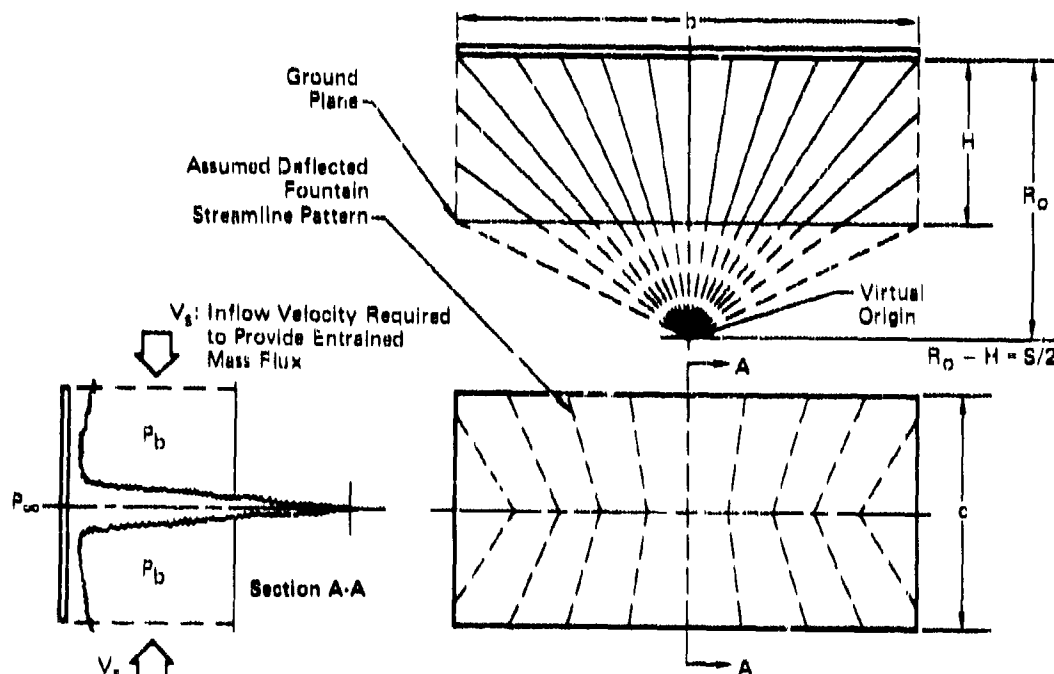


FIGURE 65
FOUNTAIN IMPINGEMENT ON A RECTANGULAR PLATE
Origin of Suckdown Force

QR77-6574-1

6.1.2.1 Fountain Suckdown Force for a Rectangular Plate - An approximate means of calculating the fountain suckdown force has been devised. The calculation is carried out in two steps. The first step estimates the total excess mass flux in the turbulent flow out of the control volume described in the previous paragraph. The second step estimates the pressure in this control volume by calculating the inflow velocity for a one-dimensional flow which supplies the excess mass flow across the control volume's lateral area.

To calculate the mass flow entrained by the turbulent flow, the flow turning geometry discussed in Section 6.1 and depicted in Figure 62 is used. The flow direction on the plate bottom will then appear as shown in the plan view of Figure 65. It is assumed that after the radial jet is split by impingement on the bottom of the plate, each half continues to entrain as if it had not been turned. Consequently, the total mass flux entrained on each side of the radial jet's plane of symmetry is the same as if the turning caused by impingement had never occurred. The total excess mass flow out of the control volume is therefore calculated from a diagram such as that shown in Figure 66. This diagram is obtained by "folding" the plate planform along the fountain impingement line PQ in Figure 65. For the symmetric case in Figure 65, the diagram on both sides of the fountain plane of symmetry is the same. If the fountain impinged at a distance x_0 from the plate midchord, then for $x > x_0$, the plate upper edge in Figure 66 would be at:

$$z = R_0 + \frac{c}{2} - x_0 ,$$

and for $x < x_0$, the upper edge would lie at:

$$z = R_0 + \frac{c}{2} + x_0 .$$

To compute the net mass flux entrained into the control volume, it is necessary to calculate the mass outflow normal to the lines

AB, BC, and CD

and subtract from this, the mass influx across the line AD. Constrained radial jet data obtained in Reference 8 are used to calculate this mass flow. Since the flow-field is symmetric, it is easier to work with the right hand side of Figure 66.

The net mass flow normal to the line OC is given by

$$\dot{m}_1 = \int_0^{b/2} \int_0^{\infty} \rho \left[V_R \cos \theta \right]_{z=R_0 + \frac{c}{2}} dx dy - \int_0^{b/2} \int_0^{\infty} \rho \left[V_R \cos \theta \right]_{z=R_0 - h} dx dy \quad (99)$$

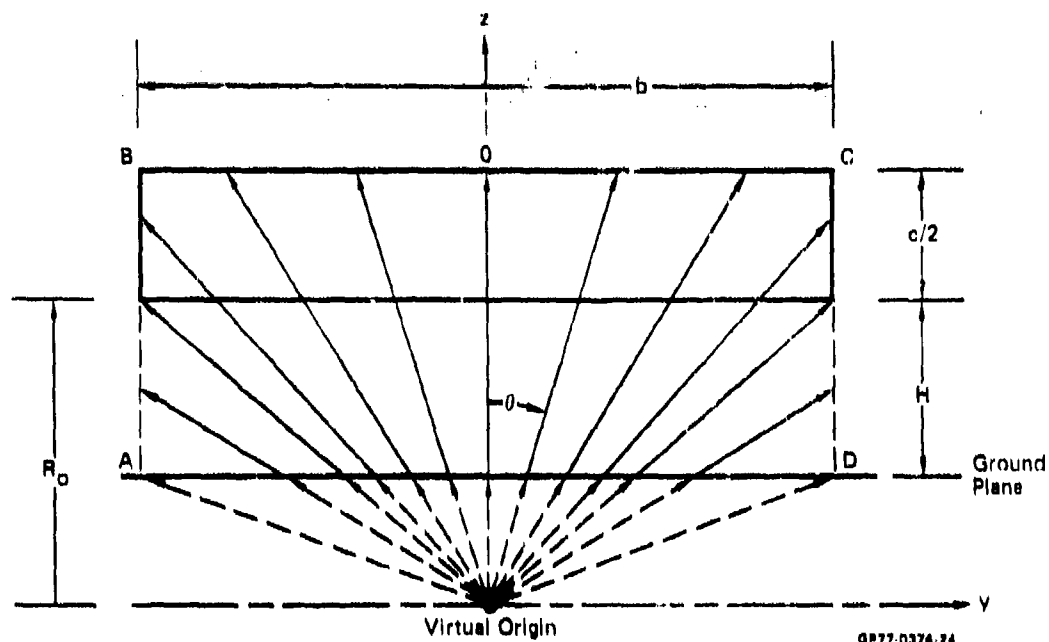


FIGURE 86
FOUNTAIN MASS FLOW DIAGRAM FOR IMPINGEMENT AT
MIDCHORD OF A RECTANGULAR PLATE

and normal to the line CD:

$$\dot{m}_2 = \int_{(R_o - h)}^{(R_o + \frac{c}{2})} \int_0^{\infty} \rho [V_R \sin \theta] dx dz \quad (100)$$

The x-integrations can be carried out using the self-similar properties of the radial jet velocity profile, and the data of Reference 8:

$$\int_0^{\infty} V_R dx = (V_m \Delta x_5) \int_0^{\infty} \left(\frac{V_R}{V_m} \right) d\left(\frac{x}{\Delta x_5} \right) .$$

Using Equation (91) to represent the correlated velocity profile, this becomes

$$\int_0^{\infty} V_R dx = (V_m \Delta x_5) \int_0^{\infty} \text{sech}^2 \left[(1.763) \left(\frac{x}{\Delta x_5} \right) \right] d\left(\frac{x}{\Delta x_5} \right)$$

and carrying out the integration, the result is:

$$\int_0^{\infty} V_R dx = \frac{V_m \Delta x_5}{(1.763)}.$$

In Reference 8 Witze has shown that the radial jet half-velocity thickness grows as

$$\Delta x_5 = (0.212) (R - R_j), \quad (101)$$

and the peak velocity decays as:

$$V_m = (2.496) V_j \sqrt{\frac{\Delta x_j R_j}{R(R - R_j)}} \quad (102)$$

where V_j - annular jet velocity

R_j - radius of annular jet nozzle .

Δx_j - width of annular jet nozzle

Then, using Equations (101) and (102)

$$\Delta x_5 V_m = (0.5291) V_j \sqrt{\Delta x_j R_j} \sqrt{\frac{R - R_j}{R}}. \quad (103)$$

For simplicity, it is assumed that $R \gg R_j$, so that with Equation (103), the velocity integral becomes:

$$\int_0^{\infty} V_R dx = (0.300) V_j \sqrt{\Delta x_j R_j}. \quad (104)$$

From Figure 66

$$\cos \theta = \frac{R_o + c/2}{\sqrt{(R_o + \frac{c}{2})^2 + y^2}} \quad (105)$$

or

$$\cos \theta = \frac{R_o - H}{\sqrt{(R_o - H)^2 + y^2}} \quad (106)$$

Substituting Equations (104) and (105) or (106) into (99):

$$\dot{m}_1 = (0.300) (\rho V_j) \sqrt{\Delta x_j R_j} \left\{ (R_o + \frac{c}{2}) \int_0^{b/2} \frac{dy}{\sqrt{(R_o + \frac{c}{2})^2 + y^2}} - (R_o - H) \int_0^{b/2} \frac{dy}{\sqrt{(R_o - H)^2 + y^2}} \right\}$$

and carrying out the integrations:

$$\begin{aligned} \dot{m}_1 = (0.300) \rho V_j \sqrt{\Delta x_j R_j} \left\{ (R_o + \frac{c}{2}) \ln \left[\left(\frac{b/2}{R_o + c/2} \right) + \sqrt{\left(\frac{b/2}{R_o + c/2} \right)^2 + 1} \right] \right. \\ \left. - (R_o - H) \ln \left[\left(\frac{b/2}{R_o - H} \right) + \sqrt{\left(\frac{b/2}{R_o - H} \right)^2 + 1} \right] \right\} \quad (107) \end{aligned}$$

To carry out the integration in Equation (100), note that

$$\sin \theta = \frac{b/2}{\sqrt{z^2 + (b/2)^2}}.$$

Using this relation, in addition to Equation (104), Equation (100) may be integrated explicitly, and the result is:

$$\dot{m}_2 = (0.300) \rho V_j \sqrt{\Delta x_j R_j} \left(\frac{b}{2} \right) \ln \left\{ \frac{(R_o + c/2) + \sqrt{(R_o + \frac{c}{2})^2 + (b/2)^2}}{(R_o - H) + \sqrt{(R_o - H)^2 + (b/2)^2}} \right\}. \quad (108)$$

Combining Equations (107) and (108), the total excess mass flux out of one quarter of the control volume is:

$$\dot{m}_{T, \frac{1}{4}} = (0.300) \rho V_j \sqrt{\Delta x_j R_j} K \quad (109)$$

where

$$K = (R_o + \frac{c}{2}) \ln \left[\left(\frac{b/2}{R_o + c/2} \right) + \sqrt{\left(\frac{b/2}{R_o + c/2} \right)^2 + 1} \right] \quad (110)$$

$$- (R_o - H) \ln \left[\left(\frac{b/2}{R_o - H} \right) + \sqrt{\left(\frac{b/2}{R_o - H} \right)^2 + 1} \right] + \\ + \frac{b}{2} \ln \left[\frac{(R_o + c/2) + \sqrt{(R_o + c/2)^2 + (b/2)^2}}{(R_o - H) + \sqrt{(R_o - H)^2 + (b/2)^2}} \right].$$

Referring to Figure 65, it is assumed that a one-dimensional flow across one quarter of the control volume's lateral area supplies this excess mass flow, so

$$\dot{m}_{T \frac{1}{4}} = \rho V_s A_{L \frac{1}{4}} \quad (111)$$

where

$$A_{L \frac{1}{4}} = \left(\frac{b + c}{2} \right) H \quad (112)$$

Assuming ambient pressure acts on the plate upper surface, the suckdown force will be given by

$$F_{s \frac{1}{4}} = (p_b - p_\infty) A_{w \frac{1}{4}} \quad (113)$$

where

$$A_{w \frac{1}{4}} = \frac{bc}{4}$$

and

$$p_b = p_\infty - \frac{\rho}{2} V_s^2 \quad (114)$$

Using Equation (111), the suckdown force then becomes

$$F_{s \frac{1}{4}} = - \left(\frac{1}{2} \right) \frac{\dot{m}_{T \frac{1}{4}}^2}{\rho} \frac{A_{w \frac{1}{4}}}{A_{L \frac{1}{4}}^2}$$

Substituting from Equation (109):

$$F_{s\frac{1}{4}} = - (0.045) \frac{A_{w\frac{1}{4}}}{A_{L\frac{1}{4}}^2} [\rho V_j^2 (\Delta x_j R_j) K^2] \quad (115)$$

The total suckdown force is given by

$$F_s = 4 F_{s\frac{1}{4}}$$

Defining a force coefficient by normalizing by the total radial jet momentum flux:

$$C_s = \frac{F_s}{2\pi \rho R_j \Delta x_j V_j^2} \quad (116)$$

and substituting for F_s

$$C_s = - (0.0286) \frac{A_{w\frac{1}{4}}}{A_{L\frac{1}{4}}^2} K^2$$

Substituting for the planform and lateral area

$$C_s = - (0.0286) \left[\frac{bc}{(b+c)^2 H^2} \right] K^2 \quad (117)$$

where K has been given in Equation (110). The following case has been calculated.

$$\begin{aligned} b &= 20 \text{ in} \\ c &= 8 \text{ in} \\ (R_o - H) &= 2 \text{ in} \\ R_o &= 4 - 9 \text{ in} \end{aligned}$$

For the case where the fountain impinges at midchord, the results are shown in Figure 67. The fountain suckdown force calculated according to the above equations is shown. The force is negative and increases towards zero as R_o increases. The fountain impingement force calculated by the method detailed in Section 6.1.1.2 is also shown. This force is positive and decreases in magnitude as R_o increases.

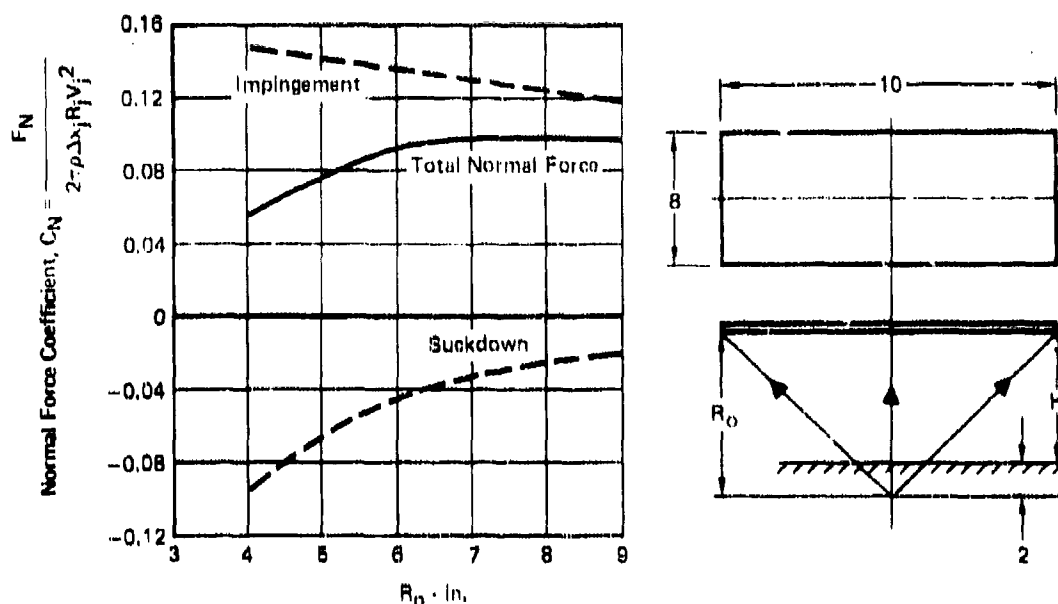


FIGURE 67
CALCULATED FOUNTAIN IMPINGEMENT AND SUCKDOWN
FORCES ON A RECTANGULAR PLATE

GP77 0374-28

The result of summing the two effects is a positive force which initially increases with R_0 , and then decreases as the negative suckdown contribution approaches zero.

In the fountain suckdown calculation, the radial jet thickness has not been taken into account, and the radial jet "footprint" has not been considered, as was done for the impingement force. Furthermore, it has been assumed that the ambient air influx occurs across the entire lateral area of the control volume. In reality, part of this area is occupied by the turbulent flow. While refinements to the method to take account of these factors could be developed, the main objective has been to obtain approximate answers that yield the correct trends.

6.1.2.2 Fountain Suckdown Force for a Trapezoidal Wing - Figure 68 shows the geometry relevant to the calculation of the fountain suckdown force for a trapezoidal wing. In the sketch of the wing geometry, the radial jet representing the fountain is shown to impinge at a distance x_0 from the origin. As in the rectangular plate case, the mass flow diagrams are obtained by "folding" the wing planform along the intersection line with the fountain plane of symmetry. The excess mass flux out of the control volume bounded by the wing undersurface, its projection on the ground plane, and the lateral area between these surfaces, is calculated from the mass flow diagrams 68a and 68b. Figure 68a indicates the geometry for $x > x_0$. In this case, the mass outflow is calculated from one-half of the radial jet mass flow across the

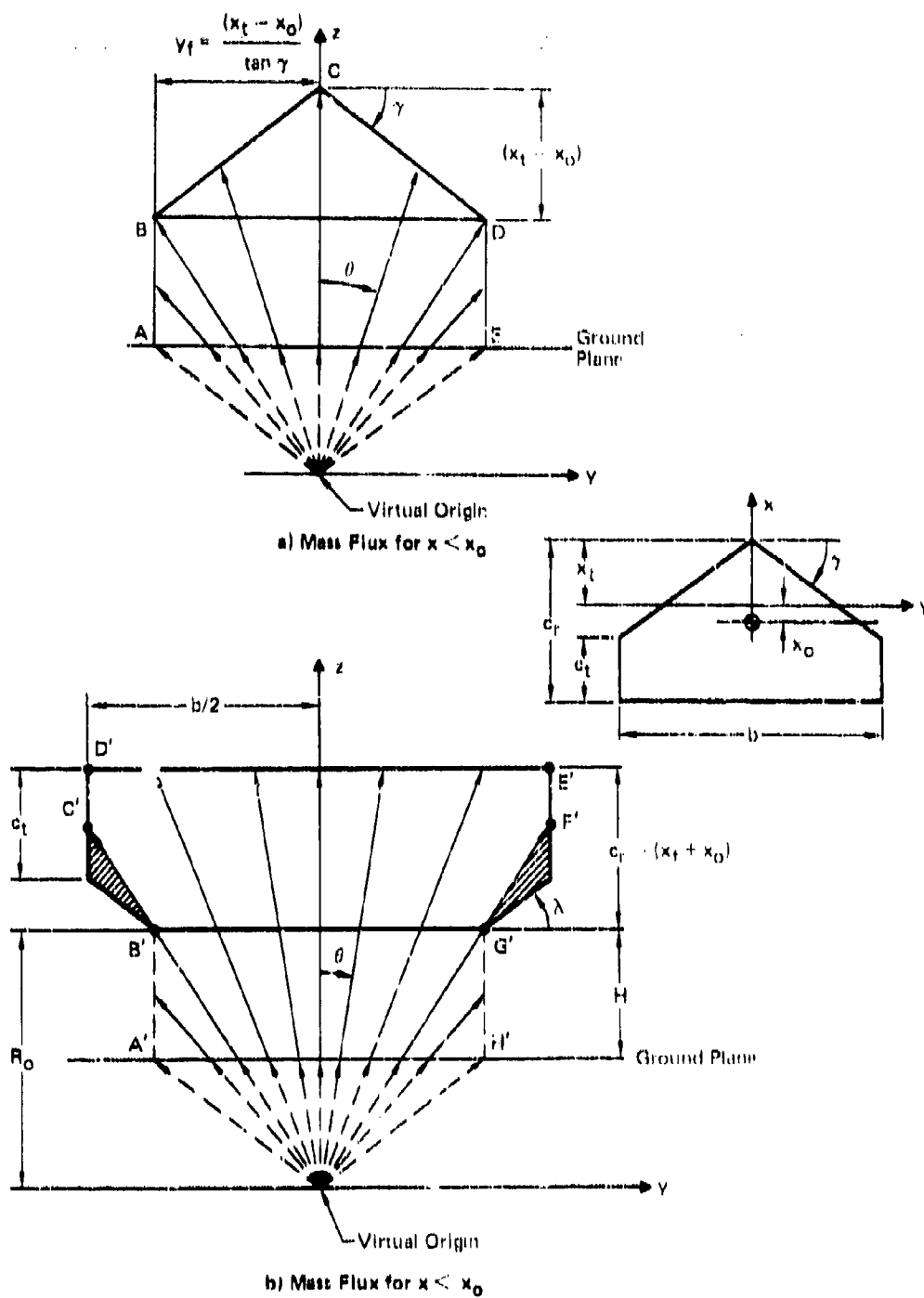


FIGURE 88
FOUNTAIN MASS FLOW DIAGRAMS FOR IMPINGEMENT AT
STATION x_0 - TRAPEZOIDAL WING

11P77 03/74 26

boundary A'B'C'D'E'F'G'H', and the inflow across the boundary A'H' is subtracted out. Note that the shaded areas in Figure 68b do not contribute to fountain entrainment, since according to the assumed radial jet impingement process (Figure 62), these areas are not wetted by the flow.

The calculations proceed as in the rectangular plate case, except for the outflow at the swept wing leading edge. Referring to Figure 68a, the mass outflow across the line CD is given by:

$$\dot{m}_e = \int_0^{s_f} \int_0^{\infty} \rho V_R \cos(\gamma - \theta) dx ds$$

Since $ds \cos \gamma = dy$

$$\dot{m}_e = \int_0^{y_f} \int_0^{\infty} \rho V_R \frac{\cos(\gamma - \theta)}{\cos \gamma} dx dy \quad (118)$$

Using Equation (104) for the x integration:

$$\dot{m}_e = (0.300) \rho V_j \sqrt{\Delta x_j R_j} \int_0^{y_f} \frac{\cos(\gamma - \theta)}{\cos \gamma} dy \quad (119)$$

The equation describing the swept leading edge is:

$$z = -(\tan \gamma) y + (R_o + x_t) \quad (120)$$

Consequently, along the leading edge

$$\cos \theta = \frac{-(\tan \gamma) y + (R_o + x_t)}{\left\{ [(\tan \gamma) y - (R_o + x_t)]^2 + y^2 \right\}^{1/2}} \quad (121a)$$

and

$$\sin \theta = \frac{y}{\left\{ [(\tan \gamma) y - (R_o + x_t)]^2 + y^2 \right\}^{1/2}} \quad (121b)$$

Expanding the cosine term in Equation (118) and using Equations (121)

$$\dot{m}_e = (0.300) \rho V_j \sqrt{\Delta x_j R_j} \left\{ (R_o + x_t) \int_0^{y_f} \frac{dy}{\left[\frac{y^2}{\cos^2 \gamma} - 2 \tan \gamma (R_o + x_t) y + (R_o + x_t)^2 \right]^{1/2}} \right\}$$

and carrying out the integration:

$$\dot{m}_e = (0.300) \rho V_j \sqrt{\Delta x_j R_j} K_1 \quad (122)$$

where

$$K_1 = (R_o + x_t) \cos \gamma \ln \left\{ \frac{y_f - \sin \gamma \cos \gamma (R_o + x_t) + \left[y_f^2 - 2 \sin \gamma \cos \gamma (R_o + x_t) y_f + \cos^2 \gamma (R_o + x_t)^2 \right]^{1/2}}{\cos^2 \gamma (R_o + x_t) (1 - \sin \gamma)} \right\} \quad (123a)$$

$$\text{and } y_f = \frac{x_t}{\tan \gamma} \quad (123b)$$

Equations (122) and (123), in addition to mass outflow and inflow results along the other boundaries indicated in Figure 68, have been used to calculate the suckdown force due to radial jet impingement on the undersurface of a trapezoidal wing planform. The results are presented in Section 6.3, where they are compared to data from the fountain impingement test program described therein.

The methods for calculating fountain impingement and suckdown forces for two-jet symmetrical fountains have been extended to multiple-jet fountain configurations. The general technique, and its application to a four-jet fountain configuration, are detailed in the next Section.

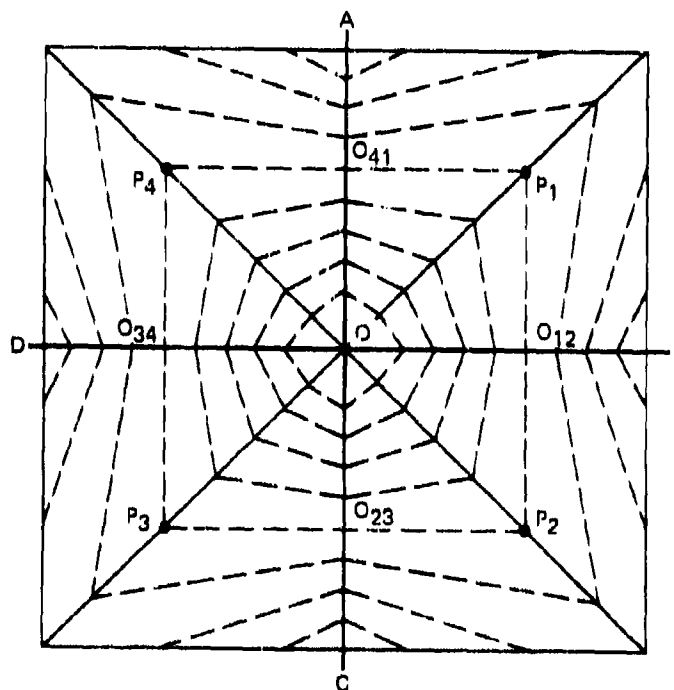
6.2 Multiple-Jet Fountain Impingement and Suckdown

As discussed in Section 5.3.1, the various fountain segments which make up three or four-jet fountain configurations are subdivided into "inner region sectors" and "outer region sectors". The inner region sectors interact to form a central fountain, which is not currently well defined. However, it has been argued in Section 5.3.1 that in the inner region, the total vertical momentum flux across planes parallel to the ground plane must be conserved, provided the central fountain is confined to the inner region. When calculating a multiple-jet fountain impingement force, it is necessary to consider the footprint of the inner and outer fountain sectors on the aircraft planform. Because of conservation of vertical momentum in the inner region, as long as the inner region footprint lies wholly within the aircraft planform, the fountain impingement force due to the inner region segments will be independent of height above the ground plane. The outer region sectors will behave

as in the two-jet fountain case, contributing a decreasing amount to the impingement force as the aircraft height above the ground plane increases.

The calculation of fountain suckdown forces for multiple-jet configurations is greatly complicated by the presence of a central fountain and interaction between various fountain segments after they impinge on the airframe undersurface. For example, Figure 69 depicts an idealized flow pattern caused by impingement of a four-jet fountain on the undersurface of a square plate. The planes of symmetry of the four radial jets which represent the fountain intersect the plate along the lines OA, OB, OC, and OD. The segments OO_{12} , OO_{23} , OO_{34} , and OO_{41} correspond to the inner sectors, and the square $P_1P_2P_3P_4$ defines the inner region. The idealized turning process illustrated in Figure 62 yields the streamline pattern depicted by the dotted lines in Figure 69. This overall pattern has been highly idealized, for the following reasons:

1. In the neighborhood of the point O, central fountain impingement occurs, leading to an unknown streamline pattern.



GP77 0374-80

FIGURE 69
IDEALIZED STREAMLINE PATTERN FOR A SQUARE, FOUR-JET
FOUNTAIN IMPINGING ON THE BOTTOM OF A FLAT PLATE

2. Along the diagonal OP_1 , OP_2 , OP_3 , and OP_4 , the flows along the plate undersurface interact with each other.

The central fountain and the flow near diagonals OP_1 , OP_2 , OP_3 , and OP_4 may well develop as turbulent flows with entrainment characteristics which differ from those for the radial jets which generate them. These entrainment characteristics are completely unknown, so for computational purposes, the following assumption will be made:

- o The central fountain and the flows generated by interaction of flows along the plate undersurface do not entrain any excess ambient air.

With the above assumption, the radial jet entrainment rate is assumed to exist along each one of the sectors BOP_1 , BOP_2 , etc.

Four-jet fountain impingement and suckdown forces have been calculated for the configurations in the program detailed in Section 6.3. A description of these calculations is included in the sections following.

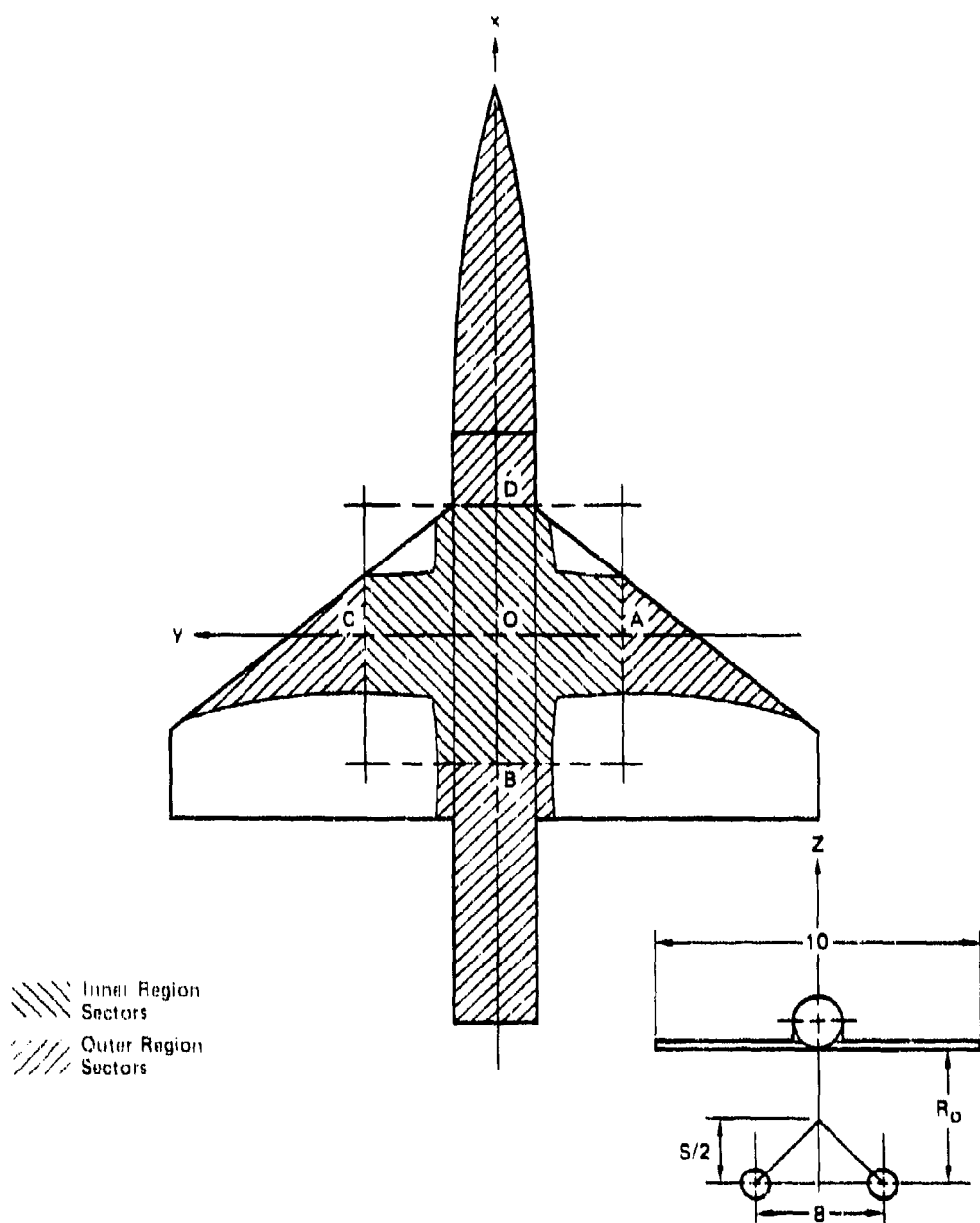
6.2.1 Calculation of Four-Jet Fountain Impingement Force - Figure 70 shows the planform of the model tested in the fountain impingement experiment described in Section 6.3, and a front view of the model orientation relative to two of the four radial jets which simulate the fountain. The planes of symmetry of the four radial jets intersect the plane of the model planform along lines OA, OB, OC, and OD. The eight-inch square defined by the radial jet centerlines bounds the inner region. For the cases calculated the inlet region center lies directly below the model reference point. Calculations have been carried out for varying values of R_0

$R_0 = 5, 6, 7, \text{ and } 8 \text{ inches.}$

In Figure 70, the inner and outer region radial jet sectors are shown by different crosshatching. The

$$V_R/V_{\max} = 0.01$$

footprint defined in Section 6.1.1.2 is shown. For the outer region sectors, the impingement force is calculated by the method outlined in Section 6.1.1.2. For the inner region sectors, it is assumed that the entire inner region footprint is captured by the planform. Consequently, the conservation of total vertical momentum flux, discussed in Section 6.2, permits calculation of the inner region impingement force, without requiring detailed knowledge of the central fountain's flowfield. The inner region force is equated to one-half of the vertical momentum flux in the inner jet sector, computed at $z = 5/2$ (see the sketch in Figure 70). From Equation (73) in Section 5.3.1, the force transmitted by each of the inner region sectors is:



GP77 0174 b1

FIGURE 70
FOUR-JET FOUNTAIN IMPINGEMENT FOOTPRINT
 $x_0 = 0$, $R_0 = 6$ in.

$$F_{z_{I_1}} = \frac{\dot{M}_{z_{I_1}}}{2} = \frac{\dot{M}_{jR_1}}{4\pi} \sin \theta_{12} \quad (124)$$

For a square jet arrangement, $\theta_{12} = \pi/4$; so for all four inner region sectors, since the jet radial momentum fluxes are all equal:

$$F_{z_{I_{total}}} = 4F_{z_{I_1}} = (0.225) \dot{M}_{jR} \quad (125)$$

The total fountain impingement force is then calculated as follows:

$$F_{z_{total}} = F_{z_{I_{total}}} + 2F_{z_{wing}} + F_{z_{forward}} + F_{z_{aft}}$$

where

$F_{z_{wing}}$ - normal force induced on one wing panel by the fountain outer sector.

$F_{z_{forward}}$ - impingement force induced on forward fuselage by outer sector

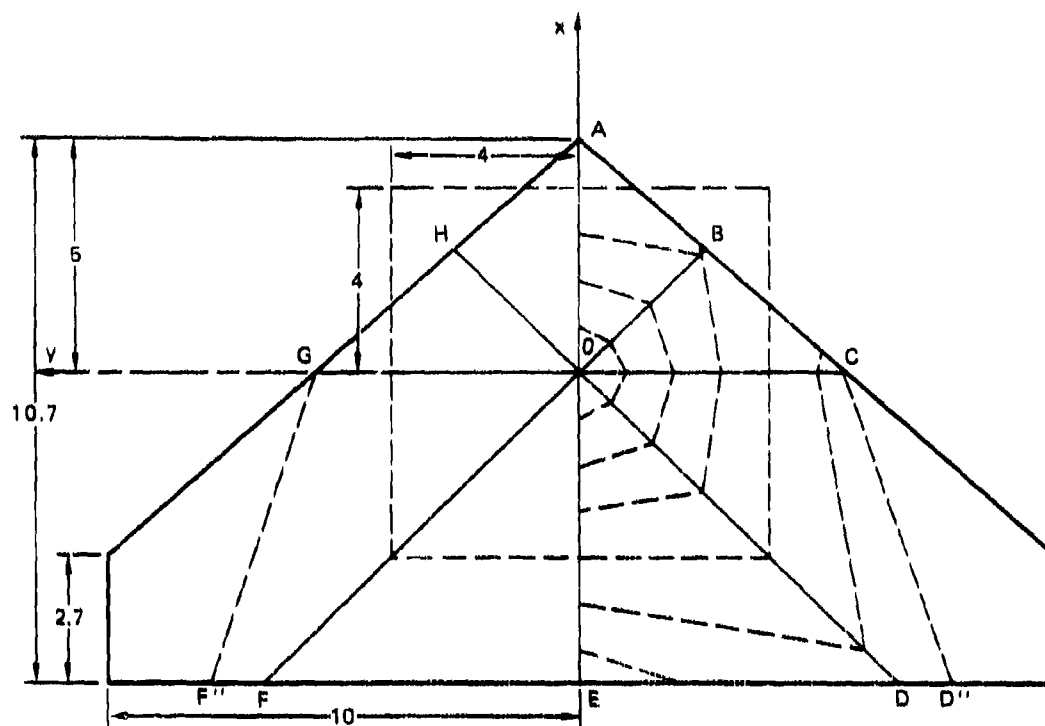
$F_{z_{aft}}$ - impingement force induced on aft fuselage by outer sector.

The impingement normal force coefficient is then defined as follows:

$$C_{N_I} = \frac{F_{z_{total}}}{4\dot{M}_{jR}} \quad (126)$$

This normal force coefficient is combined with a suckdown force coefficient to obtain the total force acting on the model. The calculation of fountain suckdown forces is outlined in the next Section.

6.2.2 Calculation of Four-Jet Fountain Suckdown Force - Figure 71 shows the idealized flow pattern created when a four-jet fountain strikes the undersurface of a trapezoidal wing planform. The wing dimensions correspond to the theoretical planform of the model tested in the fountain impingement experiment described in Section 6.3. For simplicity, the presence of the fuselage is neglected in these computations. Figure 71 shows one-half of the flow pattern derived for the square plate case in Figure 69, superimposed on the trapezoidal wing planform. The inner region is defined by the 8 in. square. As described in Section 62, it is assumed that the central fountain and the flow interactions near lines OB, OD, OF and OH do not entrain any additional flow. Consequently, these lines constitute boundaries at which the total entrained mass flow is to be computed.



QP77-0274-48

FIGURE 71
IDEALIZED FLOW DIRECTIONS ON TRAPEZOIDAL WING UNDERSURFACE
AFTER FOUR-JET FOUNTAIN IMPINGEMENT

Fountain mass flow diagrams analogous to those shown for two-jet fountain suck-down in Figures 66 and 68 are set up. In this case, however, the wing planform is to be "folded" about the two lines, AOE and GOC. The fold along AOE is performed to calculate the entrainment from the fore and aft radial jets, whose planes of symmetry go through this line. The fold along GOC is performed to calculate the entrainment from the left and right radial jets, whose planes of symmetry go through this line. Figure 72 indicates the mass flow diagrams in the x-z plane, with the wing planform folded along AOE. The ground plane is located at a distance H below the model. For the region located at

$$x > 0,$$

the entrained mass flow is computed as follows:

$$\text{Entrained mass flow} = \text{Mass outflow at A'ABOO'} - \text{Mass inflow at A'O'}$$

For the region located at

$$x < 0$$

$$\text{Entrained mass flow} = \text{Mass outflow at O'ODEE'} - \text{Mass inflow at O'E'}$$

These mass fluxes are calculated by formulae analogous to those used for single radial jets striking rectangular and trapezoidal wings, as described in Section 6.1.2. The suckdown forces acting on each portion of the wing are calculated by requiring

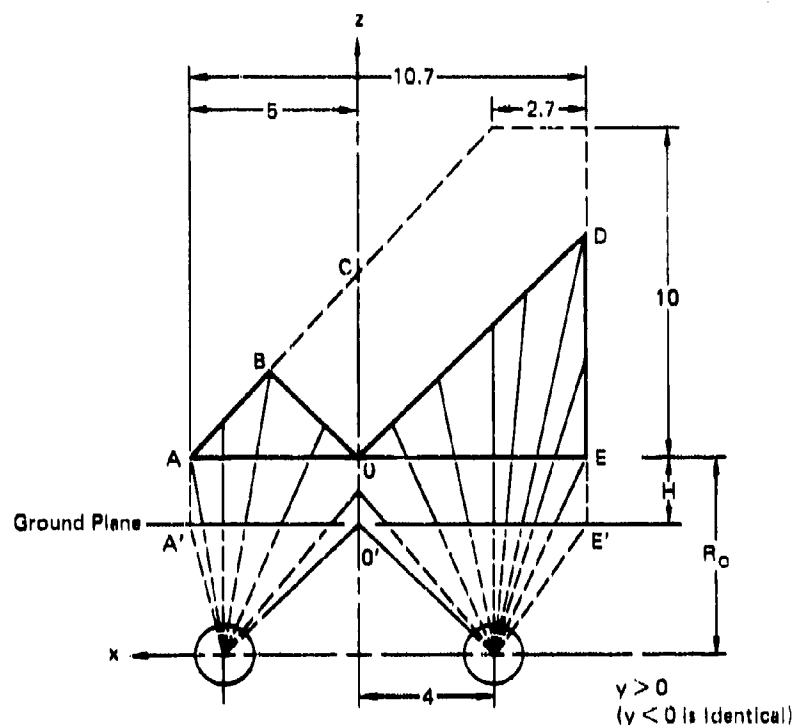


FIGURE 72
MASS FLOW DIAGRAM IN x-z PLANE

an inflow velocity across each lateral area to supply the entrained mass flow, and relating the velocity to a pressure as described in Section 6.1.2. The calculations associated with Figure 72 permit an estimate of suckdown forces for wing area segments ABO, ODE (see Figure 71), and their mirror images AHO and OFE. To calculate the rest of the suckdown force, the mass flow diagrams in Figure 73 are used. For one half of the section at

$$x > 0$$

$$\text{Entrained mass flow} = \text{Mass outflow at } O'OBCC' - \text{Mass inflow at } O'C'$$

and for one half of the section at $x < 0$:

$$\text{Entrained mass flow} = \text{Mass outflow at } O'ODD''CC' - \text{Mass inflow at } O'C'$$

Note that (as is the single radial jet case), part of the wing area is not wetted by the impinged flow, and may then be left out of the calculation. The calculations associated with Figure 73 permit an estimate of suckdown forces for wing area segments OBC and CD''DO (see Figure 71); and for their mirror images OHG and GF''FO.

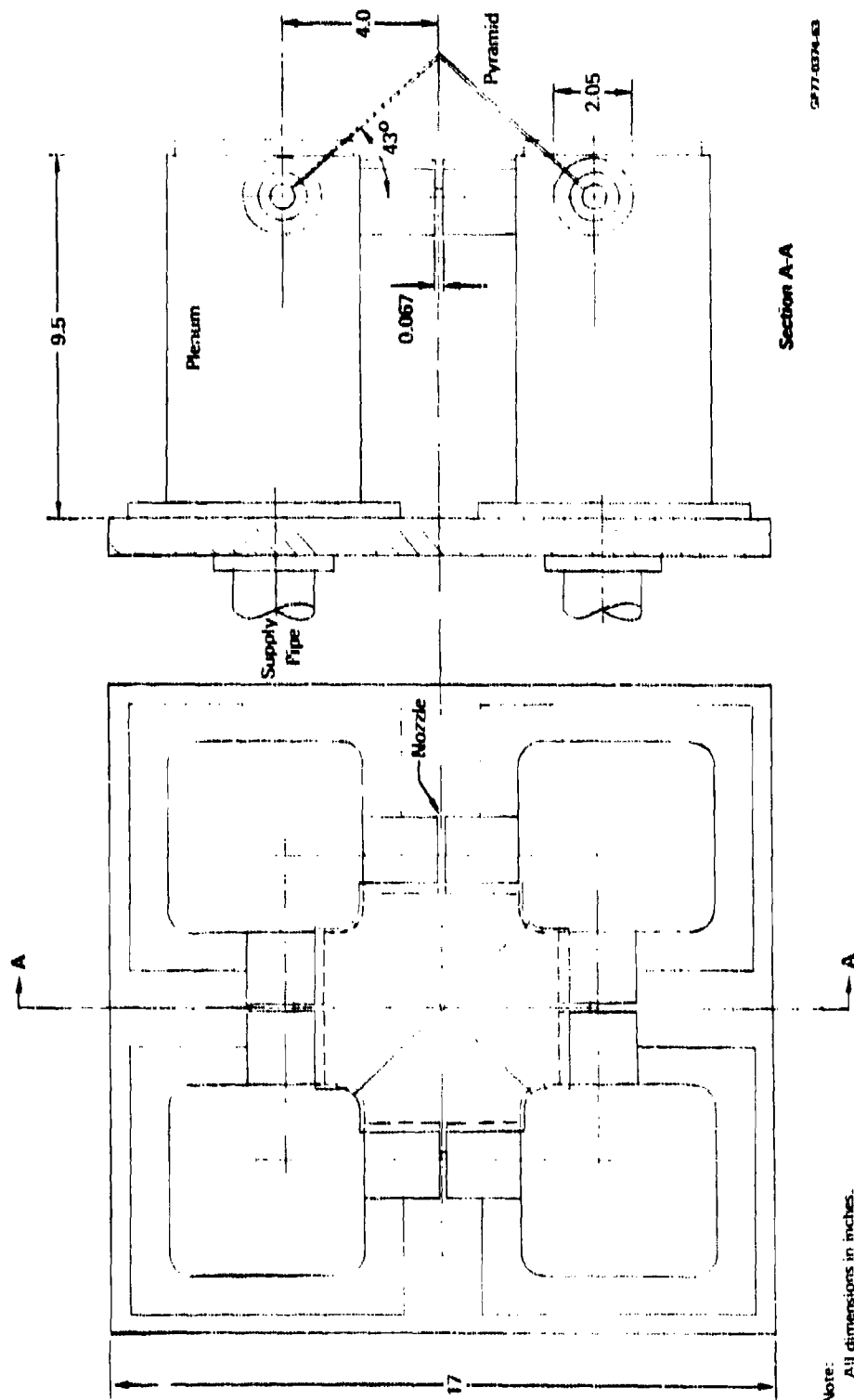
After the lengthy computations described above are completed, the suckdown forces for each part of the wing area are summed, and a total suckdown force coefficient is calculated. The results obtained are compared to data in Section 6.3.

6.3 Comparison of Predicted and Experimental Fountain Forces

As part of the MCAIR IKAD program described in Reference 23, a fountain generator was designed and fabricated. This apparatus is capable of simulating the fountain generated by a pair of circular, perpendicular jets of equal thrust, or by four circular perpendicular jets of equal thrust arranged in a square pattern. The simulated fountains were allowed to impinge on a representative aircraft model, and the forces and moments induced on the model were measured by a six-component strain gauge balance. After a brief description of the apparatus and test setup, measured normal forces are compared to the results predicted using the methods described above.

6.3.1 Fountain Impingement Test Apparatus - The fountain generator design was based upon the analogy between a symmetric two-jet fountain and a radial jet, and the postulated equivalence between multiple-jet fountains and combinations of radial jets. The fountain generator was used to isolate the fountain forces from the free and wall jet suckdown forces which would exist if the entire flowfield were simulated at once. Figure 74 is a schematic of the fountain generator assembly. Four pipes are supplied with high pressure air from an existing facility. Each pipe discharges into one of four plenums, which are equipped with porous plates and screens to smooth the flow. Each plenum supplies two nozzles. The four plenums and eight nozzles are arranged in a square pattern, creating four annular nozzles through which the air exhausts, forming four annular jets. To simulate two-jet fountains, three of the annular nozzles were capped. To simulate four jet fountains all the nozzles were operated. As explained in Section 5, only a fraction of each annular jet's mass flux should contribute to the four-jet fountain. Consequently, a detachable surface in the shape of a pyramid was used to split the annular jets when simulating a four-jet fountain, as indicated in Figure 74. The forces and moments produced by the simulated fountain impingement on a wing-fuselage model were measured by an internal six-component strain gauge balance. During the first phase of the test program, a total pressure rake was used to probe the jet flowfields. Figure 75 shows the overall test arrangement, including the fountain generator, model, rake, and support structures. The model could be translated in three directions relative to the fixed fountain generator, and rotated about all three axes. High and low wing configurations were tested, with and without trailing edge flaps and simulated underwing stores.

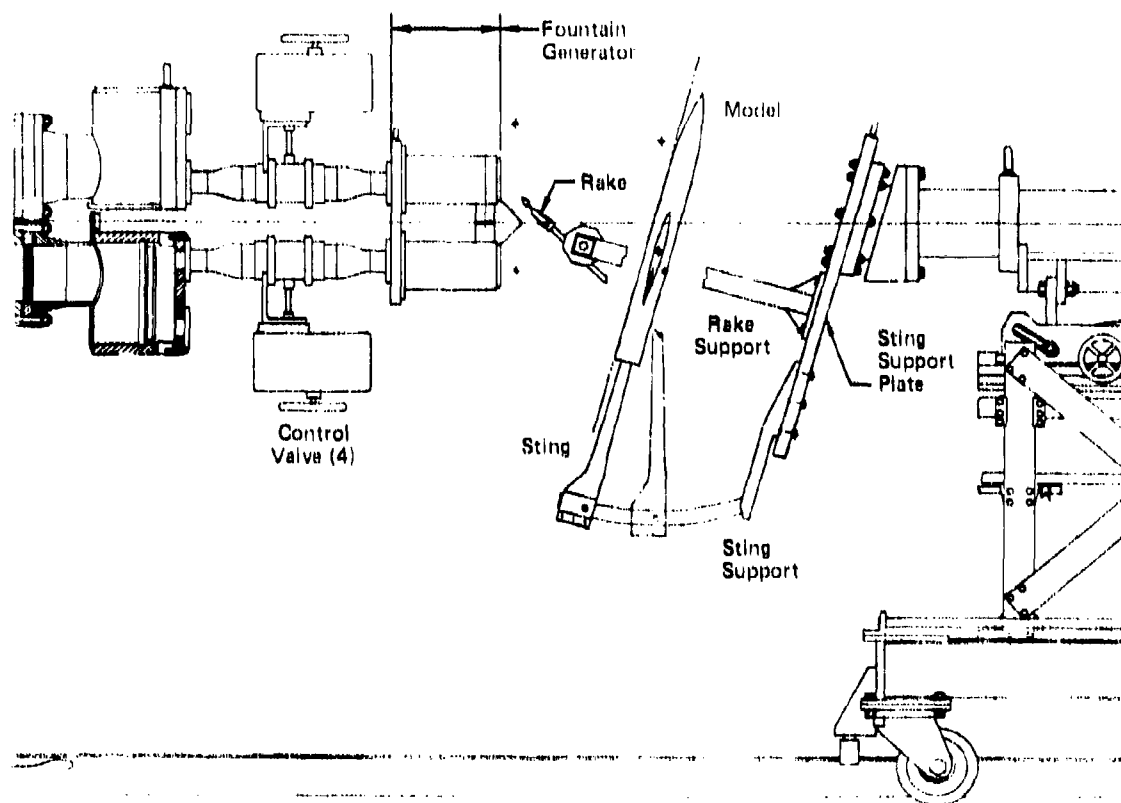
6.3.2 Comparison of Two-Jet Fountain Results - An examination of the data obtained from this test program soon revealed the necessity to include a fountain suckdown force. For a single radial jet, Figure 76 compares some test results to a calculation of the fountain impingement force carried out by the method described in Section 6.1.1.2. For the cases shown, a single radial jet impinged upon a clean,



GP77-0374-83

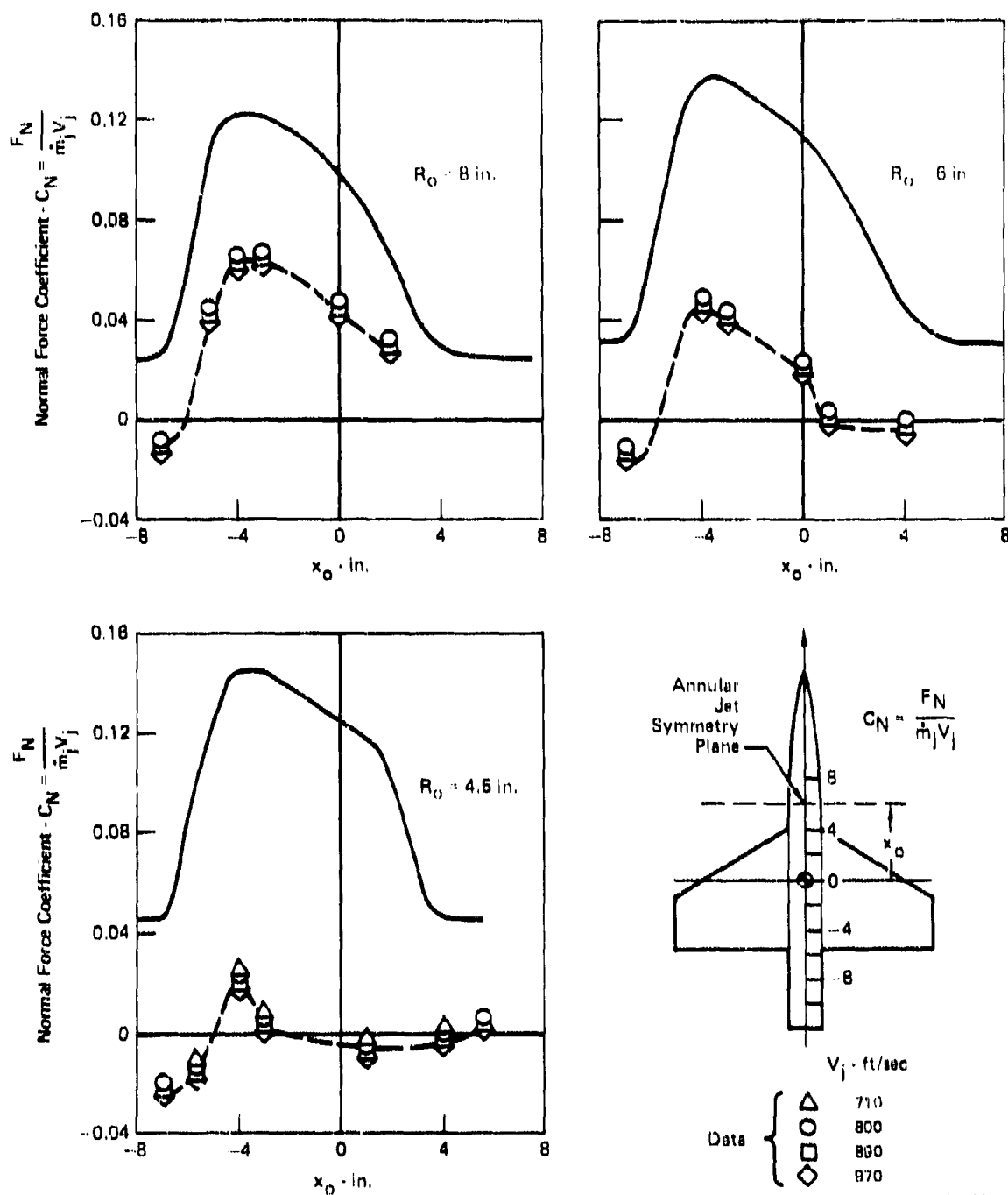
FIGURE 74
FOUNTAIN GENERATOR SCHEMATIC

Note:
All dimensions in inches.



UP77-0374-02

FIGURE 76
FOUNTAIN IMPINGEMENT TEST APPARATUS



GP77 0374 68

FIGURE 76
CALCULATED JET IMPINGEMENT FORCE COMPARED TO MCAIR IRAD TEST DATA
SINGLE ANNULAR JET, LOW WING
(NEGLECTING FOUNTAIN SUCKDOWN)

low wing model configuration, with the plane of the annular nozzle oriented perpendicularly to the model plane of symmetry. This arrangement simulates the fountain for a two-lift-jet aircraft with the jets mounted in the fuselage. The curves indicate the variation in normal force coefficient as the jet impinges at different stations along the axis. As before, the normal force coefficient is defined as:

$$C_N = \frac{\text{Normal force on model}}{\text{Annular jet momentum flux}}$$

For the four jet exit velocities tested, the results indicate that fairly good data correlation is obtained using this coefficient. Each one of the graphs corresponds to a different value of the distance (R_0) between the nozzle centerline and the reference point on the bottom of the fuselage. It is obvious that the calculated jet impingement force does not account for all the forces acting on the model. For $R_0 = 8$ and 6 in., the jet impingement calculation predicts the shape of the curve fairly well. A constant force is created when the jet impinges on the fuselage. A sharp increase in normal force occurs as the jet starts to impinge on the wing trailing edge, rising to a peak value when x_0 lies in the region of maximum planform span. Then a subsequent slower decay as the jet impinges on a region of reduced wing span containing the swept wing leading edge. The level of the forces, and in some cases their sign is not accurately predicted by the impingement calculation. It appears that in addition to the impingement force, a substantial fountain suckdown force is also acting on the model. This is evident in Figure 77, which is a crossplot of the data in Figure 76 for three jet impingement stations x_0 . One would expect that as R_0 increases, the impingement force on the model would decrease, since a smaller sector of the annular jet impinges on the model. The data however, show the opposite trend. In fact, for $x_0 = -7$ the force on the model is negative for all values of R_0 . Since the total fountain force must eventually approach zero, all the curves in Figure 77 must eventually approach zero, but this behavior was not yet evident within the R_0 range tested.

When the fountain suckdown force coefficient is included, the prediction is substantially improved. As indicated in Figure 67, for a rectangular plate, the fountain suckdown force is negative, and approaches zero as R_0 increases. Figure 78 compares the calculated total normal force coefficient, for the trapezoidal-wing model, to the data. The variation with R_0 is indicated, for two values of the jet impingement station x_0 . The calculated normal force coefficient includes a suckdown term obtained by the method outlined in Section 6.1.2.2. Although the agreement between data and theory is far from perfect, the theory predicts the data trends reasonably well. The agreement could perhaps be improved by refining the suckdown

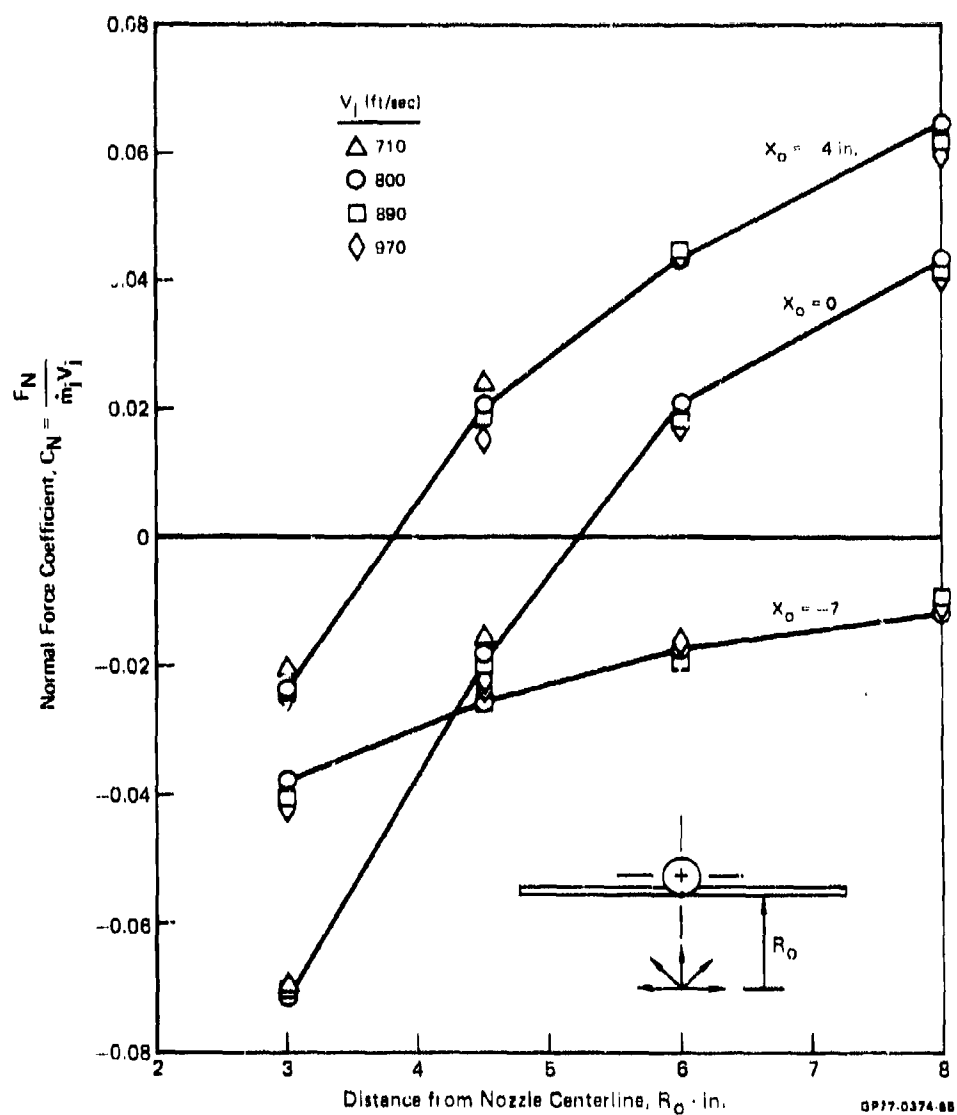


FIGURE 77
VARIATION OF NORMAL FORCE WITH HEIGHT ABOVE JET ORIGIN

calculation (e.g.) including radial jet thickness effects, but there is a more fundamental factor which obscures comparisons to data from this test program. As indicated in Figure 75, there was no simulation of the ground plane during the test. The calculation assumes that there is a ground plane which constrains the area through which the entrained mass flow must be supplied. For the computed results shown in Figure 78, it was assumed that the ground board was located flush with the top of the fountain generator plenums (the pyramid was removed for this single-jet configuration), but this is only a crude approximation of the actual geometry. Unfortunately, this problem must remain unsolved at present. A test program is currently planned, which will include the ground board and allow the radial jets to exhaust through appropriate slots in this ground board. This will provide a more realistic simulation of the actual conditions, and will permit a more direct comparison of theoretical and experimental results.

6.3.3 Comparison of Four-Jet Fountain Results - The calculation of four-jet fountain impingement and suckdown forces has been detailed in Sections 6.2.1 and 6.2.2. Results were obtained specifically for the configuration tested. Figure 79 compares the predicted force coefficient to the data. As indicated by the sketch in the figure, the four radial jet planes of symmetry go through the model x and y axes. The agreement between theory and data is reasonably good in this case, which may be due to the fact that the fountain generator pyramid constrained the flow underneath the model. When performing the suckdown calculations outlined in Section 6.2.2, it was again assumed that the ground plane was flush with the tops of the fountain generator plenums.

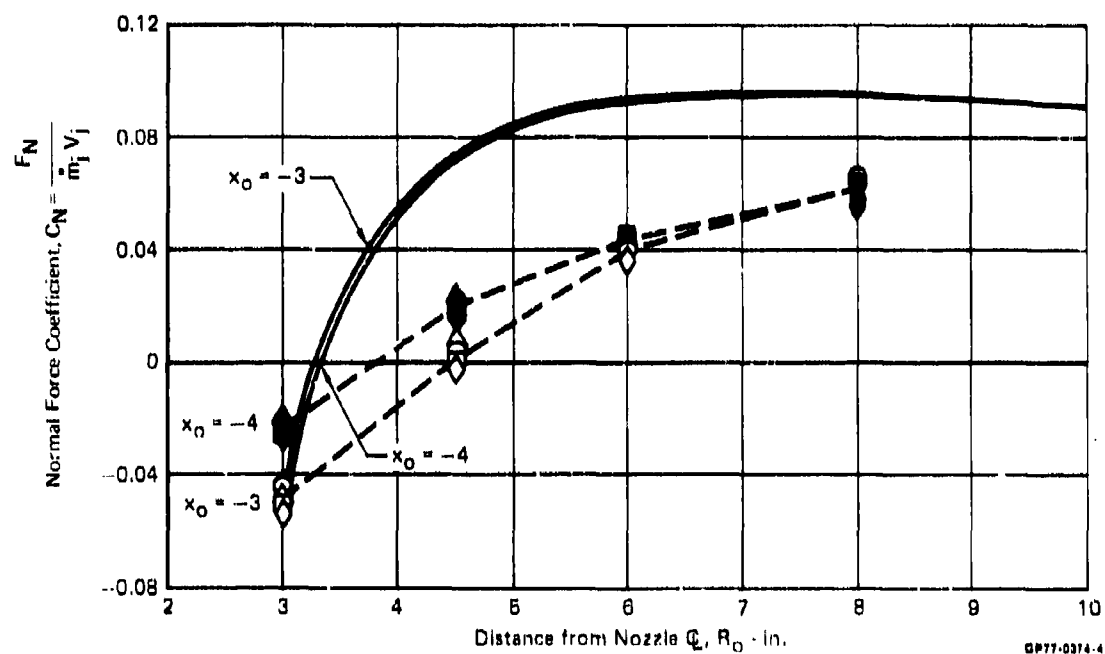
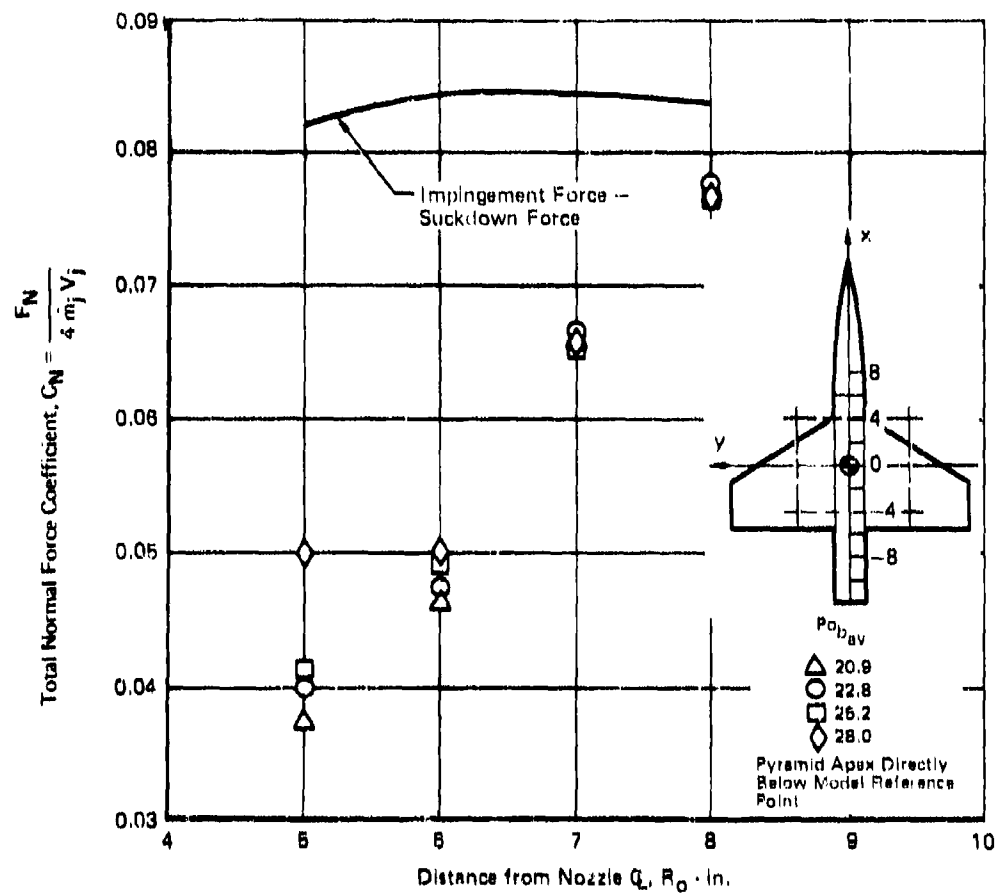


FIGURE 78
VARIATION IN THEORETICAL AND EXPERIMENTAL NORMAL FORCE
COEFFICIENT WITH HEIGHT ABOVE NOZZLE CENTERLINE



QF77-0374-88

FIGURE 79
COMPARISON BETWEEN THEORY AND EXPERIMENT - FOUR RADIAL JETS

7. EFFECTS OF PROTUBERANCES ON INDUCED FORCES

Protuberances on the underside of an airframe may be used to enhance the positive fountain force, provided they are judiciously placed. These protuberances may be underwing stores and pylons, landing gear doors, speed brakes, deflected flaps, or simply plates located expressly for increasing the overall lift on the airframe. Methods to estimate the effects of underwing stores and deflected flaps on the fountain force have been derived as part of this study. They are extensions of techniques to calculate the fountain impingement force which have been described in Section 6.

It was shown in Section 6 that the total fountain force is made up of a positive impingement force and a negative suckdown force. It is assumed that the presence of underwing protuberances does not affect the suckdown force, but does produce an increment in the impingement force. For underwing stores and for a trailing edge flap, the calculation of these increments is outlined in the following subsections. Comparisons to experimental results from the fountain impingement test described in Section 6.3 are also shown. The methods apply only to two-jet configurations but they could be combined to include multiple-jet configurations.

7.1 Fountain Force Increment Due to Stores

In Section 6.1.1, a specific type of flow turning process has been postulated to occur when a radial jet strikes the underside of the airframe. In this turning process, depicted in Figure 62, the velocity component normal to the aircraft platform is rotated by 90° , and the tangential component is unchanged. The flow produced on the underside of the airframe when the radial jet's plane of symmetry is perpendicular to the aircraft plane of symmetry then has a velocity component in the spanwise direction. This spanwise flow is inhibited by the presence of wing pylons, and an increase in fountain force results.

Figure 80 shows a drawing of the aircraft model used for the fountain impingement test program, with chordwise plates mounted on the wing undersurface to simulate underwing pylons and stores. When the model undersurface is clean, the fountain impingement force has been calculated by equating the normal component of the jet dynamic pressure to the pressure difference acting on the aircraft planform. This pressure was taken to act over the radial jet's "footprint" on the planform. Since the chordwise plates restrict the jet's spanwise flow, it is assumed that for the jet sector subtended by the distance between the plates, the total jet dynamic pressure is recovered as a positive pressure on the planform undersurface. In Figure 80, this occurs over the part of the fountain footprint indicated by the double crosshatching. Note that as R_0 increases, the angle

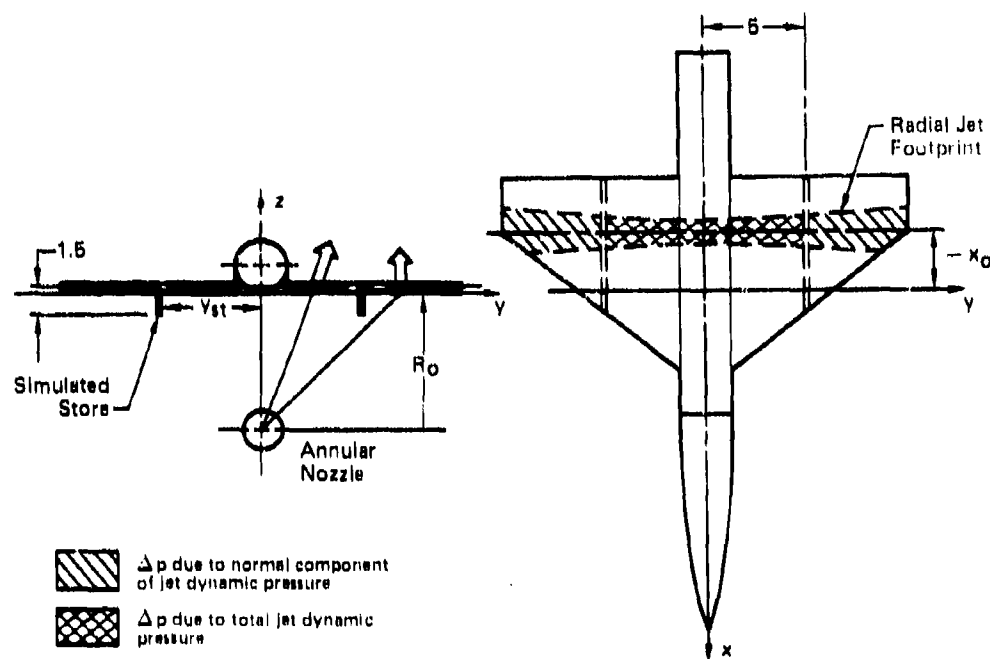


FIGURE 80
CALCULATION OF NORMAL FORCE INCREMENT DUE TO UNDERWING STORES

QP77-0374-8

subtended by the distance between the stores decreases, so that the normal force increment will decrease.

Under the above assumptions, the normal force increment acting on a planform strip dy will be:

$$d(\Delta F_z) = \int_{x_t}^{x_1} \frac{\rho}{2} V_R^2 (1 - \cos^2 \theta) dx dy$$

or,

$$d(\Delta F_z) = \frac{\rho}{2} \int_{x_t(y)}^{x_1(y)} V_R^2 \sin^2 \theta dx dy$$

The x -integration can be carried out as detailed in Section 6.1.1.2. Using:

$$\sin \theta = \frac{y}{\sqrt{y^2 + R_o^2}} = \frac{\bar{y}}{\sqrt{1 + \bar{y}^2}} \quad (127)$$

an expression equivalent to Equation (97a) can be derived for the total impingement force increment due to one of the chordwise plates. The result is:

$$\Delta \bar{F}_{z_{st}} = \frac{(0.374)}{2\pi} \int_0^{y_{st}} \frac{\bar{y}^2}{(1 + \bar{y}^2)^{3/2}} \left[\tanh \xi^* - \frac{1}{3} \tanh^3 \xi^* \right]_{\xi_T^*}^{\xi_L^*} d\bar{y} \quad (128a)$$

where,

$$\xi^* = (1.763) \left[\frac{x - x_0}{\Delta x_g} \right] \quad (128b)$$

$$\bar{y} = y/R_0 \quad (128c)$$

and the other variables are defined in Section 6.1.1.2. For the configuration tested during the fountain impingement test program, $x_0 = 3$ in., and the entire fountain footprint was captured in the chordwise direction. Then, taking the limit in Equation (128a) as

$$\xi_L^* \rightarrow +\infty$$

$$\xi_T^* \rightarrow -\infty$$

it becomes

$$\Delta F_{z_{st}} = \frac{1}{4\pi} \int_0^{y_{st}} \frac{\bar{y}^2}{(1 + \bar{y}^2)^{3/2}} d\bar{y} \quad (129)$$

letting

$$b_{st} = \text{span between stores}$$

$$y_{st} = \frac{b_{st}}{2R_0}$$

Defining the total normal force increment

$$\Delta C_{N_{st}} = 2\Delta F_{z_{st}}$$

and carrying out the integration in Equation (129)

$$\Delta C_{N_{st}} = \frac{1}{2\pi} \left\{ \ln \left[\left(\frac{b_{st}}{2R_0} \right) + \sqrt{1 + \left(\frac{b_{st}}{2R_0} \right)^2} \right] - \frac{\left(\frac{b_{st}}{2R_0} \right)}{\sqrt{1 + \left(\frac{b_{st}}{2R_0} \right)^2}} \right\} \quad (130)$$

For the case tested

$$b_{st} = 10 \text{ in.}$$

and Equation (130) is plotted in Figure 81 along with data from the fountain impingement test. In Figure 81, the calculated incremental normal force coefficient is added to the clean configuration data, to obtain the solid line. This is to be compared with the data points obtained with the simulated stores. For the case shown, the chordwise plates extended from the wing leading edge to 72% of the local wing chord. The agreement between data and experiment is quite satisfactory except for the lowest value of R_0 .

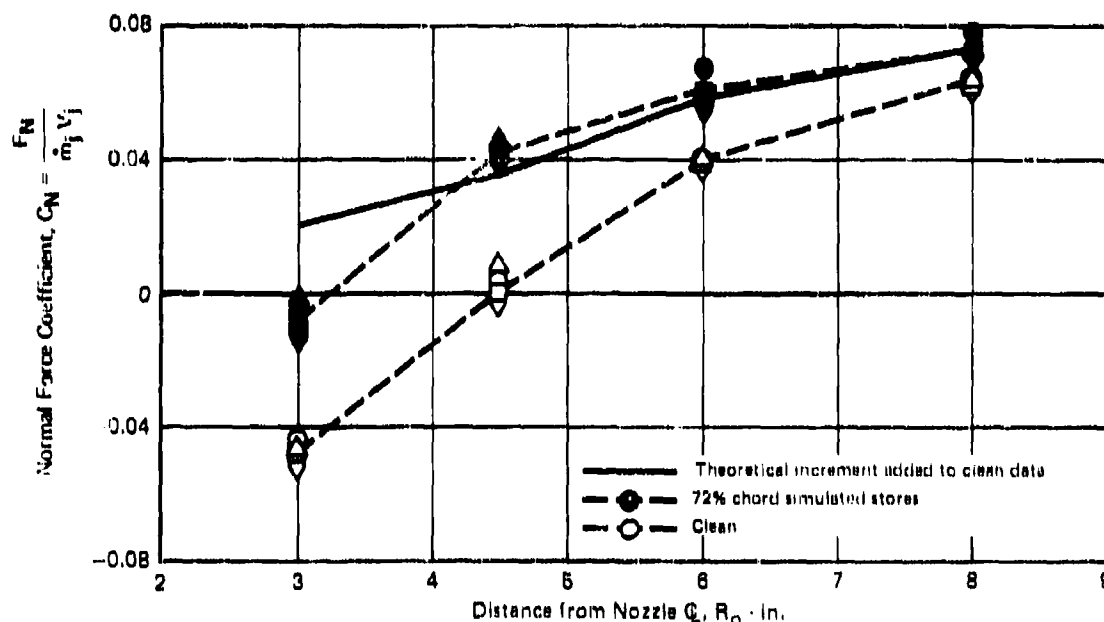


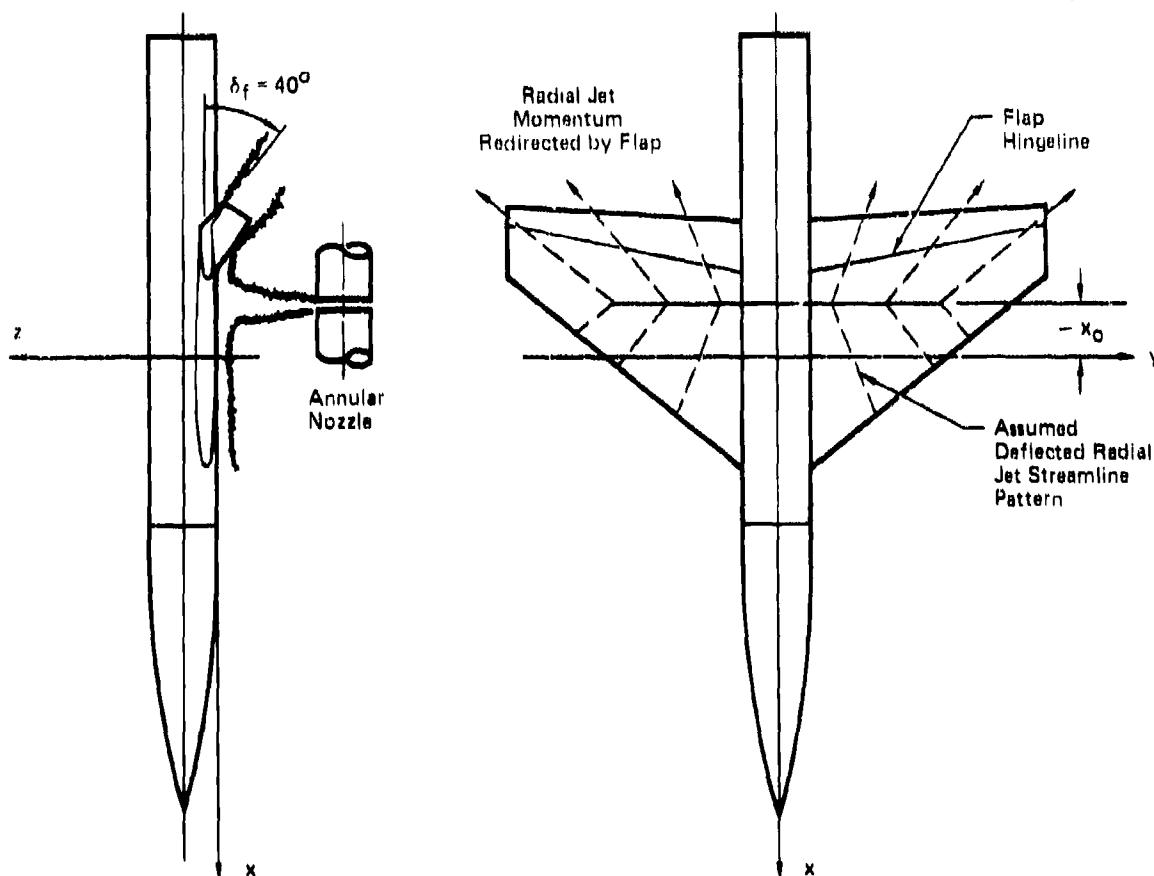
FIGURE 81

QP77-0374-8

THEORETICAL AND EXPERIMENTAL NORMAL FORCE COEFFICIENT WITH SIMULATED STORES

7.2 Fountain Force Impingement Due to Trailing Edge Flap Deflection

Figure 82 illustrates the reasoning used to predict the increment in fountain impingement force produced by deflecting a trailing edge flap. Once again, the geometry corresponds to that tested in the fountain impingement experimental program. The effect of the flap is to redirect the flow along the wing bottom surface downward, and in so doing, to create an upward reaction force on the airframe. For the case considered, the flap extends along the entire exposed wing span, the flap hinge line is at 72% of local chord, and the flap deflection angle is 40° . As before, the radial jet is assumed to split and "fold" upon impingement



GP77-0374-7

FIGURE 82
CALCULATION OF NORMAL FORCE INCREMENT DUE TO FLAP

on the wing undersurface. The normal force is then related to the momentum flux normal to the wing trailing edge.

A "momentum flux diagram", analogous to the "mass flow diagrams" used to calculate fountain suckdown forces in Section 6 is shown in Figure 83. Referring to Equation (72), the momentum flux normal to the wing trailing edge is given by

$$\dot{M} = \frac{\dot{M}_1 R}{4\pi} [\sin \theta_f - \sin \theta_0] \quad (135)$$

A factor of (1/2) has been introduced to account for the fact that only one half of the radial jet momentum is deflected towards the trailing edge. In addition, another factor of 1/2 should be included to account for the fact that, as

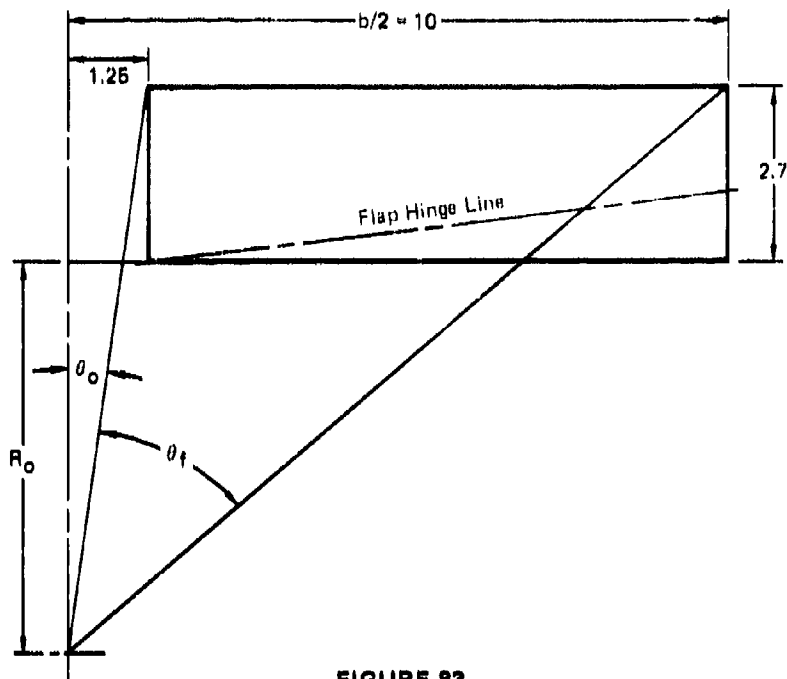


FIGURE 83
MOMENTUM FLUX DIAGRAM FOR COMPUTING FOUNTAIN FORCE
INCREMENT DUE TO TRAILING EDGE FLAP DEFLECTION

OP77-0274-81

discussed in Section 6.1.1.2, the dynamic pressure impact relation implies that one half of the radial jet's momentum is lost when it impinges on the wing under-surface. On the other hand, Equation (135) would have to be multiplied by 2 to account for the other half of the symmetric momentum flux diagram. Consequently, Equation (135) will be taken to represent the momentum flux needed to calculate the total fountain force increment. Introducing the momentum component normal to the planform, the normal force increment is given by

$$\Delta F_z = \frac{\dot{M}_j R}{4\pi} \sin \delta_f [\sin \theta_f - \sin \theta_0]$$

So, in terms of a normal force coefficient

$$\Delta C_{N_f} = \frac{\sin \delta_f}{4\pi} [\sin \theta_f - \sin \theta_0] \quad (136)$$

Note that in Figure 83 the flap only extends across the exposed wing span. The angles θ_f and θ_0 are:

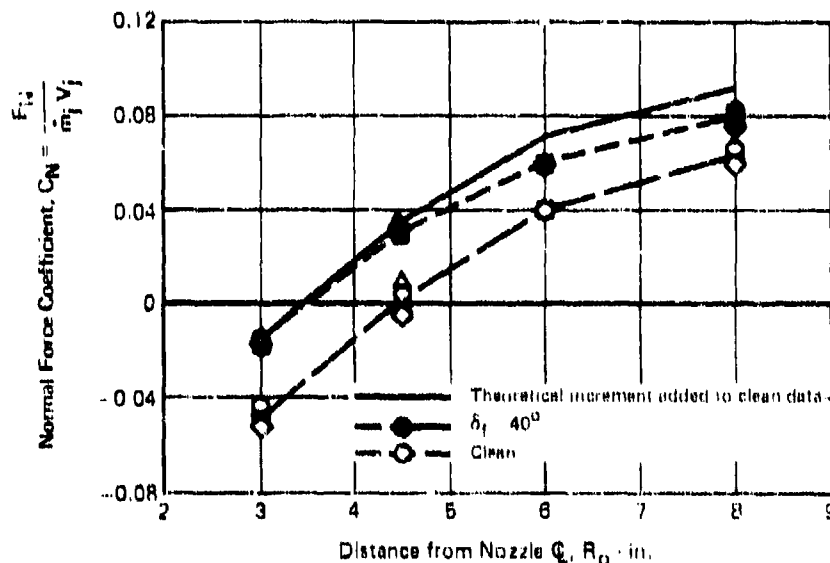
$$\sin \theta_f = \frac{b/2}{\sqrt{(b/2)^2 + (R_o + 2.7)^2}} \quad (137a)$$

and

$$\sin \theta_o = \frac{(1.25)}{\sqrt{(b/2)^2 + (R_o + 2.7)^2}} \quad (137b)$$

There is an extra force increment due to the momentum flux across the flap tip, but this term has been neglected.

Equations (135) and (137) were used to calculate an incremental normal force coefficient due to flap deflection. This increment was added to the clean configuration normal force coefficient, and the result is indicated by the solid line in Figure 84. The figure also includes the experimental results obtained with the deflected flap. Agreement between theory and data is satisfactory, although the theory appears to overpredict the force at the higher values of R_o .



GP77-0514-8

FIGURE 84
THEORETICAL AND EXPERIMENTAL NORMAL FORCE COEFFICIENTS
WITH FULL-SPAN FLAPS

8. SUMMARY OF RESULTS AND RECOMMENDATIONS FOR FURTHER STUDY

A methodology for the prediction of propulsive lift system jet induced aerodynamic effects for multi-jet VTOL aircraft hovering in and out of ground effect has been developed. To implement the analysis, the viscous (turbulent) flowfield below the aircraft in ground effect has been divided into five major elements:

1. Free-jet development.
2. Jet impingement.
3. Wall-jet development.
4. Stagnation and fountain base line formation.
5. Fountain development and impact on aircraft under-surface.

The forces (suckdown) and moments on the fuselage/wing induced by the entrainment of the turbulent free-jets and wall-jets both in and out of ground effect (where appropriate) are computed by a Douglas Neumann potential flow procedure which has been modified specifically for VTOL hover computations. The entrainment of the jets is modeled by prescribing, from empirical data, a sink distribution on the jet surfaces which simulates the inflow due to turbulent jet entrainment. This requires the panelling of pertinent free-jet and wall-jet surfaces. Forces and moments from the induced potential flows are determined on airframe surface panels from local surface pressures computed by application of the Bernoulli equation.

The contribution to the overall forces and moments on the airframe due to fountain impingement is computed separately and added to the induced potential flow computation results. Since the fountain impinges on the airframe directly, the prediction methods developed are more empirical in nature. To calculate the fountain forces, an analogy between fountains and radial jets with virtual origins located below the ground plane surface was established. The dynamic pressure distribution in these jets was used to calculate the fountain impingement force on the airframe, and the entrainment distribution on these jets was used to calculate a fountain suckdown force.

Limited comparisons of the results of the complete prediction methodology with experimental data in ground effect for a 15% scale model of a four lift jet VTOL attack aircraft were made. These comparisons showed acceptable agreement between measured and computed suckdown forces and overprediction of the magnitude of the fountain impingement force. The overprediction of the fountain impingement force is thought to be due to the inability of the methodology to predict fountain suppression due to partial merging of the lift jets prior to ground impingement or overlap of impingement regions on the ground plane.

8.1 Free Jet Development

The data obtained on non-circular jets show a considerable amount of scatter and are rather limited in scope. Specifically, more information on the entrainment rate distribution for rectangular jets with non-uniform exit velocity profiles is required, and information on the entrainment characteristics of compressible rectangular jets is needed.

8.2 Jet Impingement and Wall-Jets

The methodology developed herein assumes that wall-jet properties are established by the impingement of individual jets on the ground plane. Flow properties at the exit of the impingement region (as investigated in Reference 2 for circular jets) are needed for jets from non-circular nozzles, especially high aspect ratio ($AR \geq 4$) rectangular nozzles. Additionally, in cases where two or more jets merge or partially merge before impingement, or where two jets impinge with overlapping impingement region radii, R_I , the formation of a fountain between the two jets may be suppressed. The magnitude of this suppression and its dependence on jet spacing and nozzle exit shape must be investigated.

8.3 Fountain Development

The fountain upwash flowfield models developed in this study have been restricted to fountains generated by a combination of circular or nearly circular jets, all of which impinge at 90° to the ground plane, are located at the same height above the ground plane, and have equal thrust. There are no data on the fountains generated when the jet interaction flowfield is asymmetric even for the simplest case of two perpendicular jets of different thrust. The fountain flowfield development for non-circular nozzles is another area that requires further investigation. In the calculation of fountain induced forces and moments, there are areas which require further development, even within the restriction of the present fountain flowfield models. The fountain suckdown force is currently calculated by a rather crude method, and this shortcoming could be improved by including the fountain entrainment distribution in the overall suckdown calculation performed with the Douglas Neumann potential flow program.

9. REFERENCES

1. Ricou, F. P., and Spalding, D. B., "Measurements of Entrainment by Axisymmetric Turbulent Jets", *Journal of Fluid Mechanics*, Vol. 11, Part 1, p 21, 1961.
2. Donaldson, C. du P., and Snedeker, R. S., "A Study of Free Jet Impingement, Part I - Mean Properties of Free and Impinging Jets", *Journal of Fluid Mechanics*, Vol. 45, Part 2, pp 281-319, 1971.
3. Hill, B. J., "Measurement of Local Entrainment Rate in the Initial Region of Axisymmetric Turbulent Air Jets", *Journal of Fluid Mechanics*, Vol. 51, Part 4, pp 773-779, 1972.
4. Kleis, S. J., and Foss, J. F., "The Effect of Exit Conditions on the Development of an Axisymmetric Turbulent Free Jet", Third Year Technical Report, NASA Grant NGR 23-004-068, Michigan State University, 15 May 1974.
5. Trentacoste, N., and Sforza, P., "Further Experimental Results for Three-Dimensional Free Jets", *AIAA Journal*, Vol. 5, No. 5, p 885, May 1967.
6. Wygnanski, I., "The Flow Induced by Two-Dimensional and Axisymmetric Turbulent Jets Issuing Normally to an Infinite Plane Surface", Report No. 63-12, Mechanical Engineering Research Laboratories, McGill University, Montreal, Canada, December 1963.
7. Poreh, M., and Cermak, J. E., "Flow Characterization of a Circular Submerged Jet Impinging Normally on a Smooth Boundary", 6th Midwestern Conference on Fluid Mechanics, The University of Texas, 1959.
8. Witze, P. O., "A Study of Impinging Axisymmetric Turbulent Flows: the Wall Jet, the Radial Jet, and Opposing Free Jets", Sandia Laboratories, Combustion Research Division, Report SAND 74-8257, January 1975.
9. Donaldson, C. du P., and Gray, K. E., "Theoretical and Experimental Investigation of the Compressible Free Mixing of Two Dissimilar Gases", *AIAA Journal*, Volume 4, No. 11, November 1966.
10. Warren, W. R., "An Analytical and Experimental Study of Compressible Free Jets", Princeton University Dept. of Aeronautical Engineering, Report 381, 1957.
11. Siciari, M. J., Barche, J., and Migdal, D., "V/STOL Aircraft Prediction Technique Development for Jet-Induced Effects", Vol. 1, Grumman Aerospace Corp., PDR-623-18, Report prepared under NAPTC Contract N00140-74-C-0113, 15 April 1975.

9. REFERENCES (Continued)

12. Abramovich, G. N., "The Theory of Turbulent Jets", The M.I.T. Press, Cambridge, Mass., 1963.
13. Rozenblat, R. A., Schmitt, J. D., and Durando, N. A., "Lift Induced on a Wing by an Adjacent Lift/Cruise Fan", Prediction Methods for Jet V/STOL Propulsion Aerodynamics, Naval Air Systems Command, Research and Technology Group, July 1975.
14. Bower, W. W., and Kotansky, D. R., "A Navier - Stokes Analysis of the Two-Dimensional Ground Effects Problem", AIAA Paper No. 76-621, July 1976.
15. Tani, I., and Komatsu, Y., "Impingement of a Round Jet on a Flat Surface", Proceedings of the Eleventh International Congress of Applied Mechanics (Munich, Germany), 1964, pp 672-676.
16. Hess, J. L., and Mack, D. P., "Calculation of Potential Flow About Arbitrary Three-Dimensional Lifting Bodies", McDonnell Douglas Corporation Report J5679, Volumes 1 and 2, October 1972.
17. Saunders, P. W. and Bristow, D. R., "Douglas Neumann Computations for Potential Flow About Arbitrary Three-Dimensional Bodies with Modifications for V/STOL Applications", McDonnell Douglas Corporation Report MDC A4707, 1 March 1977.
18. Hess, J. L., "The Use of Higher Order Surface Singularity Distributions to Obtain Improved Potential Flow Solutions for Two-Dimensional Lifting Airfoils", Computer Methods in Applied Mechanics and Engineering, Volume 5, No. 1, January 1975.
19. Kellogg, O. D., Foundations of Potential Theory, p 219, Dover Publications, Inc., New York, 1953.
20. Bristow, D. R., "Incompressible Potential Flow: Numerical Characteristics of Three Classical Surface Singularity Representations", McDonnell Douglas Corporation Report A4407, September 1976.
21. Catherall, D., Foster, D. N., and Sells, G.C.L., "Two Dimensional Incompressible Flow Past a Lifting Aerofoil", R.A.E. TR-69118, 1969.
22. Wagnanski, I., "The Flow Induced by Two-Dimensional and Axisymmetric Turbulent Jets Issuing Normally to an Infinite Plane Surface", McGill University Mechanical Engineering Research Laboratories Report 63-12, December 1963.
23. Anon., "V/STOL Aerodynamic-Propulsive Interactions", 1976 Independent Research and Development Report MDC Q0844-7, Volume 2, January 1976, pp 7064.01-7064.18.

9. REFERENCES (Continued)

24. Hall, G. R., and Rogers, K. H., "Recirculation Effects Produced by a Pair of Heated Jets Impinging on a Ground Plane", NASA CR 1307, May 1969.

NOT
PRECEDING PAGE BLANK - FILMED

APPENDIX I AIRFRAME AND JET COORDINATES

Problem: To define airframe geometry, jet positions, jet vectoring angles, and jet impingement points for an arbitrary VTOL configuration hovering in ground effect.

Approach: Derive transformation from airplane fixed to ground fixed coordinates. Locate jet exit positions in ground fixed coordinates and jet inclination angles relative to ground plane. For each nozzle, locate effective jet impingement point on ground. This point is defined as the intersection with the ground plane of a straight line inclined at the jet inclination angle and going through the nozzle center of thrust.

Purpose: To provide basic geometric input to (static) aero-propulsive interaction problem. Input geometric parameters are assumed to be:

- o Airplane e.g. location (fuselage station, waterline, butt line).
- o Location of center of thrust for each nozzle.
- o Thrust vectoring and splay angles for each nozzle.
- o Airframe angle of pitch, roll and yaw. (The latter is only important for cross wind cases.)
- o Height of airplane e.g. above ground plane.

Transformation Equations

Transform unit base vectors

$$(\hat{i}, \hat{j}, \hat{k})$$

along airplane-fixed axes (x, y, z) in Figure 1-1, to vectors

$$(\hat{i}^n, \hat{j}^n, \hat{k}^n)$$

along lines (A, B, C) respectively.

The reference angles are the standard Euler angles:

θ : pitch

ψ : yaw

ϕ : roll

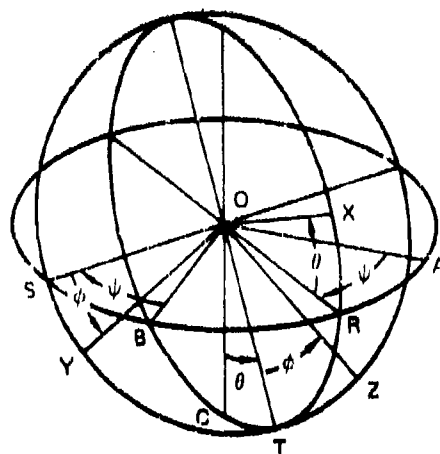


FIGURE I-1
EULER ANGLES

GP77-0374-48

Defining first the intermediate vectors \bar{e}_r and \bar{e}_s along lines OR and OS, respectively:

$$\bar{e}_r = \bar{i}'' \cos \psi + \bar{j}'' \sin \psi$$

$$\bar{e}_s = -\bar{i}'' \sin \psi + \bar{j}'' \cos \psi$$

Using these vectors, the relation between the unprimed and double-primed base vectors may be shown to be:

$$\bar{i} = \bar{i}'' [\cos \psi \cos \theta] + \bar{j}'' [\sin \psi \cos \theta] - \bar{k}'' [\sin \theta] \quad (I-1a)$$

$$\bar{j} = \bar{i}'' [\cos \psi \sin \theta \sin \phi - \sin \psi \cos \phi] \quad (I-1b)$$

$$+ \bar{j}'' [\sin \psi \sin \theta \sin \phi + \cos \psi \cos \phi] + \bar{k}'' [\sin \phi \cos \theta]$$

$$\bar{k} = \bar{i}'' [\cos \psi \sin \theta \cos \phi + \sin \psi \sin \phi] + \quad (I-1c)$$

$$+ \bar{j}'' [\sin \psi \sin \theta \cos \phi - \cos \psi \sin \phi] + \bar{k}'' [\cos \theta \cos \phi]$$

Now introduce a third, ground fixed, coordinate system such that

$$\bar{i}' = \bar{i}''$$

$$\bar{j}' = \bar{j}''$$

$$\bar{k}' = -\bar{k}''$$

(I-2)

$$x' = x''$$

$$y' = y''$$

$$z' = (z'' - h_{cg})$$

(I-3)

where h_{cg} is the height of the center of gravity above the ground plane, positive upward.

In the airplane coordinates, the n th jet nozzle location will be defined by a vector

$$\vec{r}_{jn} = \vec{i} x_{jn} + \vec{j} y_{jn} + \vec{k} z_{jn}$$

Equations (1-1), (1-2) and (1-3) may be used to obtain the nozzle coordinates in the ground fixed system

$$\vec{r}'_{jn} = \vec{i}' x'_{jn} + \vec{j}' y'_{jn} + \vec{k}' z'_{jn}$$

where

$$\begin{aligned} x'_{jn} = & x_{jn}[\cos \psi \cos \theta] + y_{jn}[\cos \psi \sin \theta \sin \phi - \sin \psi \cos \phi] \quad (1-4a) \\ & + z_{jn}[\cos \psi \sin \theta \cos \phi + \sin \psi \sin \phi] \end{aligned}$$

$$\begin{aligned} y'_{jn} = & -x_{jn}[\sin \psi \cos \theta] - y_{jn}[\sin \psi \sin \theta \sin \phi + \cos \psi \cos \phi] \quad (1-4b) \\ & - z_{jn}[\sin \psi \sin \theta \cos \phi - \cos \psi \sin \phi] \end{aligned}$$

$$z'_{jn} = h_{cg} + x_{jn}[\sin \theta] - y_{jn}[\sin \phi \cos \theta] - z_{jn}[\cos \theta \cos \phi] \quad (1-4c)$$

The thrust vector direction for the n th nozzle is defined by two angles,

Thrust deflection angle δ_n

Nozzle play angle ϵ_n

Referring to Figure 1-2, a unit thrust vector in the airplane coordinate system is then given by

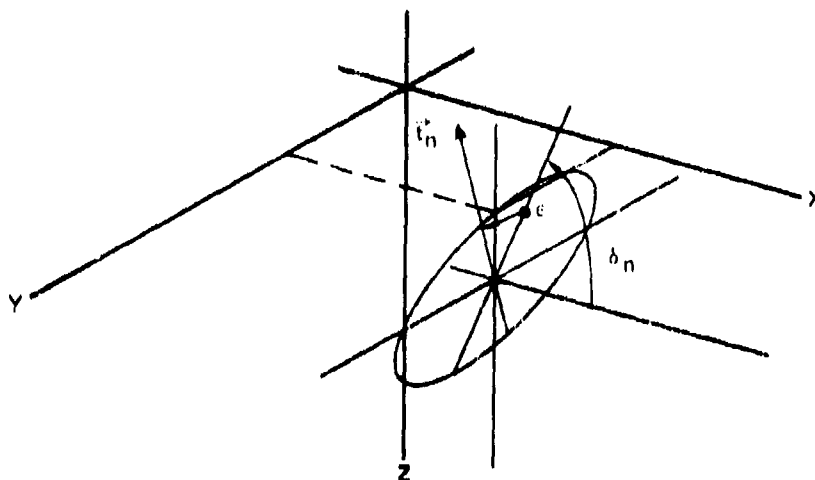
$$\vec{t}_n = \vec{i} (\cos \epsilon_n \cos \delta_n) + \vec{j} (\sin \epsilon_n) + \vec{k} (\cos \epsilon_n \sin \delta_n) \quad (1-5)$$

In the ground coordinate system, the unit thrust vector for the n th nozzle is denoted by

$$\vec{t}'_n = \vec{i}' t'_{x'_n} + \vec{j}' t'_{y'_n} + \vec{k}' t'_{z'_n}$$

and using Equations (1-1), (1-2) and (1-3), Equation (1-5) yields

$$\begin{aligned} t'_{x'_n} = & (\cos \epsilon_n \cos \delta_n)[\cos \psi \cos \theta] - \sin \epsilon_n [\cos \psi \sin \theta \sin \phi - \sin \psi \cos \phi] \\ & + (\cos \epsilon_n \sin \delta_n)[\cos \psi \sin \theta \cos \phi + \sin \psi \sin \phi] \quad (1-6a) \end{aligned}$$



GP77-0374-47

FIGURE I-2
NOZZLE THRUST DEFLECTION ANGLE AND SPLAY ANGLE

$$t'_{y_n} = -(\cos \epsilon_n \cos \delta_n)[\sin \psi \cos \theta] - \sin \epsilon_n [\sin \psi \sin \theta \sin \phi + \cos \psi \cos \phi] \\ + (\cos \epsilon_n \sin \delta_n)[\sin \psi \sin \theta \cos \phi - \cos \psi \sin \phi] \quad (1-6b)$$

$$t'_{z_n} = (\cos \epsilon_n \cos \delta_n)[\sin \theta] - \sin \epsilon_n [\sin \phi \cos \theta] \\ + (\cos \epsilon_n \sin \delta_n)[\cos \theta \cos \phi] \quad (1-6c)$$

The effective jet impingement point is defined by the intersection of a straight line emanating from the nozzle center and parallel to the t'_n vector, and the ground plane $z' = 0$. From the equation for the line

$$\frac{x' - x'_{jn}}{t'_{x_n}} = \frac{y' - y'_{jn}}{t'_{y_n}} = \frac{z' - z'_{jn}}{t'_{z_n}}$$

it can be shown that the effective impingement point coordinates are given by:

$$y'_{on} = y'_{jn} - \left(\frac{t'_{y_n}}{t'_{z_n}} \right) z'_{jn} \quad (1-7a)$$

$$x'_{on} = x'_{jn} - \left(\frac{t'_{x_n}}{t'_{z_n}} \right) z'_{jn} \quad (1-7b)$$

The effective impingement angle for the nth jet is defined as

$$\sigma_n = \cos^{-1} (\vec{k}' \cdot \vec{t}'_n)$$

or

$$\sigma_n = \cos^{-1} (t'_{z,n}) \quad (I-8)$$

APPENDIX II

JET PATH DEFLECTION DUE TO CROSS-FLOW

The position and direction of the thrust vector for the nth nozzle of an aircraft at an arbitrary attitude may be specified by the transformation equations in Appendix I. The reference coordinate system is fixed to the ground and defined by the (x', y', z') axes shown in Figure II-1. The position of the thrust vector for the nth jet is denoted by :

$$\vec{r}_{jn} = \hat{i}' x'_{jn} + \hat{j}' y'_{jn} + \hat{k}' z'_{jn} \quad (II-1)$$

and its direction by the unit vector :

$$\vec{t}'_n = \hat{i}' t'_{x'_n} + \hat{j}' t'_{y'_n} + \hat{k}' t'_{z'_n} \quad (II-2)$$

In the above equations $(\hat{i}', \hat{j}', \hat{k}')$ are unit vectors in the (x', y', z') directions, respectively. In a crossflow, the jet path for the nth jet is defined by the empirical equation presented in Reference 12 :

$$\xi = \left[\frac{|\vec{V}_\infty|}{|\vec{V}_j|} \right]^{2.6} \zeta^3 + \zeta \tan \theta_{on} \quad (II-3)$$

where ξ and ζ are distances which have been normalized by the jet diameter, and θ_{on} is the complement of the angle between the jet velocity vector and the free stream velocity vector. This equation has been used with good results in studies of power-induced effects in transition flight, (Reference 13).

Equation (II-3) is considered to apply in the plane defined by the free stream and jet velocity vectors. By definition of the ground-fixed coordinate system,

$$\vec{V}_\infty = - \hat{i}' |\vec{V}_\infty| \quad (II-4)$$

and since the jet velocity vector direction is opposite to that of the thrust vector

$$\vec{V}_{jn} = - \hat{t}'_n |\vec{V}_{jn}| \quad (II-5)$$

The cross product of these two vectors defines the normal to the plane which contains them, and the dot product defines the angle between the free stream and jet velocities. Thus

$$-(\vec{V}_{jn} \times \vec{V}_\infty) = \vec{e}_{2n} |\vec{V}_{jn}| |\vec{V}_\infty| \cos \theta_{on} \quad (11-6A)$$

$$\vec{V}_{jn} \cdot \vec{V}_\infty = |\vec{V}_{jn}| |\vec{V}_\infty| \sin \theta_{on} \quad (11-6B)$$

where the unit vector \vec{e}_{2n} and the angle θ_{on} are shown in Figure 11-1.

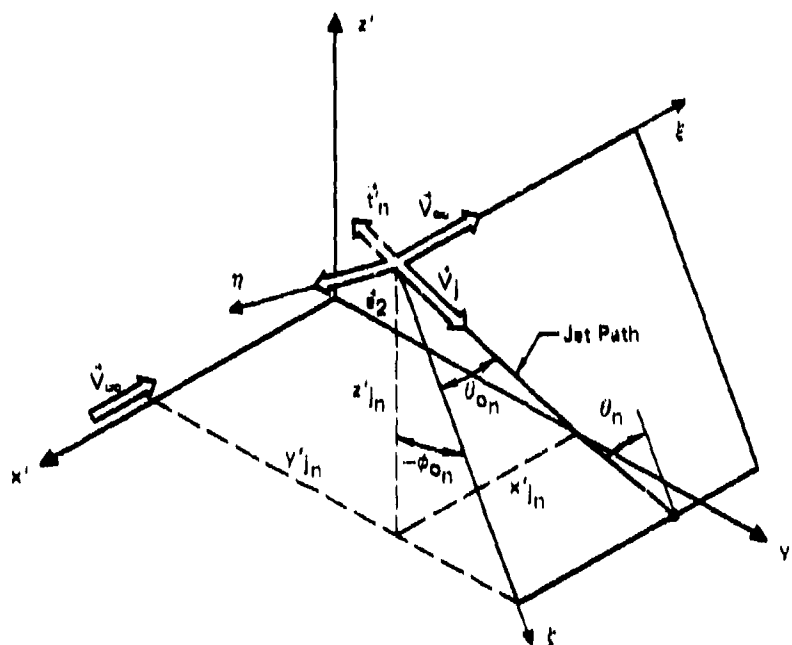


FIGURE 11-1
JET PATH PLANE DEFINITION

OP77 0374 40

Using Equations (II-4) and (II-5) in Equations (II-6), it is possible to show that

$$\theta_{on} = \sin^{-1} [t'_{x'_n}] \quad (11-7A)$$

and

$$\vec{e}_{2n} = [1 - t'^2_{x'_n}]^{-1/2} \begin{bmatrix} -j' t'_{z'_n} + k' t'_{y'_n} \\ \end{bmatrix} \quad (11-7b)$$

From Equation (II-7b) it is then possible to calculate the angle

$$\phi_{0n} = \cos^{-1} [t'_{z'n} / (1 - t'^2_{x'n})^{1/2}] \quad (\text{II-8})$$

This angle is also shown in Figure II-1.

In the (x', y', z') coordinate system, points along the jet path are given by

$$x'_{pn} = -d_{jn}\xi + x'_{jn} \quad (\text{II-9a})$$

$$y'_{pn} = y'_{jn} - d_{jn}\zeta \sin \phi_{0n} \quad (\text{II-9b})$$

$$z'_{pn} = z'_{jn} - d_{jn}\zeta \cos \phi_{0n} \quad (\text{II-9c})$$

where ξ and ζ are related by Equation (II-3) and d_{jn} is the exit diameter for the n th jet. Intersection with the ground plane is defined by the condition

$$z'_{pn} = 0$$

Using this in (II-9c) and substituting in (II-9b)

$$y'_{on} = y'_{jn} - z'_{jn} \tan \phi_{0n} \quad (\text{II-10})$$

and using (II-3) and (II-9a)

$$x'_{on} = x'_{jn} - d_{jn} \left\{ \left[\frac{|\vec{V}_\infty|}{|\vec{V}_{jn}|} \right]^{2.6} \left[\frac{z'_{jn}}{d_{jn} \cos \phi_{0n}} \right]^3 + \tan \theta_{0n} \left[\frac{z'_{jn}}{d_{jn} \cos \phi_{0n}} \right] \right\} \quad (\text{II-11})$$

Equations (II-10) and (II-11) define the point at which the jet path intercepts the ground. To define the angle of intersection, Equation (II-3) is differentiated to calculate

$$\tan \theta_n = 3 \left[\frac{|\vec{V}_\infty|}{|\vec{V}_{jn}|} \right]^{2.6} \left[\frac{z'_{jn}}{d_{jn} \cos \phi_{0n}} \right]^2 + \tan \theta_{0n} \quad (\text{II-12})$$

where Equation (II-9c) for $z'_{pn} = 0$ has been used, and where θ_n is the angle between the jet path and a perpendicular in the (ξ, ζ) plane, as shown in Figure II-1. With θ_n calculated from Equation (II-12), it is then possible to define a unit vector tangent to the jet path, and the components of this vector in the (x', y', z') system. The result is

$$t'_{on} = \hat{i}' (\sin \theta_n) + \hat{j}' (\cos \theta_n \sin \phi_{0n}) + \hat{k}' (\cos \theta_n \cos \phi_{0n}) \quad (\text{II-13})$$

As in Appendix I the effective impingement angle for the jet is

$$\sigma_n = \cos^{-1} [\vec{k}' \cdot \vec{e}'_{on}]$$

or

$$\sigma_n = \cos^{-1} [\cos \sigma_n \cos \phi_{on}] \quad (11-14)$$

In addition, the angle of the plane in which the above angle lies is given by

$$\gamma_n = \tan^{-1} [t'_{oy'_n} / t'_{ox'_n}]$$

or

$$\alpha_n = \tan^{-1} \left[\frac{\sin \phi_{on}}{\tan \phi_n} \right] \quad (11-15)$$